Estimation of Atmospheric Turbidity from a Sky Image and Its Applications

天空画像からの大気混濁係数推定とその応用

BY

Hongxun Zhao

A Doctoral Dissertation

Submitted to the Graduate School of
the University of Tokyo

in Partial Fulfillment of the Requirements
for the Degree of
Doctor of Information Science and Technology

July 2012

Thesis Supervisor: Katsushi IKEUCHI　池内　克史

Committee:

Kiyoharu AIZAWA (Chair)
Kaoru SEZAKI
Shunsuke KAMIJO
Yoichi SATO
Takeshi NAEMURA

ABSTRACT

Atmospheric turbidity is defined as the ratio of optical thickness of the haze atmosphere as opposed to molecules, it is widely used in the computer graphics and vision community for modeling the outdoor illumination.

This thesis proposes a novel method for estimating the atmospheric turbidity and provides three applications. Specifically, the atmospheric turbidity is estimated by matching the brightness distribution between a sky model and an actual image. By using the estimated turbidity, we recover the spectral sensitivity and white-balance parameters of digital cameras from sky images, render the virtual object with turbidity-based aerial perspective calculation, estimate the reflectance of outdoor diffuse object from a single perspective image.

Camera spectral sensitivity plays an important role for many physics-based computer vision methods, such as demosaicing, color correction and illumination estimation. However, less attention has been paid to estimating the spectral sensitivity. This is unfortunate, because this parameter significantly affect the image colors. We have proposed a novel method for estimating the spectral sensitivity from images. A basic idea is to use a sky image from which the spectra of the sky can be inferred. Given the input image, the atmospheric turbidity is estimated by fitting the brightness distribution to a sky model. Assuming the sun direction with respect to the camera view direction can be estimated, the sky spectra is calculated from the estimated turbidity. Having obtained the pairs of image *RGB* values and corresponding spectra, the spectral sensitivity is calculated by using basis-functions. The basis functions are extracted from the database which consists of collected spectral sensitivities of different digital cameras. The utilization of the basis functions makes the estimation accurate and robust.

Virtual object rendering has been widely used in the academy, the architecture, the entertainment and the heritage preservation. Aerial perspective plays an important rule for making the rendered image appear realistic, especially when the object is distant from the camera. The aerial perspective is caused by the scattering of particles in the atmosphere, it models the slight color change of distant object. The virtual object rendering with the aerial perspective effect is described. The spectral radiance of the sun and skylight is first calculated from the estimated turbidity, and the aerial perspective effect is calculated as the summation of in-scattered and out-scattered light along the camera view direction. Experimental results shows the accuracy of this technique.

Three-dimension models have been widely used in many fields. The reflectance is necessary for making a realistic 3D model. However, how to estimate the accurate re-

flectance still remains a challenge, especially for outdoor objects, because it is difficult to precisely model the outdoor illumination. Many trials have been made to capture the outdoor illumination, but these methods need expensive equipments and massive calibrations. We propose a novel method for estimating the reflectance of outdoor diffuse object from a single perspective image. The atmospheric turbidity is first estimated from the input image, and then the whole illumination condition is recovered from the estimated turbidity. The reflectance is calculated from the surface radiance and irradiance value. The proposed method also solves the problem of inter-reflection, which exists between concave surfaces. We assume the object surface consists of hundreds of small facets, and the inter-reflection is calculated as the incoming light energy from all other facets. Experimental results show the accuracy achieved by the proposed method.

The main contributions of this thesis are that a novel atmospheric turbidity estimation method and its three applications. It can be summarized by the four following points: First, the atmospheric turbidity is estimated by matching the brightness distributions between a sky model and an actual image. Second, the estimated atmospheric turbidity is used for recovering the camera spectral sensitivity and white balance parameters. Third, the estimated atmospheric turbidity is used to calculate the aerial perspective effect which makes the rendered image appear realistic. Fourth, the estimated atmospheric turbidity is used to model the outdoor illumination environment for estimating the reflectance of outdoor diffuse object.

Acknowledgements

First and foremost, I would like to acknowledge and extend my heartfelt gratitude to my thesis supervisor, Prof. Katsushi Ikeuchi, for his consideration and supervision. He encouraged and challenged me during every meeting, and gave me a lot of great ideas to solve the problem. His profound learning and down-to-earth attitude left a deep impression on me. I also would like to thank him for a great research environment provided in his laboratory.

My appreciation goes to Dr. Rei Kawakami of my direct senior associate. She is always patient with me and gave me significant advice to my research. I learned from her how to be a good researcher. I still remember she revising my paper line by line. She also made great efforts to make me adapt life in japan. I really appreciate the efforts she made for both my research and life.

Many thanks go to the people that I have been working with, the current and former members of the Computer Vision Laboratory at the University of Tokyo. Special thanks go to Dr. Robby T.Tan, who found time to direct me to overcome the difficulty and continue my research in the midst of all his activities, to Dr. Jun Takamatsu, who kindly helped me when i asked for the source code of one of his work and explained details to me, to Dr. Bo Zheng, who always helped me to solve the problem and concerned about my life. I would like to thank Tetsuya Kakuta, Tetsuro Morimoto, and Tomoaki Higo, for having interesting and fruitful discussions with me regarding the field of physics-based vision, to Bjoern Rennhak, Mawo Kamakura, Ulinta Ginting, Phongtharin Vinayavekhin, Jinge Wang, Sonoko Okura, and Boun Vinh Lu, for making my lab-time enjoyable. I am also indebted to Kiminori Hasegawa, Keiko Motoki, Yoshiko Matsuura, Kaoru Kikuchi, and Mikiko Yamaba, for help me going through the admission procedures and other procedures needed in my department.

Last but not least, I would like to pay my highest tribute to my family, my dear

mother and father. It was them that supported me during these years to make it possible to concentrate on my study and research. It was them that consoled me when i was upset and encouraged me to go ahead. I could not accomplish anything without their understanding and support. I dedicate this dissertation to my family.

July 2012
Hongxun Zhao

Contents

List of Figures

List of Tables

Chapter 1

Introduction

1.1 Background

The sky appearance is determined by scattering and absorption of solar irradiance due to various particles suspended in the atmosphere. The particle density changes according to many aspects, such as the weather condition, the cosmic bombardment and the oceans. The atmospheric turbidity is a heuristic parameter used for describing the characteristic of sky. Atmospheric turbidity is the ratio of the optical thickness of the haze atmosphere as opposed to the optical thickness of the atmosphere with molecules, it is widely used for modeling the characteristics of the sun and sky in the computer graphics and vision community. After acquiring the turbidity, we could calculate the spectral sensitivity of digital cameras, render the virtual object with the aerial perspective effect and estimate the surface reflectance of outdoor diffuse object.

Spectral Sensitivity Estimation Spectral sensitivity plays an important role for many computer vision applications, such as demosaicing (Brainard, 1994), color correction (Vrhel and Trussell, 1994) and illumination estimation algorithms (Freeman and Brainard, 1995; Maloney and Wandell, 1996). CCD (Charge Coupled Device) sensors usually provide only single response at each pixel, demosaicing is used to recover response of R, G and B channels based on the spectral sensitivity for each pixel. Color correction is a method that correct the obtained image to compensate for the effects of the recording illumination. Illumination estimation is used for recovering the illumination by acquiring different images under different illumination environments. Spectral

sensitivity is also an essential characteristic for color constancy methods. Captured appearance of object is different according to different illumination conditions. Color constancy method is used to remove the influence of light source and retrieve object surface color under standard illumination.

In computer vision and graphics research fields, a few methods that estimate the spectral sensitivity have been proposed. Vora et al (1997) measured the spectral sensitivity of two digital cameras: Kodak DCS-200 and Kodak DCS-420. In this paper, the target is illuminated by the monochromator which could produce narrow-band illumination. While changing the wavelength, the images and spectra are simultaneously captured by camera and spectrometer, respectively. The spectral sensitivity is calculated by dividing the image intensity by the measured spectra. Hardeberg et al. proposed a method that estimates spectral sensitivity by inverting the system of linear equations obtained by image intensities and known spectral reflectance (Hardeberg et al, 1998), while it has not been applied to real data because of the instability.

All these proposed methods of spectral sensitivity estimation require the image intensity as input. The image intensity is not linearly related to scene radiance because of the gamma function. In order to obtain the precise measurement of scene radiance to estimate the spectral sensitivity, the gamma function (also called as camera response function) must be estimated first. While less attention has been paid for estimating the spectral sensitivity, much attention has been paid for camera response estimation. Mann and Picard (1995) proposed a method that assumes the response functions can be approximated by gamma correction functions. Debevec and Malik (1997) estimate response functions with a non-parametric representation using a smoothness constraint. Takamatsu et al (2008) proposed a method for estimating camera response functions by maximizing the image similarity measurement defined as the integral of the probabilistic intensity similarity.

Virtual Object Rendering Virtual object rendering can insert virtual object created by computer graphics models into a real scene, hence it is widely used in many fields: the academy, the architecture, the entertainment and the heritage preservation. The shape information, the reflection properties and the illumination are required for rendering process. The aerial perspective effect is very important for making the rendered image appear realistic, especially when the object is far away from the camera.

For the seamless integration of virtual object with a real scene, it is crucial to achieve the illumination consistency. Two kinds of methods were proposed for estimating the

illumination condition. The first kind directly measures the illumination environment: Debevec (1998) uses the calibrated spheres for capturing the illumination, Sato et al (1999a) uses the camera attached with fish-eye lens for acquiring the illumination distribution. The other kind recovers the illumination environment from the shadows (Sato et al, 1999b; Kakuta et al, 2004).

Despite of illumination environment, much effort has been made for calculating the aerial perspective effect. Kaneda et al (1991) and Klassen (1987) discuss the aerial perspective effect and explicitly model it as a particular case of light scattering. These methods could be applied to various atmospheric conditions, however they are computer-intensive. Ward (1994) calculates the aerial perspective effect in the Radiance rendering system by assuming the ambient illumination is constant. It is an efficient approximation of aerial perspective, but it fails for different view directions or sun positions. Ebert et al (1998) model the aerial perspective by the Rayleigh scattering which caused by the particles with diameter smaller than the wavelength. The object color is calculated as the summation of surface color and weighted sky color when it is distant from the camera. The weight becomes larger when it moves further away.

Surface Reflectance Estimation Computer vision and graphics techniques to create a realistic model of a real world object have attracted interest from a wide range of research fields and industries in recent years. To simulate the accurate appearance of an object, shape and optical information are necessary. Acquiring shape information has been facilitated by the development of sensors and the progress of data processing algorithms, while estimating surface reflectance properties remains a challenge, especially for outdoor objects.

Several modeling methods with range sensors were proposed (Neugebauer and Klein, 1999; Bernardini et al, 2001); however those methods created surface textures by simply blending images taken from multiple views. Meanwhile, physics-based reflectance estimation methods (Dana et al, 1999; Machida et al, 2003), photometric stereo techniques (Basri and Jacobs, 2001; Hertzmann and Seitz, 2005; Chen et al, 2006), and image-based rendering techniques (Winnemoller et al, 2005) have been proposed to create more physically correct object appearances. Physics-based reflectance estimation is based on physical reflection models (Cook and Torrance, 1981) and estimates the parameters of the models by fitting the data to them. The methods have achieved highly accurate re-renderings, yet they need accurately calibrated illuminations and cameras. Photometric stereo is a method that captures images under three different

lighting conditions and estimates the surface reflectance and the surface normal of the shape. It assumes a known distant point light source, and therefore it is unsuitable for outdoor conditions. Image-based rendering is a technique that samples appearances under a number of different lighting conditions, and re-renders the appearance by interpolating the images. Creating such a number of different illumination conditions is impractical for an outdoor environment, and so it is difficult to be applied to outdoor objects.

Debvec et al (2000) proposed a method to obtain the reflectance function with the position of light sources known. To extend this idea to outdoor scenes, Yu and Malik (1998) measured the illumination of the scene by acquiring photographs of the sky and the surrounding environments. Most recently, Debevec et al (2004) introduced a novel lighting measurement apparatus than can record the high dynamic range of both, sunlit and cloudy environments, using a set of specular and diffuse calibrated spheres. With the captured illumination, proposed method estimates spatially varying surface reflectance. Weiss (2001) proposed a method to decompose an image into a reflectance image and an illumination image by assuming the change caused by reflectance remains constant in the image sequence, while the change caused by illumination varies depending on time. Therefore, by taking the median of derivative filter outputs of input images, the reflectance image can be estimated. Matsushita et al (2004) extended the idea so that it can handle non-Lambertian surfaces, and proposed an illumination normalization scheme utilizing the illumination eigen space and a shadow interpolation method based on shadow hulls.

1.1.1 Spectral Sensitivity Estimation

Spectral sensitivity of digital cameras can be calculated from the atmospheric turbidity. Spectral sensitivity is non-trivial information for many computer vision applications. Different cameras usually produce differently-colored images for the same scene due to the different characteristics of the spectral sensitivities.

Spectral sensitivity is the response of a sensor to monochromatic light as a functions of wavelength, also known as spectral response. This paper defines the spectral sensitivity on each *RGB* channel with the wavelength varying from 400 nanometers to 700 nanometers. The spectral sensitivity is normalized among three channels, therefore the maximum value is 1.0. Figure 1.1 shows the images captured by three different consumer cameras. As shown in the Figure, also indicated numerically by the chro-

(a) Canon IXY 900 IS.

(b) Casio EX-Z 1050.

(c) Panasonic DMC-FX 100.

Figure 1.1: The color difference of images taken by different cameras. The left, middle and right images are taken by Canon IXY 900 IS, Casio EX-Z 1050 and Panasonic DMC-FX 100, respectively. The images were adjusted to have the same scale of intensity values, to emphasize the color differences. The averaged chromaticity values (r, g, b) of the red squares are $(0.45, 0.32, 0.23)$ for Canon, $(0.39, 0.32, 0.29)$ for Casio, and $(0.41, 0.32, 0.27)$ for Panasonic. The color difference results from the difference in camera spectral sensitivities and white balance settings.

maticity values of the red squares, colors of a scene vary depending on the cameras, due to the difference of the spectral sensitivities and white-balance settings.

Spectral sensitivity can be measured by dividing the image intensity by the corresponding spectral radiance with two special equipments, spectrometer and monochromator. Vora et al (1997) measured the spectral sensitivity of two digital cameras: Kodak DCS-200 and Kodak DCS-420 in this way. Image intensity is not linearly related to scene radiance recorded at the camera sensor, it must be linearized first in order to calculate the spectral sensitivity. In this paper, the camera response function is determined by stimulating the camera with varying intensities of a single light source obtained with ND filters (neutral density filters). The image intensity of camera Kodak DCS-200 was verified to be linear over most of the visible spectra range, a linearized curve of camera Kodak DCS-420 was also developed. The spectral sensitivity for these cameras are determined by stimulating them with very narrow-band illumination produced by a monochromator, while simultaneously capturing the images and spectra by these cameras and the spectrometer, respectively. This measurement is conceptually very simple and can be very accurate. However, the equipment required to produce sufficiently intense narrow-band illumination at uniformly spaced wavelengths is expensive and not readily available.

1.1.2 Virtual Object Rendering

The virtual object can be realistically rendered by using the atmospheric turbidity. Virtual object rendering is used in many fields, especially in the field of recreating those lost cultural heritage objects. The lost objects are difficult to rebuild because of the cost and archaeological concerns. Instead of rebuilding the heritage objects, it is more convenient and economical to create them by the computer graphics models.

Fig. 1.2 shows the rendered image of the ancient capital of Asukakyo. The capital of Asukakyo does not actually exist now, as shown in Fig. 1.2 (a), however we could create the capital by the computer graphics models and insert it into the real scene by virtual object rendering. This makes it appear there is a real capital standing next to the hill's bottom as shown in Fig. 1.2 (b).

It requires the following three parameters for accurate virtual object rendering: the object shape information, the reflectance properties and the illumination. The object can be created by the computer graphics models. The reflectance properties can be manually set when creating the models. Compared to the first two parameters, the illu-

(a) A real scene.

(b) Rendered image with a virtual capital of Asukakyo inserted.

Figure 1.2: Virtual object rendering: insert the capital of Asukakyo into a real scene.

mination is not easily acquired, because it is complicated especially for outdoor objects. The most accurate method for recovering the illumination environment is to directly measure it (Debevec, 1998; Sato et al, 1999a), this method needs some equipments such as the calibrated sphere or fish-eye lens. The other way to acquire the illumination is to estimate from shadows (Sato et al, 1999b; Kakuta et al, 2004). The aerial perspective is also important for rendering the virtual object especially when it is distant from the camera. Aerial perspective is caused by the light scattering, and it models the slight color change of object. Ward (1994) models the aerial perspective effect by assuming the ambient illumination is constant, it is efficient but can not calculate correctly when the view direction or sun position changes. Ebert et al (1998) calculates the aerial perspective by the Rayleigh scattering. In their method, the object color is calculated as the linear combination of surface color and sky color.

1.1.3 Reflectance Estimation

The surface reflectance of object can be estimated from the atmospheric turbidity. With the acquisition of shape information of diffuse object, we need to estimate the absolute surface reflectance for recovering the appearance of the object under a novel illumination condition. Reflectance is the ratio of reflected light to the incident electromagnetic radiation, i.e., how much light a material will reflect regarding the incident light. This thesis defines the reflectance on each *RGB* channel; the maximum reflectance (no absorption) is (1.0, 1.0, 1.0) for (R, G, B). Figure 1.3 shows an example of surface reflectance. We can clearly see that the surface reflectance is the most essential component in terms of the object's surface property. However, we have to take the shape information into account.

For directly estimating surface reflectance properties, three components are necessary: the shape of a target object, the actual appearance of the object, and the illumination environment. Shape information and actual appearance can be obtained by range and image sensors, respectively. Two methods of recovering surface reflectance of outdoor objects measured the above three components. Yu and Malik (1998) the first who handled outdoor objects, took photographs of the sun and sky to measure their radiance distribution. As they used a normal camera, they included landmarks in each photograph so that they could use them to recover the camera pose later. Debevec et al (2004), the second and the latest to solve the outdoor problem, used a specific apparatus to measure the outside illumination. They used a mirrored sphere to image the sky

(a) Appearance.

(b) Shape and illumination.

(c) Surface reflectance.

Figure 1.3: The object's appearance is determined by its shape, surrounding illumination, and surface reflectance.

and clouds, a shiny black sphere to indicate the position of the sun, and a diffuse gray sphere to indirectly measure the intensity of the sun. These methods need elaborate procedures and do not take the inter-reflection into account. Consequently, these methods could not be applied for outdoor objects which have concave parts. Because the inter-reflection effect is not negligible for the concave objects.

For concave objects or objects with concave parts, a point of object surface receives light from both light source and other points on the surface. The latter (reflection between points on object surface) is called as inter-reflection effect. Therefore, light rays that we observe for concave object is the result of reflections repeated between surface points infinitely. It is difficult to trace back those recursive reflections from the observation.

1.2 Thesis Overview

Chapter 2 describes the proposed method for estimating the atmospheric turbidity. Turbidity is a very important factor for modeling the outdoor illumination. It is estimated by matching the brightness distribution between a sky model (Preetham et al, 1999) and an actual image. An assumption is introduced here, that the image intensity is proportional to the sky brightness no matter what the camera and the white-balance parameters are. By using this assumption, we could estimate the same turbidity from images captured by different cameras. The validation for turbidity estimation is also provided in this chapter.

Chapter 3 proposes a method for estimating the spectral sensitivity and white-balance jointly from sky images. After briefly reviewing the related work, we explains how to calculate the sky spectra by using estimated turbidity. With the pairs of image *RGB* values and corresponding spectra, the spectral sensitivity is calculated by using basis functions. The utilization of basis functions reduce the number of unknowns and makes the estimation robust. The proposed method is first evaluated with raw images, since they are affected by minimal built-in color processing; then it is evaluated with images downloaded from the Internet. An application of spectral sensitivity, namely, the color correction is introduced. The color captured by one camera could be transfered into that of another by using the color correction. We also provides the limitation of the proposed method in this chapter.

Chapter 4 describes the virtual object rendering technique based on the turbidity. Related work is introduced first, then the method for calculating the aerial perspective

effect is explained. The aerial perspective effect is caused by the particles suspended in the atmosphere and it slightly changes the object appearance especially when it is far away from the camera. Aerial perspective is calculated as the summation of in-scattered and out-scattered light along the view direction. The rendering process which takes the aerial perspective into account is also explained. This technique is applied to the Asukakyo project which restores the ancient capital of Asukakyo.

Chapter 5 describes the proposed method for estimating the surface reflectance of outdoor diffuse object from a single perspective image. After briefly reviewing the related work, the illumination estimation from perspective image is introduced. Then, the surface radiance and irradiance value is computed from the recovered illumination. The inter-reflection exists in the concave object. By assuming the object surface consists of small facets, the inter-reflection is calculated as the sum of incoming light energy from all the other points. Next, the evaluation of illumination estimation is provided and the proposed method is applied to real outdoor object.

Chapter 6 provides the summaries and contributions of this dissertation and discusses possible future research directions.

Chapter 2

Atmospheric Turbidity Estimation and its Evaluations

2.1 Introduction

The appearance of sky, *e.g.* the color and the clearness, is determined by scattering and absorption of solar irradiance due to air molecules, aerosols, ozone, water vapor and mixed gases, where some of them change according to the climate condition (Chaiwiwatworakul and Chirarattananon, 2004). Aerosols are attributed to many factors, such as volcanic eruptions, forest fires, etc.; thus, they are difficult to characterize precisely. However, a single heuristic parameter, namely turbidity, has been studied and used in the atmospheric sciences (Preetham et al, 1999). Atmospheric turbidity is defined as the ratio of optical thickness of haze as opposed to molecules. The sky appearance with different turbidity values are shown in Fig. 2.1. The higher the turbidity value is, more scattering happens in the sky, hence makes the sky appear whiter.

In this chapter, we explains the proposed method for estimating the atmospheric turbidity. We first applies the proposed method to the omni-directional images and evaluate the performance. Then we extend it to estimate the turbidity value from rectilinear images and provide the evaluations.

There are a few assumptions used in the proposed method. First, it assumes the presence of sky in the input images. Ideally, it expects a clear sky; however, it performs quite robustly even when the sky is hazy or partially cloudy. Second, it assumes that the sun direction with respect to the camera viewing direction can be extracted. If we have the camera at hand, we can arrange the camera in sun a way that we can

extract the information from the image. However, if we do not have the camera at hand (e.g., we utilize images available on the Internet), the EXIF tag (the time when the image is taken), the site geo-location and the pose of a reference object in the site are necessary to determine the camera view direction and the sun direction. While the requirement of geo-location and the reference object sounds restrictive, if we apply the method for landmark objects, such information can normally be obtained. Moreover, on-line services like Google Earth or Google Map can also be used to determine the geo-location of the site.

It should be noted that several methods of computer vision have utilized the radiometric sky model. Yu and Malik (1998) use the Perez *et al*.'s sky model (Perez et al, 1993) to calculate the sky radiance from photographs, in the context of recovering the photometric properties of architectural scenes. The work of Lalonde et al (2010) is the most similar to the proposed method, since it utilizes the visible portion of the sky and estimates turbidity to localize clouds in the sky images. However, the method (Lalonde et al, 2010) cannot be used directly for our purpose, since its optimization is based on xyY color space. To convert image RGB into xyY, a linear matrix must be estimated from known camera sensitivities and white-balance settings, which are obviously unknown in our case. Thus, instead of using xyY, we use the linear correlation between the relative intensity (i.e., the ratio of a sample point's intensity over a reference point's intensity) and relative sky brightness. By fitting the relative intensity between pixels to that of the sky model, the proposed method can estimate the turbidity, which we consider to be an improvement over the method of Lalonde et al (2010).

2.2 Turbidity Estimation from Omni-directional Image and its Evaluations

To estimate the turbidity, our basic idea is to match the brightness distribution between an actual image and the sky model proposed by Preetham et al (1999). They derive the correlation between the brightness distribution and the turbidity based on the simulations of a variety of sun positions and turbidity values. According to them, the luminance Y of the sky in any viewing direction with respect to the luminance at the zenith Y_z is given by:

$$Y = \frac{\mathcal{F}(\theta, \gamma)}{\mathcal{F}(0, \theta_s)} Y_z, \tag{2.1}$$

(a) T=2.0. (b) T=3.0. (c) T=4.0

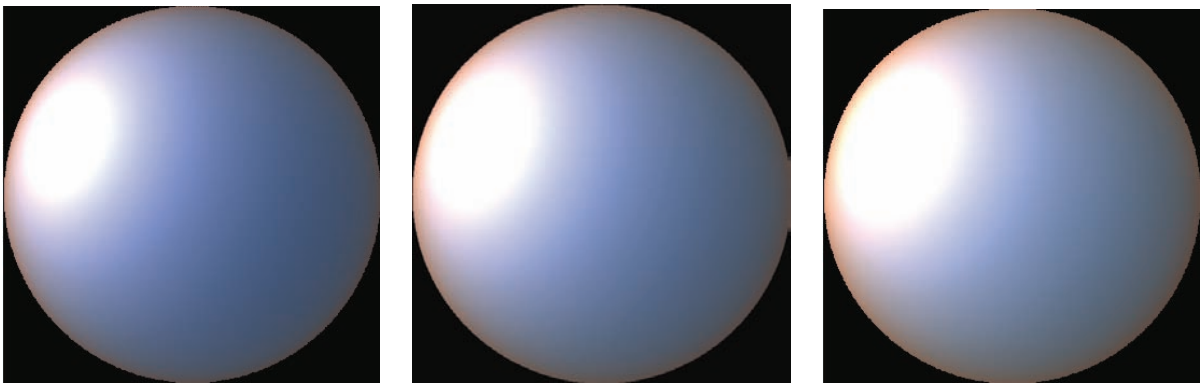

(a) T=5.0. (b) T=6.0. (c) T=7.0

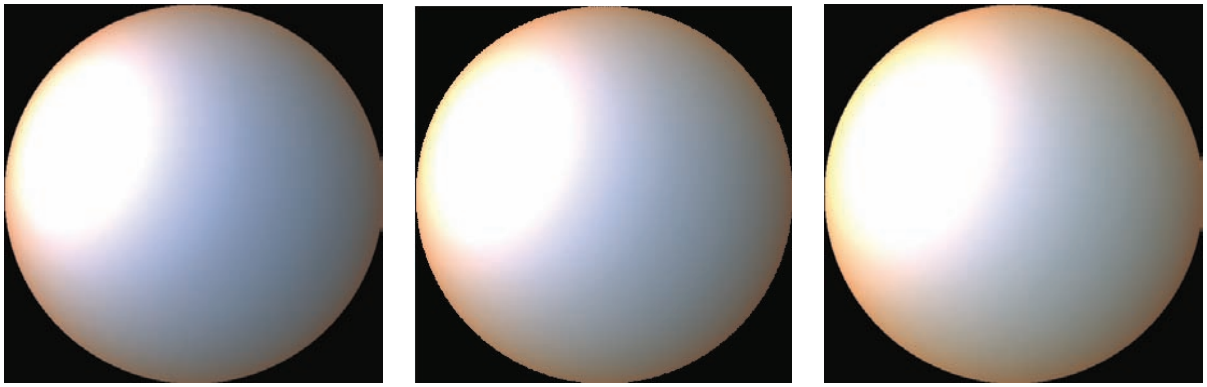

(a) T=8.0. (b) T=9.0. (c) T=10.0

Figure 2.1: Simulated sky appearance of Canon 5D camera with different turbidity values, higher turbidity value implies more scattering happens, hence makes the sky appear whiter.

where $\mathcal{F}(.,.)$ is the sky brightness distribution function of turbidity developed by Perez et al (1993), θ_s is the zenith angle of the sun, θ is the zenith angle of view direction, and γ is the angle of the sun direction with respect to the camera viewing direction, as shown in Fig. 2.2, see more details for calculating sky luminance in Appendix B.

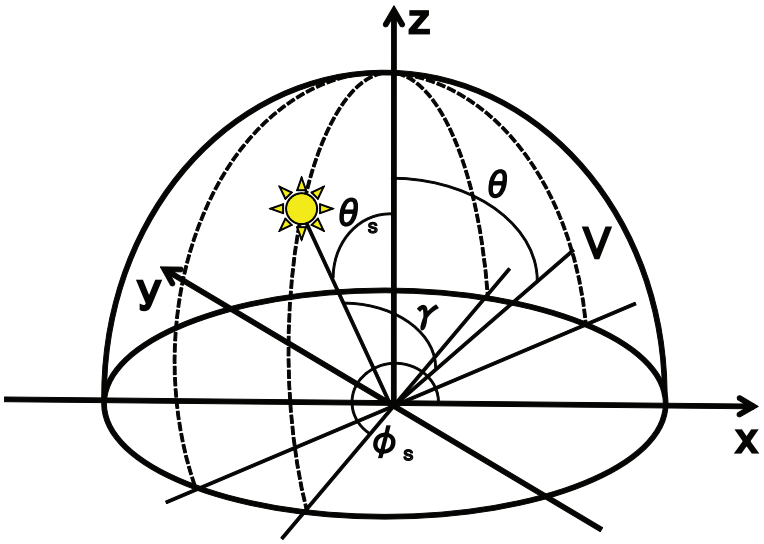

Figure 2.2: The coordinates for specifying the sun position and the viewing direction in the sky hemisphere.

Thus, to estimate turbidity (T), our method minimizes the following error function:

$$Err = \sum_{i=1}^{n} \left| \frac{Y_i(T)}{Y_{ref}(T)} - \frac{J_i}{J_{ref}} \right|, \tag{2.2}$$

where n represents the number of sample points and Y/Y_{ref} is the luminance ratio of the sky, which can be calculated from $\mathcal{F}(\theta,\gamma)/\mathcal{F}(\theta_{ref},\gamma_{ref})$, given the sun direction and the turbidity. Y_{ref} is the luminance of a reference point, and we found that it can be the zenith as in Eq. (2.1), or *any other point in the visible sky portion.* J is the total intensity of a pixel:

$$J = I_r + I_g + I_b, \tag{2.3}$$

where I_c is the image intensity for RGB color channels. J_{ref} is the total intensity of a reference pixel. Since we assume the camera's gamma function is linear, the image intensity ratio (J_i/J_{ref}) is proportional to the luminance ratio of the sky (Y_i/Y_{ref}), regardless of the camera sensitivities and white-balance settings. The error function is minimized by Particle Swarm Optimization (Kennedy and Eberhart, 1995), which is more robust than the Levenberg-Marquardt algorithm.

When the image is taken by a fish-eye lens or an omni-directional camera, the sun is visible in the captured image. Here, the pose of the camera with respect to the sun is calibrated, for instance, we assume that the optical axis of the camera is perpendicular to the ground. For calculating the sun direction, we extract the saturated area of the captured image as the circumsolar area and fit it as an ellipse. The sun position is then considered as the center of the extracted ellipse.

Having determined the sun direction, we sample the intensity distribution for the sky model and actual image. The directions are sampled from uniformly distributed patches of the upper hemisphere, the icosahedron is used to partition the hemisphere.

The brightness of sampled view directions from the sky model and the captured image are calculated, with extracted sun direction. Turbidity is estimated by matching the two brightness distributions.

The currently used sky model does not provide the equations for calculating the brightness of cloudy pixels. Therefore, when the clouds present in the captured image, we have to remove them from sampling. The RANSAC approach is used to automatically remove the clouds. Specifically, we randomly choose twenty adjacent sampled view directions as the hypothetical inliers, and estimate the turbidity value by matching the brightness distribution of these view directions. If the estimated turbidity value is too large, there is a high probability the majority of the inliers are cloudy pixels, therefore we terminate the procedure and go to the next iteration. The estimated turbidity value is used to test all the other sample view directions, the error between the sky brightness from sky model and the image intensity is calculated, if the brightness error of one view direction is smaller that the threshold, we consider it as a inlier and put it into the hypothetical inlier set. Then, the turbidity value is re-estimated from the new inlier set and calculate the error between the brightness from the sky model and actual image. This procedure is repeated until the maximum iteration. Turbidity is estimated from the inlier set which has smallest brightness error.

The performance of the proposed method for estimating the atmospheric turbidity is evaluated. We provide two evaluations for the turbidity estimation from omni-directional images: the turbidity estimation method and the accuracy of sky appearance from the sky model. The comparison between the proposed method and the previous method is also provided.

Robustness to noises The robustness of the proposed method for estimating the turbidity is evaluated. We tried two sets of input images with different turbidity

(a) 2% noise. (b) 3% noise. (c) 5% noise.

Figure 2.3: The simulated input images of Canon 5D for evaluating the robustness of the turbidity estimation method. These images are simulated with lower turbidity values (T=2.0) compared to those images in Fig. 2.4, and they have different noises. The noises are manually added to the brightness ratios.

(a) 2% noise. (b) 3% noise. (c) 5% noise.

Figure 2.4: The simulated input images of Canon 5D for evaluating the robustness of the turbidity estimation method. These images are simulated with higher turbidity values (T=4.0) compared to those images in Fig. 2.3, and they have different noises. The noises are manually added to the brightness ratios.

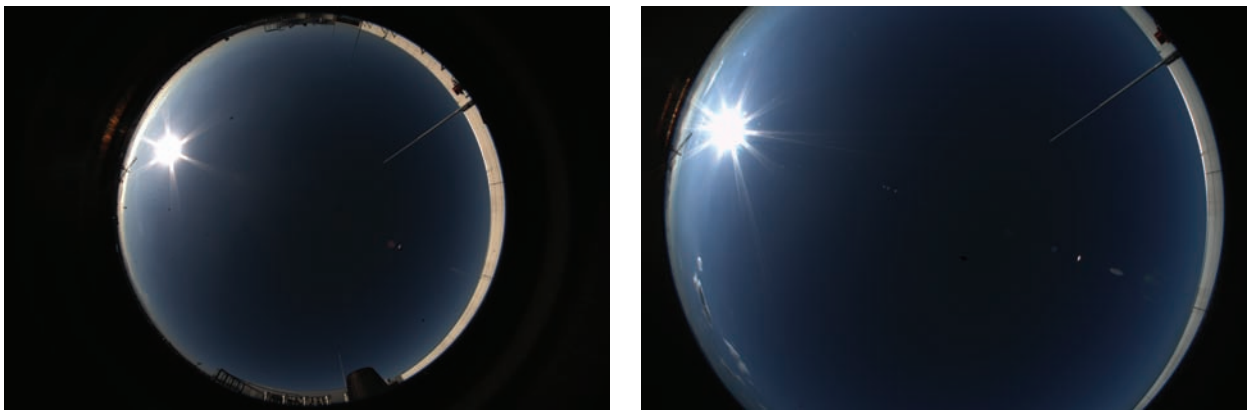

(a) Canon 5D image. (b) Nikon D1x image.

Figure 2.5: Input images for verifying the correlation between the sky luminance and image intensity. The input images are captured by two different cameras at the same time. Due to different characteristics of the spectral sensitivities, the captured images have different colors. About 120 points are uniformly sampled from these input images for the verification.

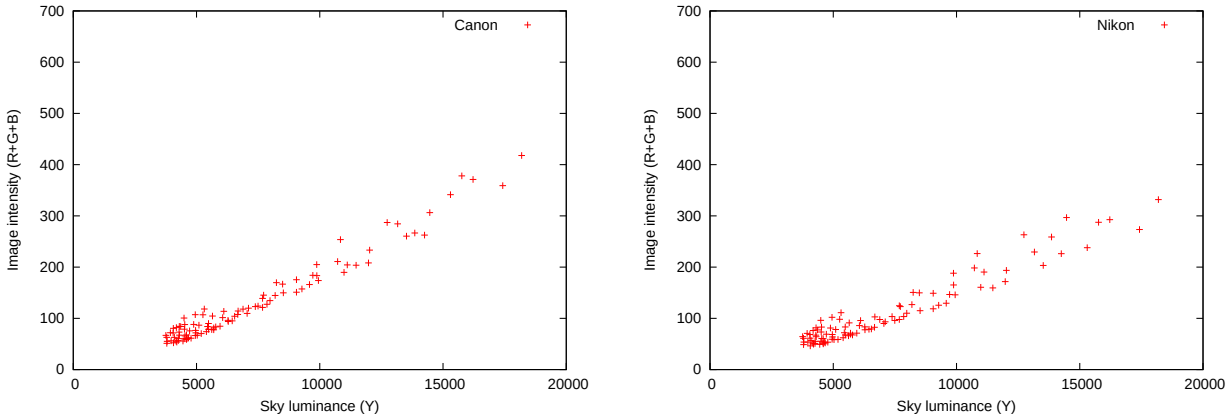

(a) Canon 5D camera. (b) Nikon D1x camera.

Figure 2.6: Verification of the correlation between sky luminance and image intensity. The horizontal axis is the sky luminance calculated from the sky model, the vertical axis is the image intensity calculated as the summation of R, G and B values.

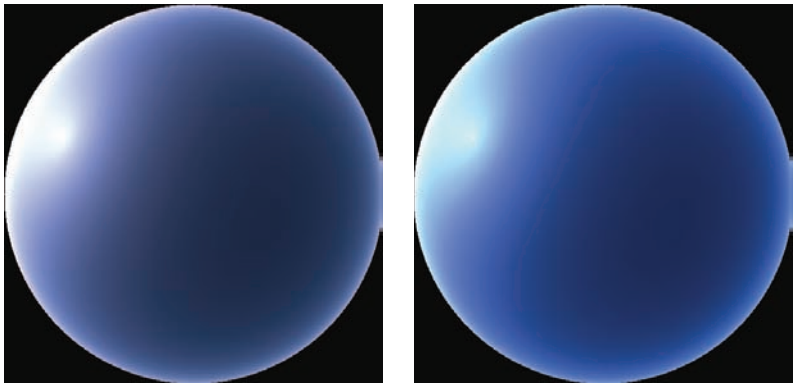

(a) WB as “Daylight”. (b) WB as “Fluorescent”.

Figure 2.7: The simulated input images of Canon 5D with different white-balance settings, these images have the same turbidity value.

(a) Input image. (b) The proposed method. (c) Lalonde et al.’s method. White-balance as “Daylight”.

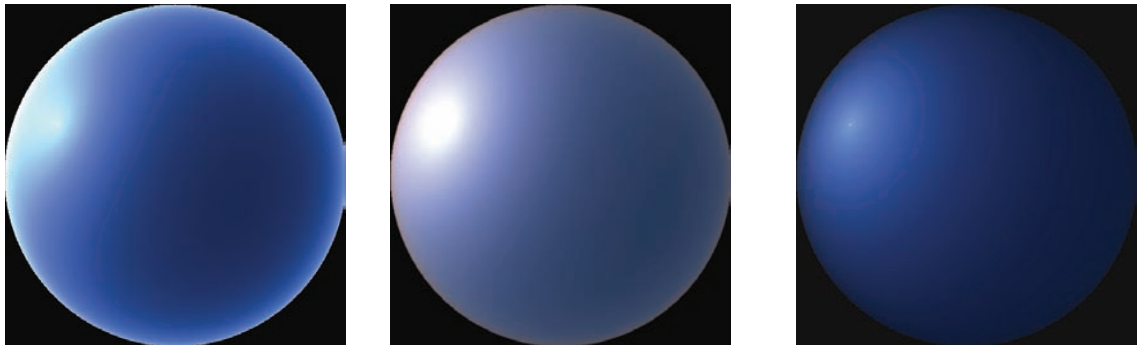

(d) Input image. (e) The proposed method. (f) Lalonde et al.’s method. White-balance as “Fluorescent”.

Figure 2.8: The comparison between the proposed method and Lalonde et al.’s method (Lalonde et al, 2010).

values, one set is simulated with turbidity value 2.0 and the other is simulated with turbidity 4.0. Then, we manually add 2%, 3% and 5% noises to the input images and estimate the turbidity from them. The input images are shown in Fig. 2.3 and Fig. 2.4, respectively. The estimated turbidity values from the first set of input images are 2.02, 2.04 and 2.07, for the second set of input images are 4.03, 4.05 and 4.07. This proves the atmospheric turbidity estimation is robust to noises.

Verification of the linear correlation between the image intensity and sky brightness Assuming we capture the same scene with different cameras or different white-balance parameters, the color of captured images are different according to different characteristics of the spectral sensitivity. Note that, following the common assumption in computational color constancy (i.e., von Kries transformation), we assume the cameras automatically multiply the spectral sensitivity of each color channel with different scaling factors according to different white-balance settings. However, the image intensity is proportional to the sky brightness regardless of the camera spectral sensitivity and white-balance settings, if knowing the camera gamma function. The image intensity is calculated as the summation of R, G and B values and the sky brightness is calculated from the estimated turbidity. In order to clarify this, we verify the linear correlation between the image intensity and sky brightness.

The verification is performed with two different cameras: Nikon D1x and Canon 5D. The input images are shown in Fig. 2.5 (a) and (b). The images are captured with the gamma turned off. We sampled about 120 points which uniformly distributed on the sky dome. The verification results are shown in Fig. 2.6. The plotted data for both cameras form a straight line. This proves the image intensity is linearly correlated with the sky brightness.

Whether the same scene provide the same turbidity value Based on the linear correlation between the image intensity and sky brightness, the proposed method obtain the same turbidity value from the same scene captured by different cameras or with different white-balance settings.

Whether the images of the same scene captured by different cameras provide the same turbidity value is evaluated. The input images are shown in Fig. 2.5. These two images are captured at the same time by Canon 5D and Nikon D1x. The estimated turbidity value is 2.2 for both images.

Whether the images captured with different white-balance parameters provide the

same turbidity is also evaluated. We simulated two images with same turbidity values (T=2.0) but different white-balance settings. The input images are shown in Fig. 2.7. Fig. 2.7 (a) shows the simulated image with the white-balance setting as "Daylight", and Fig. 2.7 (b) shows the simulated image with the white-balance setting as "Fluorescent". The estimated turbidity is 2.03 for both input images.

The comparison between the proposed method and the previous method We compared the proposed turbidity estimation method with Lalonde et al.'s method (Lalonde et al, 2010). The proposed method is based on brightness distribution, while Lalonde et al.'s is based on the xyY color space. Supposing we capture the same scene by two different cameras or with two different white-balance settings, then the calculated xyY values are different according to different RGB values. Therefore, the estimated turbidity values are different, which cannot be correct since the scene is exactly the same. The proposed method can handle this problem, because the image intensity is linearly correlated with the sky brightness. Using the two methods, we fitted the sky model to images from the estimated turbidity values. The result is shown in Fig. 2.8. Fig. 2.8 (a) and (d) are the input images simulated from sky model with turbidity 2.0 (manually set), the white-balance parameters are set as "Daylight" and "Fluorescent", respectively. The estimated turbidity values by the proposed method are 2.03 for both input images, while the turbidity values by Lalonde et al.'s method are 2.32 and 1.41. The simulated sky appearance from the estimated turbidity values are shown in Fig. 2.8 (b), (c), (e) and (f). The result of the proposed method is much more similar to the input images.

Evaluation of the accuracy of sky appearance The accuracy of the sky appearance simulated from the sky model (Preetham et al, 1999) might pose an issue in the applications, therefore we evaluated it by comparing the chromaticity produced by the sky model with the actual sky chromaticity. The result is shown in Fig. 2.9, where (a) shows the actual sky image captured by the spherical camera Ladybug2, and (b) is the simulated sky appearance from the sky model. The image intensity in (b) is adjusted so that their average becomes equal to that in (a). The red points in Fig. 2.9 show the sample points. We took 18 sample points which uniformly distributed on the upper hemisphere for comparing the chromaticity values. The comparison is summarized in Fig. 2.10. Here, the chromaticity values are calculated as $I_c/(I_r + I_g + I_b)$ where $c = \{r, g, b\}$. Looking at the 18 sampled points, the simulated sky image models the real

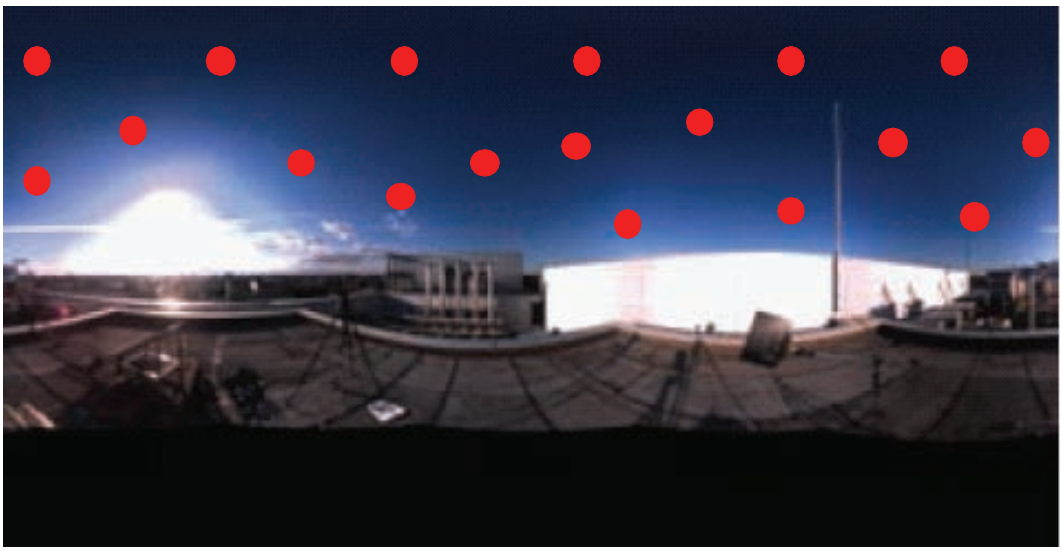

(a) Captured image.

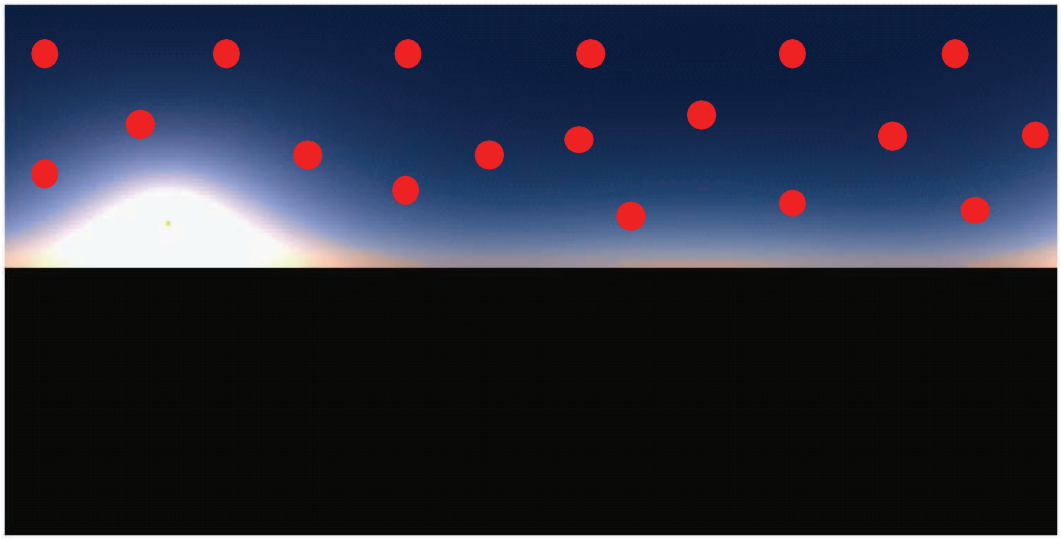

(b) Simulated sky appearance from sky model.

Figure 2.9: Comparison of the sky appearance from the captured and simulated image. The camera used was Ladybug2. The pixel values in the simulated sky image are calculated from the estimated turbidity. The red points show the eighteen sample points which uniformly distributed on the upper hemisphere.

image considerably accurate.

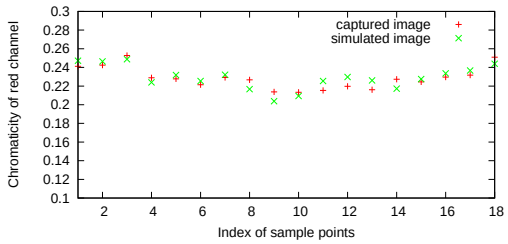

(a) Red channel.

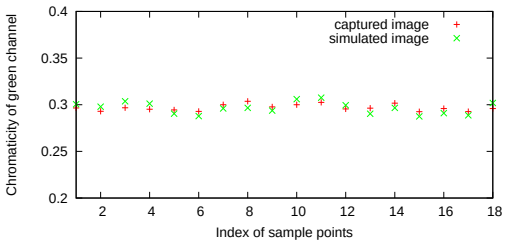

(b) Green channel.

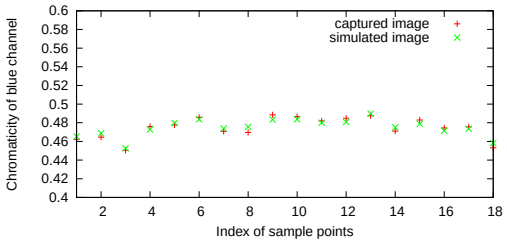

(c) Blue channel.

Figure 2.10: Numerical evaluation of the sky appearance: the comparison between captured and simulated sky image.

2.3 Turbidity Estimation from Rectilinear Image and its Evaluation

The atmospheric turbidity from rectilinear image is estimated in the same manner as from the omni-directional image, by using Eq. (2.2). However, the sun direction and camera view direction is calculated differently, because unlike the omni-directional image, the sun is usually not captured and the camera view direction is unknown for the rectilinear image.

The sun direction is calculated from the time stamp and the site geo-location (longitude and latitude), when it is not visible in the input image. The time stamp is acquired from the EXIF tag. The geo-location is obtained from Google Earth. Details for calculating the sun direction when it is not visible are provided in Appendix A.

In order to estimate the camera view direction, we collect images that include a reference object with known pose. The pose (orientation angle) of a reference object is in many cases searchable on the Internet, particularly for a landmark object, such as

the Statue of Liberty, the Eiffel tower, etc. Then, the camera view direction with respect to the reference object is recovered using a few images that contain the reference object by using the SfM (structure from motion) algorithm. Having manually acquired the pose of the reference object, the camera view direction in the world coordinate system with respect to the sun is recovered.

Google Earth can be used to estimate the pose of the reference object. The orientation angle is calculated by drawing a line between two specified points, as shown in Fig. 2.11. However, this estimation is less accurate than the actual on-site measurement (which for some landmark objects is available on the Internet). The inaccuracy in the orientation angle is 6 degrees, which in the end, decreases the accuracy of estimated turbidity value approximately 3%.

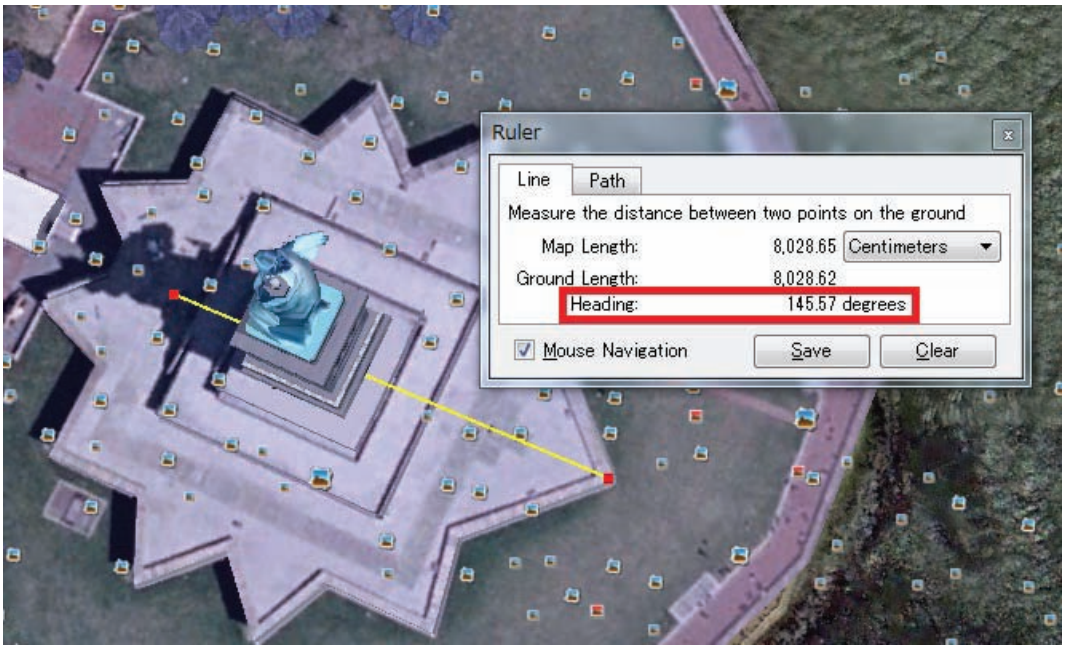

Figure 2.11: Estimating the orientation angle by Google Earth.

The same as the omni-directional image, when the cloud present in the rectilinear image, we use the RANSAC approach to automatically remove them.

The accuracy of estimated turbidity from rectilinear image greatly depends on the sun direction and camera view direction. We evaluated these two parameters. In order to verify whether the partial sky provide enough information for turbidity estimation, we compared the turbidity value estimated from part of an omni-directional image with that from the whole image.

Robustness to the sun direction estimation We evaluate the robustness of turbidity estimation by adding noises to the sun direction. For rectilinear images, the sun direction is calculated from the time stamp and the geo-location (longitude and latitude). The evaluation result is shown in Table. 2.1.

Table 2.1: Errors of the estimated turbidity values by manually adding noises to the sun direction.

Noise in the sun direction	Error of estimated turbidity
5 degree	3%
10 degree	5%
15 degree	9%

Number of images acquired for consistent camera view direction estimation For rectilinear images, the camera view direction is estimated by using the structure from motion algorithm, and this algorithm requires multiple images as input, therefore we evaluated how many images can be used for consistent estimation of camera view direction. The result is shown in Fig. 2.12, where (a) shows the result for the elevation angle (θ) and (b) shows the result for the azimuth angle (ϕ). We tried as many as 300 input images and the SfM algorithm starts to converge at about 50 images.

Robustness to the camera view direction estimation We evaluate the robustness of turbidity estimation by adding noises to the camera view direction. For rectilinear images, the camera view direction is calculated by using the structure from motion algorithm. The evaluation result is shown in Table. 2.2.

Table 2.2: Errors of the estimated turbidity values by manually adding noises to the camera view direction.

Noise in the camera view direction	Error of estimated turbidity
5 degree	4%
10 degree	7%
15 degree	11%

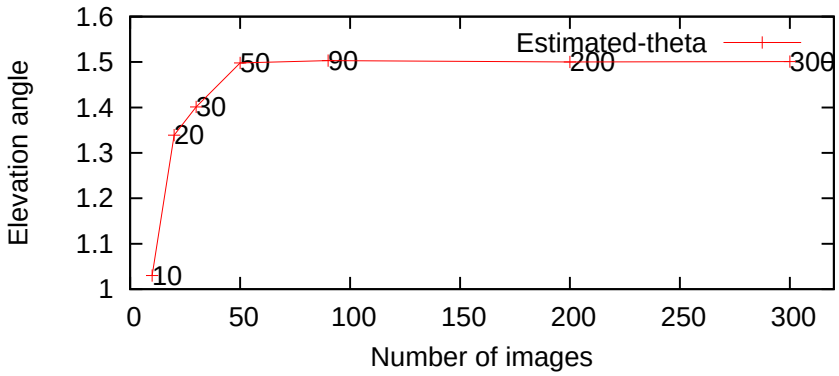

(a) Elevation angle (θ).

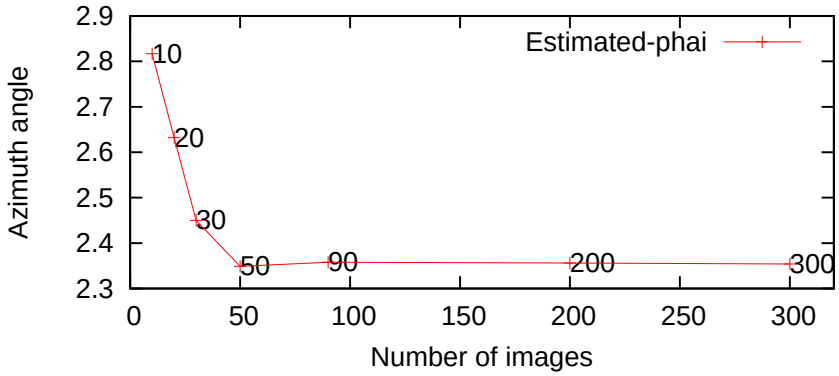

(b) Azimuth angle (ϕ).

Figure 2.12: Verification of the correlation between sky luminance and image intensity. The horizontal axis is the sky luminance calculated from the sky model, the vertical axis is the image intensity calculated as the summation of R, G and B values.

Whether the partial sky provide enough information Unlike the omni-directional image, only partial sky is captured in the rectilinear image, we evaluate whether partial sky provide enough information for the turbidity estimation. The input images are shown in Fig. 2.13, where (a) is the captured omni-directional image by the spherical camera Ladybug2, (b), (c) and (d) show different parts cropped from the omni-directional image. The sun position is extracted from the omni-directional image when estimating the turbidity from images of different parts ((b), (c) and (d)). The estimated turbidity values from images (b), (c) and (d) are the same as that from image (a).

We also verify the image size necessary for the turbidity estimation. Three images with different sizes are used in the verification. These images are cropped from the area near the center of captured omni-directional image. The input images are shown

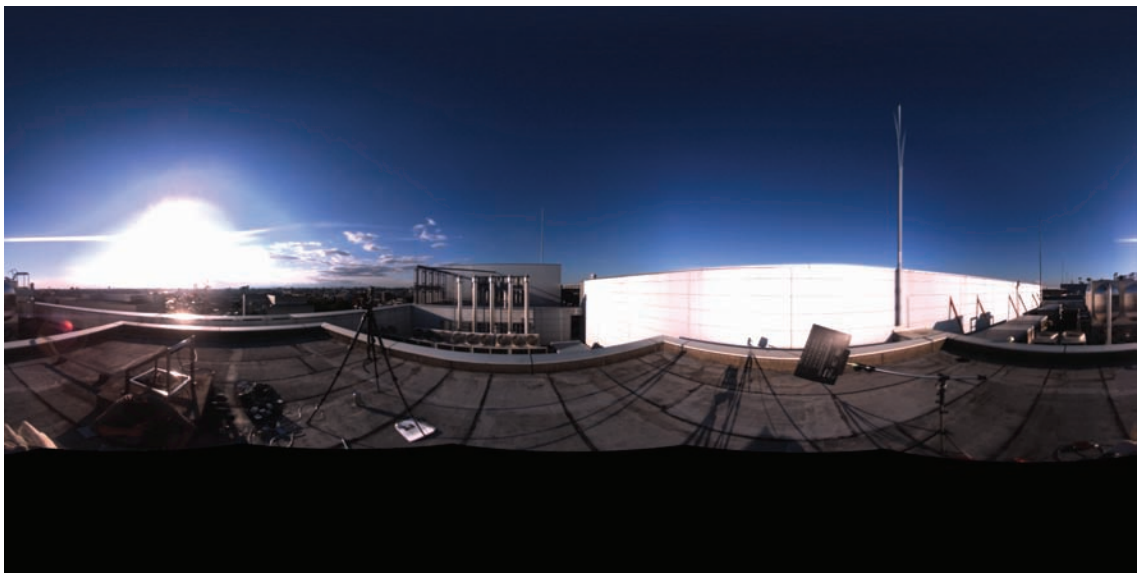

(a) Captured omni-directional image by Ladybug2.

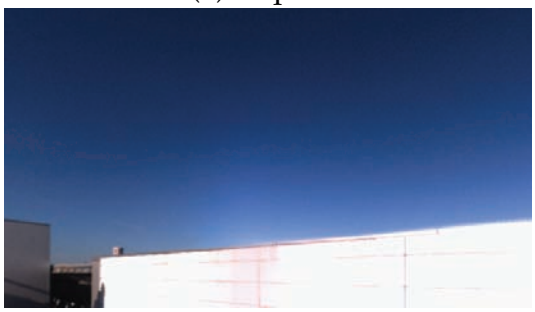

(b) Right part.

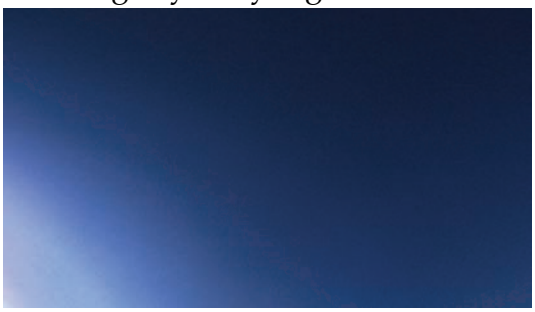

(c) Near the sun area.

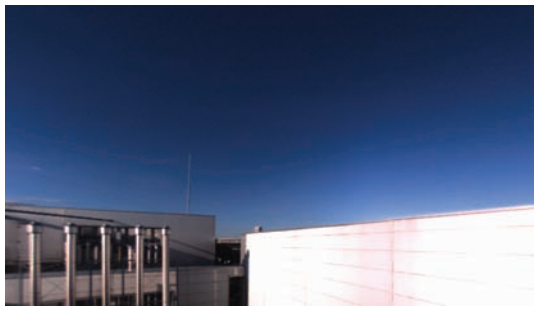

(d) Near the image center.

Different parts cut from the captured omni-directional image.

Figure 2.13: The verification of whether partial sky provide enough information for atmospheric turbidity estimation.

(a) 1000*500. (b) 600*300. (c) 200*100.

Figure 2.14: Input images with different sizes for the verification.

Table 2.3: Estimated turbidity values from input images with different sizes.

Image size	Estimated turbidity value
3800*1900	2.2
1000*500	2.21
600*300	2.23
200*100	2.25

in Fig. 2.14. The verification result is shown in Table. 2.3. The estimated turbidity value from the captured omni-directional image with the size as 3800*1900 (Fig. 2.13 (a)) is 2.2, the estimated turbidity values from the cropped image with different sizes are similar to that from the omni-directional image.

2.4 Summary

This chapter explains the proposed method for estimating the atmospheric turbidity and provides various evaluations. The atmospheric turbidity is estimated by fitting the brightness distribution of captured image to a sky model. The proposed method is first applied to the omni-directional image, and the performance is evaluated: the robustness to noises, whether it acquire the same turbidity from the same scene captured by different cameras or with different white-balance settings, the comparison between the proposed method and previous method and the accuracy of sky appearance from sky model. Then, the turbidity estimation is extended for the rectilinear image and multiple evaluations are provided: robustness to the sun direction estimation, number of images used for consistent camera view direction estimation and whether the partial sky provide enough information.

Chapter 3

Spectral Sensitivity and White Balance Estimation from Sky Images

Spectral sensitivity is calculated from the atmospheric turbidity value. Specifically, the spectral radiance is calculated from the turbidity, the image *RGB* values are obtained from the input image, the spectral sensitivity is estimated from the pairs of image *RGB* values and corresponding spectral radiance. Photometric camera calibration is often required in physics-based computer vision. There have been a number of studies to estimate camera response functions and vignetting effect from images; however less attention has been paid to camera sensitivities and white-balance settings. This is unfortunate, since those two properties significantly affect the values of image colors. Motivated by this lack of attention, we introduces a method to estimate spectral sensitivities and white-balance setting *jointly* from images. The basic idea is to use sky images from which the spectral radiance of the sky can be inferred. The turbidity is estimated by fitting the image intensity distribution to a sky model. Then the spectral radiance of the sky is calculated from the estimated turbidity. Having obtained the pairs of *RGB* values and their spectral radiance, we estimates the camera spectral sensitivity together with white balance setting. Pre-computed basis functions of camera spectral sensitivities are used in the proposed method for robust estimation. The proposed method to estimate spectral sensitivities and white balance setting is novel and practical, since, unlike the existing methods, it requires sky images without additional hardware, assuming the geo-location of the captured sky is known. Experimental results using various real images show the effectiveness of the proposed method.

3.1 Introduction

Photometrically calibrating a camera is necessary, particularly when applying physics-based computer vision methods, such as photometric stereo (Woodham, 1980; Ikeuchi, 1981; Higo et al, 2009), shape from shading (Horn, 1989; Ikeuchi and Horn, 1981; Zhang et al, 1999), color constancy (Maloney and Wandell, 1986; D'Zmura and Lennie, 1986; Forsyth, 1990; Finlayson et al, 1994; Hordley, 2006; van de Weijer et al, 2007; Tan et al, 2004; Kawakami and Ikeuchi, 2009), illumination estimation (Ramamoorthi and Hanrahan, 2001; Sato et al, 2003b; Li et al, 2003; Lalonde et al, 2009), and surface reflectance estimation (Shafer, 1985; Nayar et al, 1991; Tominaga, 1996; Sato et al, 1997; Debvec et al, 2000; Nishino et al, 2001; Hara et al, 2005; Haber et al, 2009). There have been a number of studies on automatic calibration of camera response functions and vignetting correction (Lin et al, 2004; Takamatsu et al, 2008; Kuthirummal et al, 2008). Those methods calibrate images so that obtained pixel values strictly reflect radiance of a scene.

Less attention has been paid to estimating camera sensitivities and white-balance settings, although both of them are crucial for color calibration between different types of cameras. The lack of attention is because physics-based methods usually assume images are captured by identical cameras; thus, color space used in the whole process is consistent. However, color calibration becomes an issue, when different types of cameras are used, since otherwise identical radiance will result in different pixel values. Regarding the recent popularity of digital cameras, it would be of great benefit if multiple cameras that have different characteristics can be used for inputs.

The intensity formation of each channel of colored images can be modeled as:

$$I_c = \int_\Omega L(\lambda) q_c(\lambda) d\lambda, \tag{3.1}$$

where I_c is the intensity at channel c, with $c \in \{r, g, b\}$, Ω is the range of the visible wavelength, and L is the incoming spectral radiance. $q_c = k_c q'_c$, with q'_c and k_c are the spectral sensitivity and white balance for c-color channel, respectively. In this equation, we ignore the camera gain. Note that, following the common assumption in computational color constancy (i.e., von Kries transformation), we assume cameras automatically multiply the intensity of each color channel with different scaling factors (k_c), according to different white balance settings.

Based on the last equation, our goal is to estimate q_c from given I_c. This means that from image intensity values, we intend to estimate the spectral sensitivity and white

balance setting together, without any intention to separate them ($q_c = k_c q'_c$). Note that, k_c is estimated up to a scale. Doing so, it is still possible to achieve our goal on images taken by different white balance settings, since the relative white balance values can be obtained from q_c.

In the literature, one of the basic techniques to achieve the goal is to use a monochromator (Vora et al, 1997), a special device that can transmit a selected narrow band of wavelengths of light. The method provides accurate estimation, and hence is commonly used. Other methods that do not use a monochromator require both input images and the corresponding spectral radiances (Hubel et al, 1994; Sharma and Trussell, 1993; Finlayson et al, 1998; Barnard and Funt, 2002; Ebner, 2007; Thomson and Westland, 2001).

Unlike the existing methods, in this chapter, we introduce a novel method that uses images without requiring additional devices. The basic idea of our proposed method is, first, to estimate the sky spectral radiance $L(\lambda)$ through a sky image I_c, and then to obtain the mixture of the spectral sensitivities and white balance, $q_c(\lambda)$, by solving Eq. (3.1). To our knowledge, the whole idea of this approach particularly the use of images alone is novel.

To estimate the sky spectral radiance, we calculate the turbidity of the sky from image intensity distribution, assuming the sun direction with respect to the camera viewing direction can be extracted. The calculated turbidity provides the CIE chromaticities that can then be converted to the spectral radiance using the CIE's formula.

Having the input sky image and its corresponding spectra, we estimate the spectral sensitivities by solving the linear system derived from Eq. (3.1). However, this solution can be unstable if the variances of the input colors are small, which is the case for sky images. To overcome the problem, we utilize pre-computed basis functions.

3.1.1 Related Work

Most of the existing methods of spectral sensitivity estimation (Barnard and Funt, 2002; Thomson and Westland, 2001) solve the linear system derived from Eq. (3.1), given a number of spectra and their corresponding *RGB* values. However, such estimation is often unstable, since spectral representations of materials and illumination live in a low dimensional space (Slater and Healey, 1998; Parkkinen et al, 1989), which implies that the dimension of spectra is not sufficient to recover high-dimensional spectral sensitivity information. To make the estimation stable, further constraints are required

in the optimization process, and the existing methods mostly differ in the constraints they use.

Pratt and Mancill (1976) impose a smoothing matrix on pseudo matrix inversion, compare it with the Wiener estimation, and claim that the Wiener estimation produces a better result. Hubel et al (1994) later confirm that Wiener estimation does provide a smoother result than pseudo matrix inversion. Sharma and Trussell (1993) use a formulation based on set theory, introducing a constraint set that sensitivity must satisfy, such as non-negativity, smoothness, and error variance. Finlayson et al (1998) express spectral sensitivities by a linear combination of the first 9 or 15 Fourier basis functions, and use a modality constraint such that the sensitivity becomes unimodal or bimodal. Barnard and Funt (2002) use all the constraints, replacing the absolute intensity error with the relative intensity error, and estimate the sensitivity and the camera response function at once. Ebner (2007) use an evolution strategy along with the positivity and the smoothness constraints. Thomson and Westland (2001) use the Gram-Charlier expansion (Frieden, 1983) for basis functions to reduce the dimension of spectral sensitivities. Non-linear fitting is performed in their method.

The main limitations of the mentioned methods are as follows:

1. The global optimum cannot be guaranteed.

2. The requirement of the spectral radiance is often problematic if the camera is not at hand, or if no additional devices (such as a monochromator or spectrometer) are available.

Contrary to the existing methods, in computing the spectral sensitivities we do not use an iterative technique. Importantly, our method does not require known spectral radiance.

3.2 Estimating Sky Spectral Radiance

A spectral sensitivity can be estimated if we have both image *RGB* values and the corresponding spectra, which are, respectively, I_c and $L(\lambda)$ in Eq. (3.1). Suppose that we have a set of *RGB* values and their corresponding spectra, then we can rewrite Eq. (3.1) as follows:

$$\mathbf{I} = \mathbf{q}^t \mathbf{L}, \tag{3.2}$$

where $\mathbf{I}$ is a $3 \times n$ matrix, with n representing the number of pixels. $\mathbf{L}$ is a $w \times n$ spectral matrix, with w representing the wavelengths. $\mathbf{q}$ is a $w \times 3$ camera-sensitivity matrix.

Mathematically, provided with sufficient data for **I** and **L**, we can estimate **q** by operating $\mathbf{IL}^{+}$, where $\mathbf{L}^{+}$ is the pseudo inverse of **L**. However, it becomes intractable to estimate **q** when we have an image **I** but have no spectra **L**.

To overcome this problem, we propose to infer spectra from pixel values. In fact, images of the sky provide such information. They provide clues to estimate turbidity, from which we can obtain the spectra. Having obtained the sky spectra and corresponding *RGB* values, we have **L** and **I**. Thus, we can estimate the spectral sensitivities $\mathbf{q}^{t}$ by solving Eq. (3.2).

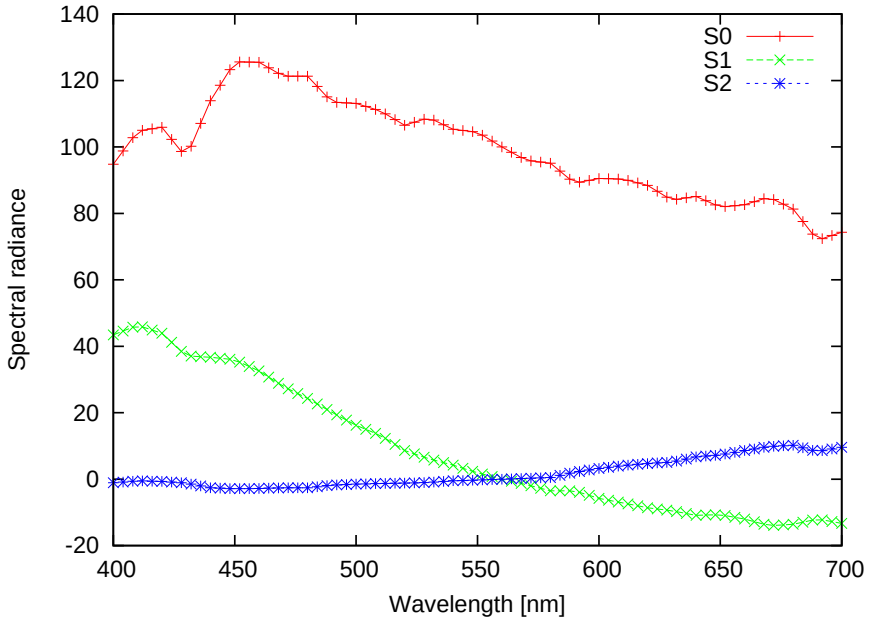

Figure 3.1: The plot of three basis functions S_0, S_1 and S_2 used for calculating the spectral radiance of sky pixels.

Preetham et al (1999) also introduce the correlation of turbidity and the CIE chromaticity (x and y). The CIE chromaticity can be calculated as follows:

$$x = x_z \frac{\mathcal{F}(\theta, \gamma)}{\mathcal{F}(0, \theta_s)}, \quad \text{and} \quad y = y_z \frac{\mathcal{F}(\theta, \gamma)}{\mathcal{F}(0, \theta_s)}, \tag{3.3}$$

where x_z and y_z represent the zenith chromaticities, and are functions of turbidity. $\mathcal{F}(.,.)$, θ_s, θ, and γ have the same meaning as in the previous subsection. For computing x and y in detail, see Appendix C.

Having obtained x and y in Eq. (3.3), spectra of the sky can be calculated using known basis functions of daylights (Judd et al, 1964; Wyszecki and Stiles, 1982). The

sky spectrum $S_D(\lambda)$ is given by a linear combination of the mean spectrum $S_0(\lambda)$ and the first two eigenvector functions $S_1(\lambda)$ and $S_2(\lambda)$. Namely,

$$S_D(\lambda) = S_0(\lambda) + M_1 S_1(\lambda) + M_2 S_2(\lambda), \tag{3.4}$$

where scalar coefficients M_1 and M_2 are determined by chromaticity values x and y. Computing M_1 and M_2 from x and y is given in Appendix C. The data of three basis functions $S_0(\lambda)$, $S_1(\lambda)$ and $S_2(\lambda)$ can be found in (Judd et al, 1964; Wyszecki and Stiles, 1982), and the plot is shown in Fig. 3.1.

3.3 Estimating Spectral Sensitivity

Given a number of input image *RGB* values and the corresponding spectra, the spectral sensitivities can be estimated using the matrix inversion as in Eq. (3.2). However, the rank of the matrix $\mathbf{L}$ has to be at least w, to calculate the pseudo inverse $\mathbf{L}^+$ stably. In our case, the representation of the sky spectral radiance is three dimensional since we calculate the spectral radiance using the basis functions in Eq. (3.4). This means that the direct matrix inversion method would produce erroneous results.

To solve the problem, we propose to use a set of basis functions computed from known spectral sensitivities. In many cases, the spectral sensitivities of cameras are different but their variances will not be extremely large, meaning that their representation may lie in a very low dimensional space, similar to the illumination basis functions (Slater and Healey, 1998). Basis functions can reduce the dimension and thus the number of unknowns. Therefore, this method generally provides robust and more accurate results than the direct matrix inversion method.

3.3.1 Estimation Using Basis Functions

Spectral sensitivity can be robustly estimated from Eq. (3.2) by using the basis functions of spectral sensitivity owing to its low dimensionality. Let us assume that the spectral sensitivity can be approximated by a linear combination of a small number of basis functions:

$$q_c(\lambda) = \sum_{i=1}^{d} b_i^c B_i^c(\lambda), \tag{3.5}$$

where d is the number of the basis functions, b_i^c is the coefficient and $B_i^c(\lambda)$ is the basis function with $c \in \{r, g, b\}$.

By substituting the equation into Eq. (3.1), we can derive

$$\begin{aligned} I_c &= \int_\Omega L(\lambda) \sum_{i=1}^{d} (b_i^c B_i^c(\lambda)) d\lambda \\ &= \sum_{i=1}^{d} b_i^c \int_\Omega L(\lambda) B_i^c(\lambda) d\lambda \end{aligned} \tag{3.6}$$

where I_c is the image intensity for RGB channels.

If we use another notation E_i^c to describe the multiplication of spectrum data and basis function of spectral sensitivity, namely,

$$E_i^c = \int_\Omega L(\lambda) B_i^c(\lambda) d\lambda, \tag{3.7}$$

then by substituting Eq. (3.7) into (3.6), we obtain

$$I_c = \sum_{i=1}^{d} b_i^c E_i^c. \tag{3.8}$$

Now, let us suppose that we have N set of data (image intensities and spectra). By using the matrix notation, we can describe Eq. (3.8) as

$$\mathbf{I} = \mathbf{bE}, \tag{3.9}$$

where I is the $N \times 3$ matrix, $\mathbf{b}$ is the $3 \times d$ coefficient matrix, and E is the $d \times N$ matrix. Consequently, this coefficient matrix $\mathbf{b}$ can be expressed as

$$\mathbf{b} = \mathbf{IE}^+ \tag{3.10}$$

where $\mathbf{E}^+$ is the pseudo inverse of the matrix $\mathbf{E}$.

3.3.2 Basis Functions from a Database

The rank of the multiplication matrix ($\mathbf{E}$) has to be larger than the number of basis functions (d) to make the estimation robust. Since the estimated spectral radiance is at most rank three, we use three-dimensional basis functions for the spectral sensitivity estimation.

In order to extract the basis functions, we collected several digital cameras to make a database and measured their spectral sensitivities, including a few spectral sensitivities drawn from the literature (Vora et al, 1997; Buil, 2005). Cameras included

in the database are Sony DXC 930, Kodak DCS 420, Sony DXC 9000, Canon 10D, Nikon D70, and Kodak DCS 460. Those used for the experiments are not included. This spectral sensitivity database is publicly available at our website (Zhao, 2011). By applying principal component analysis, the eigenvectors can be extracted.

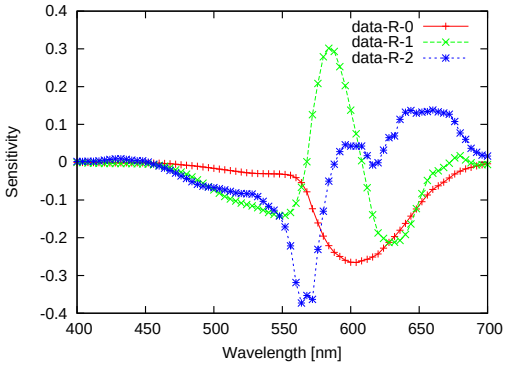

(a) Red channel.

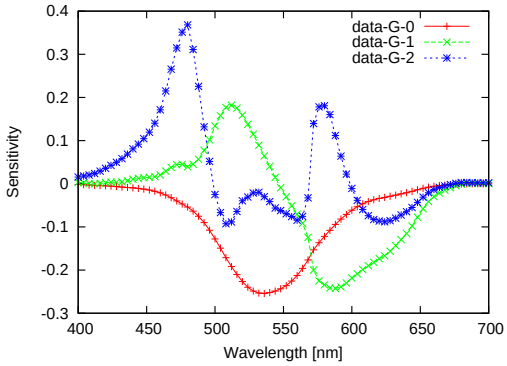

(b) Green channel.

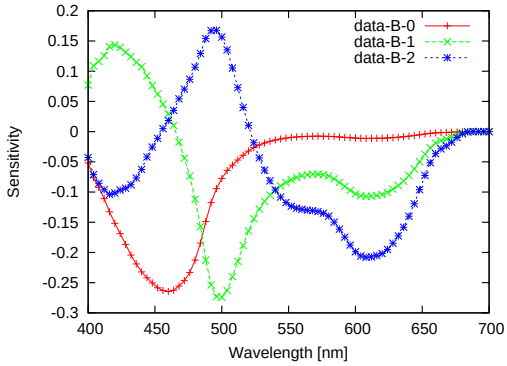

(c) Blue channel.

Figure 3.2: Extracted basis functions of red, green and blue channels from our sensitivity database.

The percentages of eigenvalues for each color channel are shown in Table 3.1. The sum of the first three eigenvalues is about 93% for all three channels. This means that the first three vectors cover 93% information of the database. Based on this, the first three eigenvectors are used as basis functions, which are shown in Fig. 3.2.

3.4 Experimental Results

In our experiment, we first evaluated our method with raw images, since they are affected by minimal built-in color processing. The raw images are captured by three

Table 3.1: The percentages of the first four eigenvalues for each color channel.

Eigenvalues			Percentage %		
R	G	B	R	G	B
6.52	8.58	6.60	68.1	73.6	61.7
1.81	1.54	1.98	19.0	13.2	18.4
0.50	0.72	1.22	5.18	6.16	11.3
0.34	0.36	0.44	3.57	3.08	4.07

different cameras: Ladybug2, Canon 5D, and Nikon D1x. In this evaluation, we tested both omni-directional images and perspective images, which were either rectified from an omni-directional image or taken by a camera with a normal lens.

Second, we evaluated our method with images downloaded from the Internet. The images are captured by three different cameras: Canon EOS Rebel XTi, Canon 5D, Canon 5D Mark II. The color post-processing is compensated by a calibration method (Chakrabarti et al, 2009) that considers the camera-response function and color matrix conversion, and then applies calibrated images for spectral sensitivities and white-balance estimation.

3.4.1 Raw Images

3.4.1.1 Omni-directional Images

Our proposed method was first evaluated with images of clear sky of the three different cameras: Ladybug2, Canon 5D, and Nikon D1x. Ladybug2 captures the panorama image, the fish-eye lens was attached to Canon 5D and Nikon D1x. Therefore, the whole upper hemisphere was captured. Fig. 3.3 (a), (d), and (g) show the captured images. The images were taken almost at the same time, with the gamma function turned off. The method proposed by Barnard and Funt (2002) was implemented for comparison. In their method, the spectral sensitivity is optimized from relative intensity error along with the constraint sets. We used the same input data for both their and our method. This input data is the estimated sky spectra from our proposed method.

Fig. 3.4 (a), (d), and (g) show the estimated results. The ground-truth of these cameras was measured by using a monochromator. Our method was able to estimate the same turbidity values, around 2.2 ± 0.02 through different cameras with different *RGB* values.

The mean error and RMSE of both our and Barnard *et al*.'s methods are shown in Table 3.2, which evaluates their performance. Here, the maximum values of estimated spectral sensitivities are normalized to 1.0. The largest mean error of our method is less than 3.5%, while that of Barnard *et al*.'s is 7%. Our method also has a smaller standard deviation. The result of our method achieves higher accuracy because it uses the basis functions extracted from collected spectral sensitivities of different cameras. The experiment shows our method works well for clear sky images.

The method was also evaluated with different sky conditions as shown in Fig. 3.3: (b) partially cloudy sky, (c) thin cloudy sky, (e) hazy sky, and (h) significantly cloudy sky. For Fig. 3.3 (b) and (c), a RANSAC-type algorithm, was used to exclude the outliers (cloud pixels). For other images, we estimated sky turbidity from the sample pixels by PSO (particle swarm optimization) (Kennedy and Eberhart, 1995), because it is likely to reach the global optimum. Estimated turbidity for those weather conditions were about 2, 3, 4 and 12, respectively. The recovered spectral sensitivities are shown in Fig. 3.4 (b), (c), (e), and (h). A large error occurs in (h) because the whole sky is covered by thick cloud that does not fit Preetham *et al*.'s model.

In the experiment, we also wanted to know whether the proposed method is effective in estimating the white balance setting by using two images taken from the same camera (thus the same spectral sensitivities) but different white balance settings. Fig. 3.3 (e) and (f) show such images. The estimated spectral sensitivities are shown in Fig. 3.4 (e) and (f). As expected, the shape of the spectral sensitivities are the same, and they differ only in the magnitude.

3.4.1.2 Perspective images

We tested our method with perspective images (images rectified from omni-directional images) and images taken from ordinary cameras. To show that narrower field-of-view also works with the method, first, we used the rectified spherical image shown in Fig. 3.3 (i). This image is a part of Fig. 3.3 (a). The recovered sensitivity is shown in Fig. 3.4 (i). The performance did not change much compared to (a), although only partial sky is visible. We tested three different directions in (a), and had similar results from them. The estimated sun position in (a) was used here.

Second, we show that the method can handle images where the sun is not visible and the camera poses are unknown. Fig. 3.5 (a) shows captured images with a reference object whose pose and geo-location are known. We captured 16 images in total, and recovered each camera pose with respect to the reference object. The sun position was

(a) Clear. (b) Partially cloudy. (c) Thin cloudy.

Ladybug2.

(d) Clear. (e) Hazy plus "Daylight" WB. (f) Hazy plus "Cloudy" WB.

Canon 5D.

(g) Clear. (h) Significantly cloudy. (i) Rectified image.

Nikon D1x. Ladybug2.

Figure 3.3: Various sky conditions captured by three different omni-directional cameras: the top row shows the images of Ladybug2, the second row shows the images of Canon 5D. The first two images of the bottom row are captured by Nikon D1x and the third one is rectified from image (a).

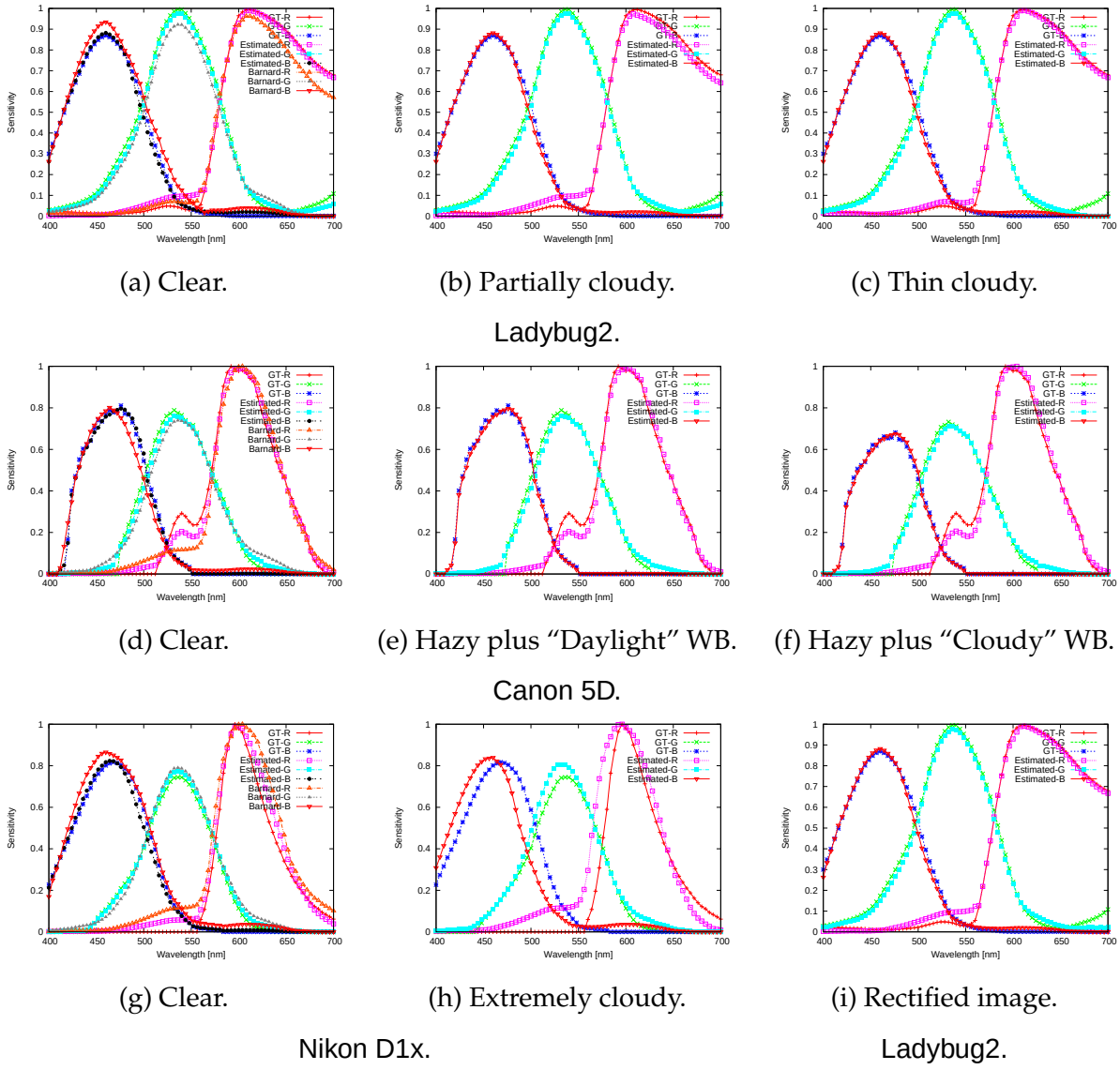

(a) Clear. (b) Partially cloudy. (c) Thin cloudy.

Ladybug2.

(d) Clear. (e) Hazy plus "Daylight" WB. (f) Hazy plus "Cloudy" WB.

Canon 5D.

(g) Clear. (h) Extremely cloudy. (i) Rectified image.

Nikon D1x. Ladybug2.

Figure 3.4: Sensitivity estimation results using the input images shown in Fig. 3.3. Ground-truth ("GT"), estimated sensitivities of our method ("Estimated"), and the method of Barnard and Funt (2002) ("Barnard") are shown for three different cameras: Ladybug2, Canon 5D and Nikon D1x.

Table 3.2: Evaluation of estimated spectral sensitivity from omni-directional images: Mean error and RMSE.

Different	Mean error		RMSE	
Cameras	Ours	Barnard's	Ours	Barnard's
Canon 5D(R)	0.0235	0.0469	0.0317	0.0734
Canon 5D(G)	0.0190	0.0380	0.0247	0.0594
Canon 5D(B)	0.0085	0.0276	0.0140	0.0411
Ladybug2(R)	0.0193	0.0378	0.0258	0.0621
Ladybug2(G)	0.0120	0.0462	0.0225	0.0525
Ladybug2(B)	0.0145	0.0341	0.0203	0.0512
Nikon D1x(R)	0.0343	0.0701	0.0359	0.0921
Nikon D1x(G)	0.0136	0.0285	0.0168	0.0431
Nikon D1x(B)	0.0162	0.0311	0.0263	0.0401

(a) Rectilinear images.

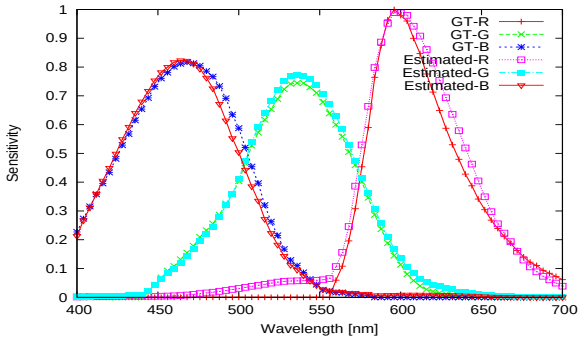

(b) Estimated result.

Figure 3.5: Rectilinear images with a reference object from multiple views of Nikon D1x and estimated spectral sensitivity. We captured about 30 images and six of them are shown in (a). These images are used for recovering the camera parameters. The spectral sensitivity estimation only requires any one of the captured images.

estimated from the time stamp in the EXIF tag. The gamma function was turned off in the experiment. The estimated spectral sensitivity is shown in Fig. 3.5 (b).

3.4.2 In-camera Processed Images

General images such as those available on the Internet are much more problematic compared with the images we tested in Section 3.4.1, since the camera response function (gamma function) has to be estimated and the images are usually taken by cameras that have built-in color processing (Ramanath et al, 2005).

We evaluated our method with images downloaded from the Internet, captured by three different cameras: Canon EOS Rebel XTi, Canon 5D, Canon 5D Mark II. Fig. 3.6 shows these images of the Statue of Liberty downloaded from a photo-sharing site. These images are JPEG compressed and are taken with internal camera processing. Chakrabarti et al (2009) invented an empirical camera model which converts the JPEG image back to raw image. We implemented the method described in this paper to photometrically calibrate the camera (response function and internal color processing). The camera pose and the sun direction were estimated in the same manner as in the previous experiment (Fig. 3.5 (a)), while 187 images were used here. The method was also evaluated by different sky conditions: clear skies (Fig. 3.6 (a), (g), and (i)), cloudy skies (Fig. 3.6 (c) and (e)), and hazy sky (Fig. 3.6 (k)).

The estimated spectral sensitivities are also shown in Fig. 3.6. Evaluation result are shown in Table 3.3. The mean error for *RGB* channels is larger than the results from omni-directional images because of the residual errors of the internal color processing, the estimation of the response function, and data compression.

We used the Macbeth color chart to evaluate the accuracy of estimated spectral sensitivity. Specifically, we captured the spectral radiance of the first 18 color patches and used estimated spectral sensitivity to predict the image intensity. The predicted and captured image intensity is plotted into 2D space. We found that if the error of estimated spectral sensitivity is less than 5%, then the plotted data forms an almost perfect straight line. This proves that the sensitivity estimation achieves high accuracy.

3.5 Applications of Estimated Spectral Sensitivity

The estimated spectral sensitivity is used for many applications, such as correcting the color between different cameras, rendering the virtual object and recovering

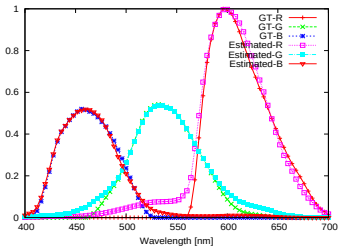

(b) Result from Input 1.

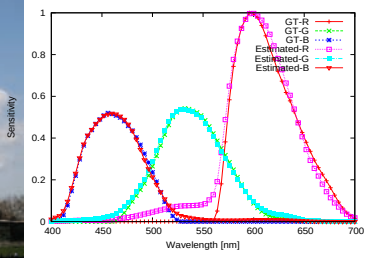

(d) Result from Input 2.

(a) Input 1. (c) Input 2.

Canon EOS Rebel XTi.

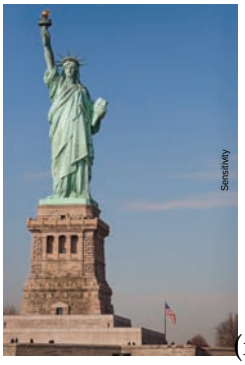

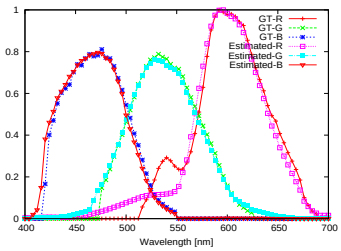

(f) Result from Input 3.

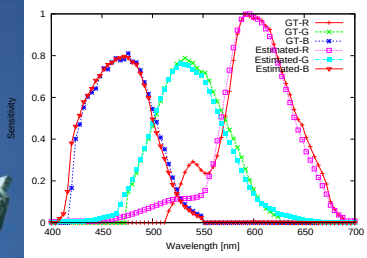

(h) Result from Input 4.

(e) Input 3. (g) Input 4.

Canon 5D.

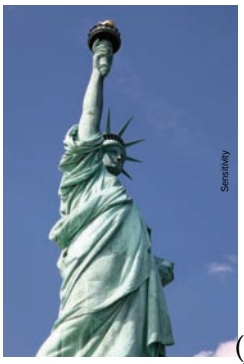

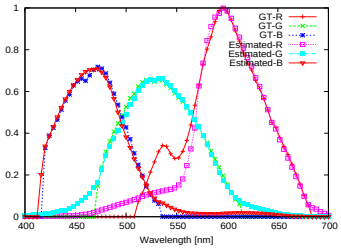

(j) Result from Input 5.

(k) Input 6.

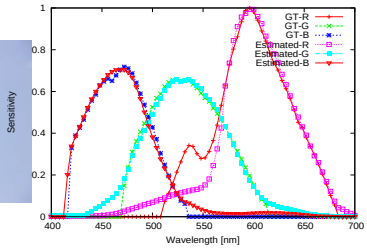

(l) Result from Input 6.

(i) Input 5.

Canon 5D Mark II.

Figure 3.6: Sensitivity estimation results on the images downloaded from the Internet. Three different cameras were tested: the top row shows the images of Canon EOS Rebel XTi, the second row shows those of Canon 5D, and the bottom row shows those of Canon 5D Mark II. (a), (c), (e), (g), (i), (k) are the input images, and (b), (d), (f), (h), (j), (l) are the corresponding results. All input images are downloaded from the Internet. ("GT") in the graphs refers to the ground truth, and ("Estimated") refers to the estimated sensitivities.

Table 3.3: Evaluation of estimated spectral sensitivity from Internet images: Mean error and RMSE.

Different input images	Mean error	RMSE
Canon Rebel XTi 1 (R)	0.0359	0.0501
Canon Rebel XTi 1 (G)	0.0161	0.0230
Canon Rebel XTi 1 (B)	0.0108	0.0142
Canon Rebel XTi 2 (R)	0.0370	0.0511
Canon Rebel XTi 2 (G)	0.0121	0.0181
Canon Rebel XTi 2 (B)	0.0097	0.0146
Canon 5D 1 (R)	0.0414	0.0579
Canon 5D 1 (G)	0.0175	0.0262
Canon 5D 1 (B)	0.0151	0.0351
Canon 5D 2 (R)	0.0410	0.0578
Canon 5D 2 (G)	0.0223	0.0327
Canon 5D 2 (B)	0.0151	0.0348
Canon 5D Mark II 1 (R)	0.0406	0.0642
Canon 5D Mark II 1 (G)	0.0220	0.0329
Canon 5D Mark II 1 (B)	0.0176	0.0237
Canon 5D Mark II 2 (R)	0.0388	0.0634
Canon 5D Mark II 2 (G)	0.0206	0.0326
Canon 5D Mark II 2 (B)	0.0175	0.0235

the outdoor illumination environment. The details for correcting the color between different cameras are provided here.

One of the applications of estimating spectral sensitivities and white balance setting is to correct the colors between different cameras. The purpose of this color correction is similar to color transfer (Reinhard et al, 2001). Thus, we intended to compare the results of color correction using our estimated spectral sensitivities and white balance with those of color transfer.

Before showing the comparisons, here we briefly discuss our color correction. By discretizing Eq. (3.1) and using matrix notation, we can rewrite it as follows:

$$\mathbf{I}_{n\times 3} = \mathbf{L}_{n\times w}\mathbf{Q}_{w\times 3}\mathbf{B}_{3\times 3} = \mathbf{E}_{n\times 3}\mathbf{B}_{3\times 3}, \tag{3.11}$$

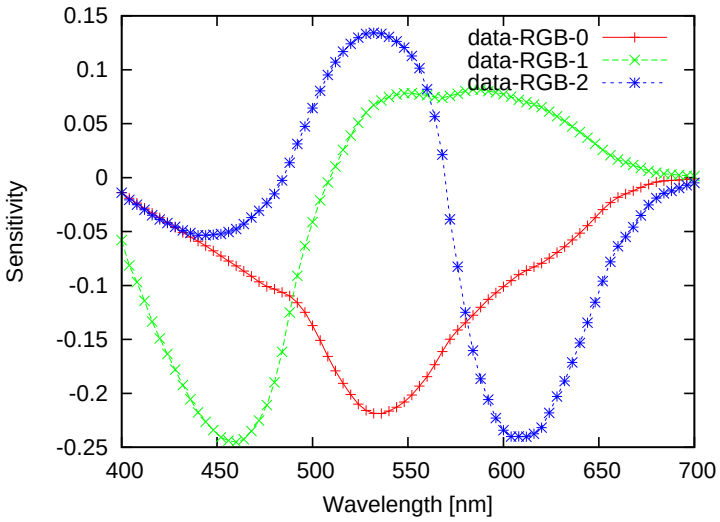

Figure 3.7: Extracted basis functions common for all three channels from our sensitivity database.

where $\mathbf{I}$ is the intensity matrix, $\mathbf{L}$ is the matrix of spectral radiance, $\mathbf{Q}$ is the matrix of basis functions for spectral sensitivities, $\mathbf{B}$ is the coefficient matrix, and $\mathbf{E}$ is the multiplication of $\mathbf{L}$ and $\mathbf{Q}$. Note that the basis functions used here are different from those extracted in Sec. 3.3.2, in the sense that now we use the same basis for the three color channels. n is the number of surfaces, and w is the number of sampled wavelengths.

Suppose we have an image captured by one camera, denoted as $\mathbf{I}_1 = \mathbf{E}\mathbf{B}_1$, then the same scene captured by another camera is expressed as:

$$\mathbf{I}_2 = \mathbf{E}\mathbf{B}_2 = \mathbf{I}_1\mathbf{B}_1^{-1}\mathbf{B}_2. \tag{3.12}$$

Since $\mathbf{B}_1$ and $\mathbf{B}_2$ are computable if both sensitivities are known, color conversion from one image to another is possible via the above equation. Fig. 3.7 shows extracted basis functions common for the three channels.

Color correction result for the Statue of Liberty is shown in Fig. 3.8. In the figure, (a) and (b) show the source and target images, and (d) is the result of our method. We also implemented Reinhard *et al.*'s color transfer algorithm (Reinhard et al, 2001) for comparison. Fig. 3.8 (c) is the result of their method. Since the proposed method is based on the physical cameras' characteristics, it produces visually better results, *e.g.*, in the chest area, or in the platform of the statue.

The quantitative evaluation is shown in Fig. 3.9. We sampled six points as shown

(a) Source. (b) Target. (c) Color transfer. (d) Our method.

Figure 3.8: Color correction between different cameras: (a) is the source image captured by Canon 5D, (b) is the target image captured by Canon EOS Rebel XTi, (c) shows the result of color transfer (Reinhard et al, 2001), (d) shows the result of our color correction method.

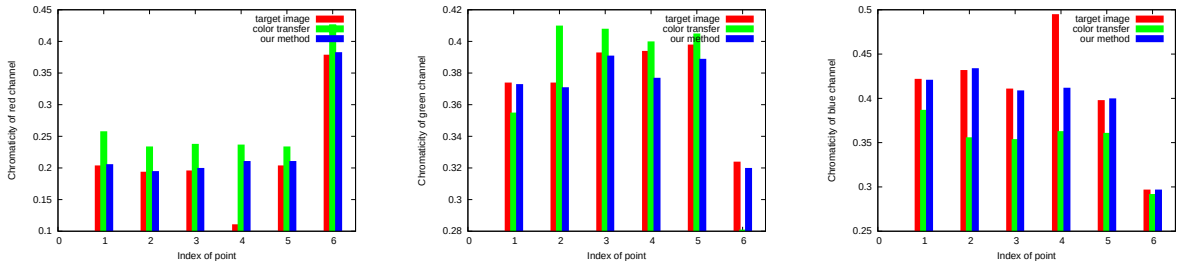

(a) Red channel. (b) Green channel. (c) Blue channel.

Figure 3.9: Chromaticity evaluation between images shown in Fig. 3.8. "target image," "color transfer," and "our method" represent chromaticities of (b), (c), and (d) in Fig. 3.8. The result of our method is close to the target image except for point 4, because it lies in the shadow region of the target image (b).

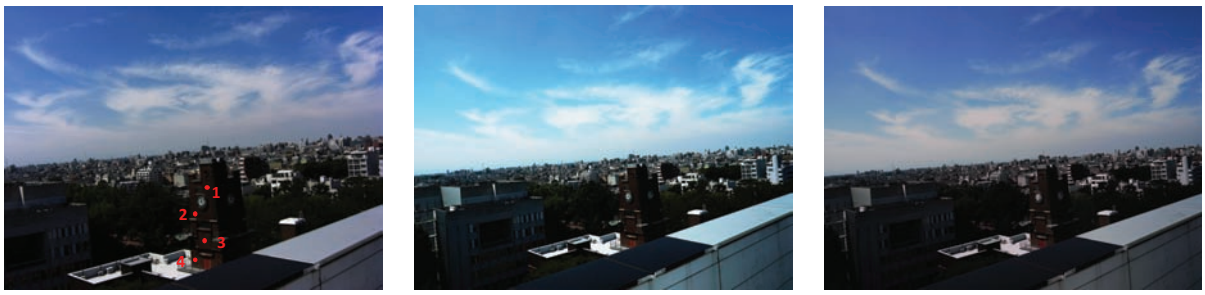

(a) Linearized Casio. (b) Linearized Panasonic. (c) Color correction result.

Figure 3.10: Color correction between different cameras: (a) is the target image captured by Casio, (b) is the source image captured by Panasonic, (c) shows the color correction result from Panasonic (b) to Casio (a).

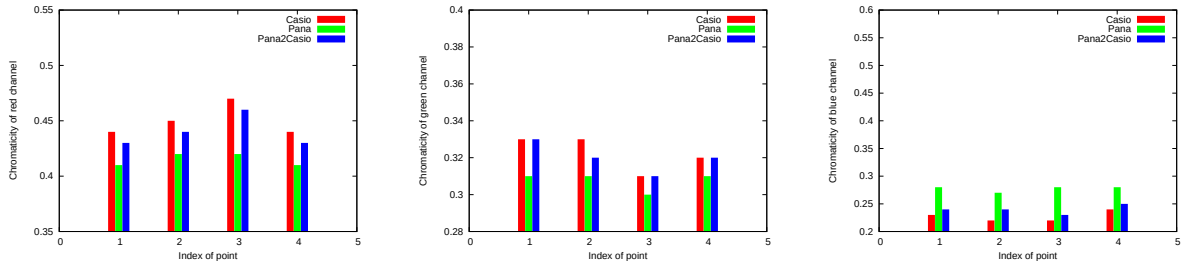

(a) Red channel. (b) Green channel. (c) Blue channel.

Figure 3.11: Chromaticity evaluation between images shown in Fig. 3.10. "Casio," "Pana," and "Pana2Casio" represent chromaticities of (a), (b), and (c). The performance is evaluated on four points.

(a) Linearized Casio. (b) Linearized Canon. (c) Color correction result.

Figure 3.12: Color correction between different cameras: (a) is the target image captured by Casio, (b) is the source image captured by Canon, (c) shows the color correction result from Canon (b) to Casio (a).

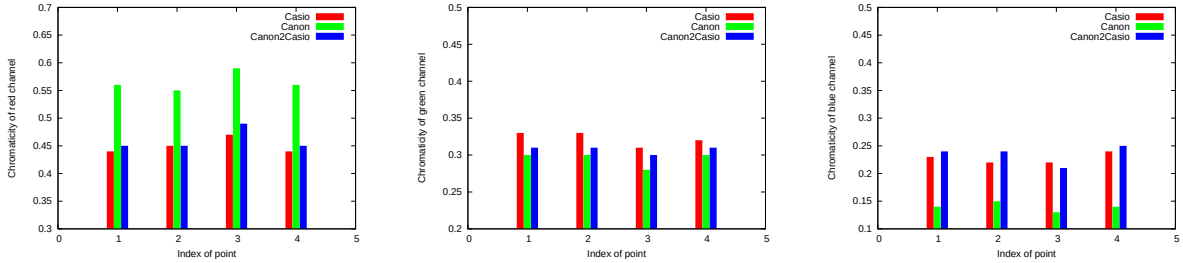

(a) Red channel. (b) Green channel. (c) Blue channel.

Figure 3.13: Chromaticity evaluation between images shown in Fig. 3.12. "Casio," "Canon," and "Canon2Casio" represent chromaticities of (a), (b), and (c). The performance is evaluated on four points.

in Fig. 3.8 (a), and compared the chromaticity of those points of three images (b), (c), and (d): In Fig. 3.9, "target image," "color transfer," and "our method" represent the chromaticity of the target image, the result of color transfer, and the proposed color correction. Chromaticity is calculated as $I_c/(I_r + I_g + I_b)$. The chromaticity values of the proposed method are close to those of the target image, except for the point 4, a point lies in the shadow region of the target image. The proposed color correction method performs better because it is based on estimated camera spectral sensitivities. Meanwhile, the color transfer method by Reinhard et al. is based on the Gaussian color distribution of two images.

Note that, while Fig. 3.8 (b) was captured only one hour later than (a), their color appears significantly different. By assuming that the illumination did not change that much, the difference must be due to the difference of the camera properties, such as spectral sensitivities and white balance. Thus, we consider that the proposed method is useful in applications where color calibration between cameras is necessary.

Another two examples of color correction for the clock tower are shown in Fig. 3.10 and 3.12. Here, (a) and (b) are gamma-corrected images from Fig. 1.1, and (c) shows the result of our method for two different cameras. Quantitative evaluations are shown in Fig. 3.11 and 3.13. "Casio," "Pana," "Pana2Casio," "Canon," and "Canon2Casio" represent the chromaticity values of Casio, Panasonic, color corrected from Panasonic to Casio, Canon, and color corrected from Canon to Casio, respectively. The performance is evaluated on the four sample points as shown in Fig. 3.10 (a) and 3.12 (a). We find that our method achieved high accuracy.

(a) Original.

(b) Manual color balance.

(c) Manual color adjustment.

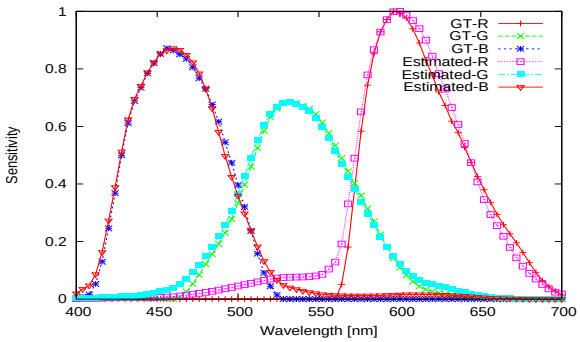

(d) Estimated spectral sensitivity from (b).

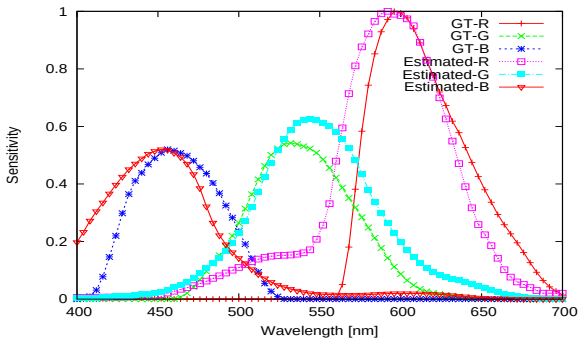

(e) Estimated spectral sensitivity from (c).

Figure 3.14: Manually processed image and estimated spectral sensitivities for Canon EOS Rebel XTi: (a) is the original image, (b) is manually processed image by changing color balance, (c) is manually processed image by increasing the pixel value of green channel, (d) shows estimated spectral sensitivity from (b), (e) shows estimated spectral sensitivity from (c).

3.6 Discussion

Many images, particularly those available on the Internet, have been processed further by image processing software, such as the Adobe Photoshop. To clarify the limitation of the method, we created such modified images: the color balance is changed for the first one (multiplying each color channel by a constant), the hue is manually adjusted for the second one (increasing the pixel values of the green channel to make it greenish), and then estimated the spectral sensitivities from them. The result is shown in Fig. 3.14. Fig. 3.14 (a) shows the original image, (b) shows the manually color balanced image, (c) shows the manually hue-adjusted image, (d) and (e) show the estimated results. Estimated spectral sensitivity from image (b) is close to the ground-truth. However, estimated spectral sensitivity from image (c) has large errors compared to the ground-truth, because the turbidity is deviated by the hue modification. Some operations performed on the input image by the Photoshop do not conflict with the spectral sensitivity estimation. How to automatically filter out the contaminated images is our future work.

3.7 Summary

In this chapter, we have proposed a novel method to estimate spectral sensitivities and white balance of digital cameras solely from images. This problem is important, since different cameras and settings can give different color values, although the incoming lights are identical. This would significantly benefit physics-based computer vision or computer vision in general, particularly for future research where the images on the Internet become valuable.

To conclude, our contributions in this paper are (1) the novel method that uses solely images for spectral sensitivity and white balance estimation, (2) a database of spectral sensitivities that is publicly available, (3) an improved atmospheric turbidity estimation that handles a wide variety of cameras, and (4) spectral sensitivity-based color correction between different cameras.

Chapter 4

Virtual Object Rendering with Aerial Perspective Effect

The virtual object is realistically inserted into a real scene by using the estimated atmospheric turbidity. Specifically, the aerial perspective is modeled by the turbidity. Virtual object rendering has been widely used in many fields, such as the academy, the architecture, the entertainment and the heritage preservation. Aerial perspective plays an important role for making the object appear realistic especially when the object is far away from the camera. This chapter describes the virtual object rendering technique with taking the aerial perspective effect into account. The atmospheric turbidity is first estimated by matching the brightness distributions, then the spectral radiance of the sun and skylight is calculated from the estimated turbidity, the aerial perspective effect is calculated as the summation of in-scattered and out-scattered spectral radiance along the camera view direction. Experimental results show the accuracy of this technique.

4.1 Introduction

Recently, the virtual object rendering which inserts the computer graphics models into a real scene has become popular (Azuma, 1997; Azuma et al, 2001). The virtual object rendering can be used in many fields, such as the academy, the architecture, the medical industry and the entertainment. It also has been widely used for representing lost cultural heritage objects, for instance, the virtual Asukakyo project which restores the ancient capital of Asukakyo to its original state (Ikeuchi, 2007; Kakuta et al, 2004).

These lost objects are difficult to rebuild due to the problem of cost and archaeological concerns. Instead, rather than rebuilding the cultural heritage objects, it would be preferable to exhibit computer graphics models of them to visitors, hereby increasing the visitor's understanding of the significance of the historical sites.

The virtual object rendering needs the geometry and illumination condition for seamlessly insert the virtual object into a real scene. The geometry information is obtained from the computer graphics models and the illumination can be either captured by using omni-directional camera (Okura et al, 2008) or estimated from the cast shadows (Sato et al, 2003b). The geometry information and the illumination condition guarantee the rendered image appear real, for instance, make the cast shadow of the virtual object match that of other objects in the scene.

Besides the geometry information and the illumination condition, the aerial perspective effect also makes the rendered object appear realistic, especially when the object is far away from the camera. The aerial perspective effect is caused by the scattering of particles suspended in the atmosphere. It is proved that the efficient and accurate way to calculate the aerial perspective effect is from the atmospheric turbidity (Preetham et al, 1999). Therefore, the problem for realistically rendering the appearance of distant object is how to estimate the turbidity value.

In this chapter, the turbidity is estimated by matching the brightness distributions between the actual image and the sky model. After acquiring the turbidity, the spectral radiance of the sun and the sky is calculated. The aerial perspective is caused by the scattering of particles, therefore, it is calculated as the summation of in-scattered and out-scattered light along the view direction.

4.1.1 Related Work

The illumination condition is very important for seamlessly integrating the computer graphics models with the real scene. Much effort has been made for recovering the illumination environment. Debevec (1998) uses the calibrated sphere to measure the global illumination for inserting new objects into real scene. Sato et al (1999a) propose to use the fish-eye lens for capturing the radiance distribution of a real scene automatically and superimpose virtual object. Lalonde et al (2009) describe a novel method for estimating the outdoor illumination from multiple cues of the input image: the sky pixels, the shading information and the casted shadows. They report that no single cue could provide robust estimation while the combination of these cues produce

reliable results.

Despite of the illumination estimation, many methods relate to calculating the aerial perspective effect have been proposed, because the aerial perspective effect makes the rendered object appear realistic, especially when it is far away from the camera. Klassen (1987) presents a lighting model with the scattering effect which is caused by suspended particles, and use the lighting model for rendering fog under general lighting conditions. Kaneda et al (1991) use the aerial perspective for displaying the appearance of a building under various weather conditions. The aerial perspective is explicitly calculated from Klassen's atmosphere scattering model. Ward (1994) integrates the aerial perspective effect into the Radiance rendering software. In his method, the aerial perspective is calculated by assuming the ambient illumination is constant and independent of the varies of viewing direction. This approximation is efficient, but it can not handle the changes in view directions and sun positions. Ebert et al (1998) use a similar approach as in this chapter, the aerial perspective is calculated by using the Rayleigh scattering. The object color is calculated as the linear combination of surface color and weighted sky color. The weight factor varies as the object moves further away from the camera.

4.2 Aerial Perspective Calculation

Aerial perspective describes the appearance of object due to light scattering when the object is far away from the camera. The aerial perspective plays an important role for making the rendered image appear realistic. The importance of this effect is emphasized by the psychologists and artists. Psychologists prove that the aerial perspective effect is the only absolute depth cue available when the object is distant (Goldstein, 1980). Painters use the aerial perspective to create the illusion of depth for distant objects in their paintings.

Fig. 4.1 shows the aerial perspective effect due to the light scattering. Fig. 4.2 roughly shows how the aerial perspective effect changes the color of object surface: Fig. 4.2 (a) is the rendered image of outdoor scene without the aerial perspective effect, while Fig. 4.2 (b) shows the rendered image with aerial perspective effect. The color of the ground slightly changes due to the light scattering in Fig. 4.2 (b).

Aerial perspective exists when the object is distant from the camera, it is caused by the light scattering along the view direction. The aerial perspective is calculated from

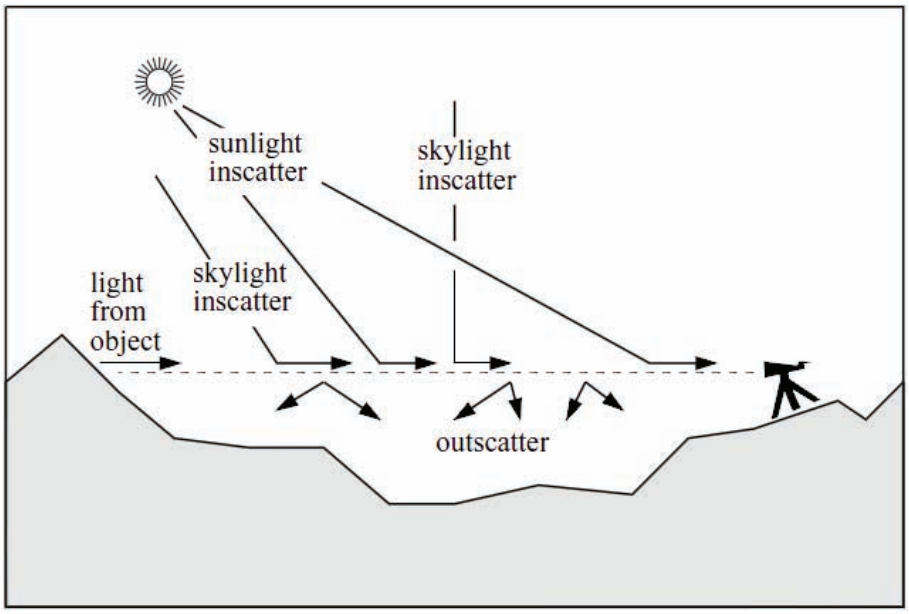

Figure 4.1: The object color changes due to the light scattering when the object is distant to the camera. In scattering effect adds light along the view direction, and out-scattering effect removes light along the view direction (Preetham et al, 1999).

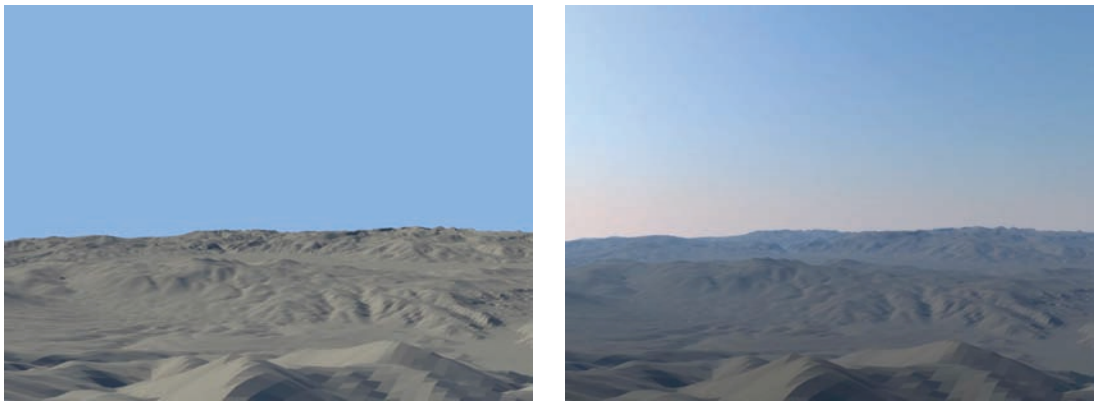

(a) Image without aerial perspective. (b) Image with aerial perspective.

Figure 4.2: How the aerial perspective change the object color: (a) shows the rendered image of outdoor scene without aerial perspective, (b) shows the rendered image with aerial perspective (Preetham et al, 1999).

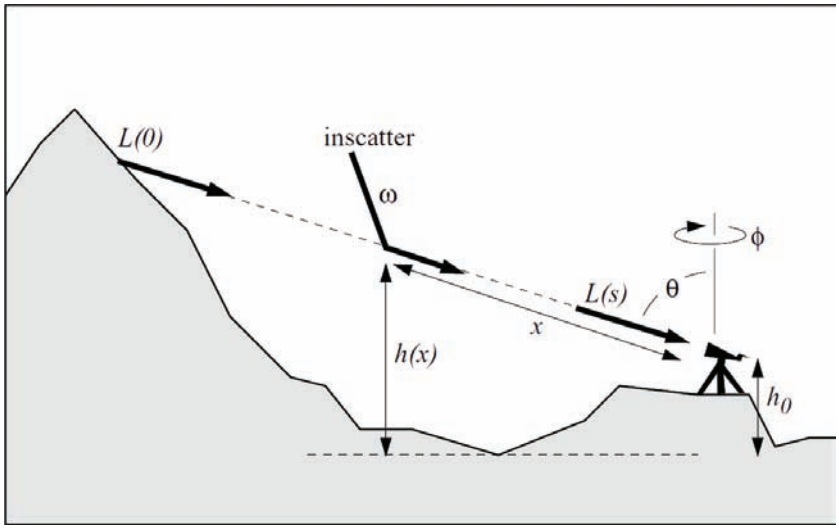

Figure 4.3: The parameters used for calculating the aerial perspective effect: $L(0)$ is the reflected light at the object surface, $L(s)$ is the reflected light after scattering, θ is the elevation angle of the camera, ϕ is the azimuth angle of the camera, h_0 is the height of the camera, $h(x)$ is the height of point x, ω is the solid angle used for calculating the in-scattering light at point x (Preetham et al, 1999).

the in-scattering light and out-scattering light (Preetham et al, 1999):

$$L(s) = L_0\tau + L_{in}, \tag{4.1}$$

where L_0 is the reflected spectral radiance at the object surface, L_{in} is the in-scattering light, τ is the extinction factor along the distance s from the object to the camera, the multiplication $L_0\tau$ describes the out-scattering light. The parameters used in this Equation is shown in Fig. 4.3.

The light scattering occurs because of the existence of various particles in the atmosphere. According to different particles, different scattering equations are applied. Specifically, the particles in the atmosphere could be roughly divided into two kind: the molecules which has the diameter smaller than the wavelength of light and the haze which has the diameter bigger than the wavelength of light. Rayleigh scattering is used for describing the molecule scattering and Mie scattering is used for haze scattering. For both particles, the density varies according to the height, hence the scattering coefficients also vary according to the height. In order to make the computation tractable, an assumption is introduced here: the particle density varies exponentially

to the height. The scattering coefficient at the height h is described as:

$$\begin{aligned}\beta(h) &= \beta_0 e^{-\alpha h} \\ &= \beta_0 e^{-\alpha(h_0 + x\cos\theta)} \\ &= \beta_0 u(x), \end{aligned} \tag{4.2}$$

where, β_0 is the scattering coefficient at earth's surface, α is the exponential decay constant, $u(x)$ is the ratio of scattering coefficient at height h to the earth's surface. The other scattering term is used for describing the in-scattering effect. The fraction of light scattered into the viewing direction (θ, ϕ) from a solid angle ω is described as:

$$\beta(\omega, \theta, \phi, h(x)) = \beta_0(\omega, \theta, \phi)u(x). \tag{4.3}$$

4.2.1 Out-scattering Coefficient

The out-scattering coefficient is calculated as $L_0\tau$, L_0 is the reflected light at object surface and τ is the extinction factor which describes the attenuation along the view direction. By using the assumption that the attenuation decreases exponentially to the height, the extinction factor over a distance s is given by:

$$\tau = e^{-\int_0^s \beta dx}. \tag{4.4}$$

By substituting the β with Eq. 4.2, we get:

$$\begin{aligned}\tau &= e^{-\int_0^s \beta_0 u(x) dx} \\ &= e^{-\beta_0 e^{-\alpha h_0} \frac{(1 - e^{-\alpha s\cos\theta})}{\alpha\cos\theta}}. \end{aligned} \tag{4.5}$$

The atmosphere contains two different particles, different particle has different scattering coefficient β_0 and decay constant α. The scattering effect of one particle is independent of the other particle, therefore, the total extinction factor of haze and molecule is calculated as the multiplication:

$$\begin{aligned}\tau_{total} &= \tau_{haze} \cdot \tau_{molecule} \\ &= e^{-\beta_{0,h} e^{-\alpha_h h_0} \frac{(1 - e^{-\alpha_h s\cos\theta})}{\alpha_h\cos\theta}} \cdot e^{-\beta_{0,m} e^{-\alpha_m h_0} \frac{(1 - e^{-\alpha_m s\cos\theta})}{\alpha_m\cos\theta}}. \end{aligned} \tag{4.6}$$

The scattering coefficients at the earth's surface for haze ($\beta_{0,h}$) and molecules ($\beta_{0,m}$) are described as:

$$\beta_{0,h} = 0.434\mathbf{c}(\mathbf{T})\pi(\frac{2\pi}{\lambda})^{v-2}k, \tag{4.7}$$

$$\beta_{0,m} = \frac{8\pi^3(n^2 - 1)^2}{3N\lambda^4}(\frac{6 + 3p_n}{6 - 7p_n}), \tag{4.8}$$

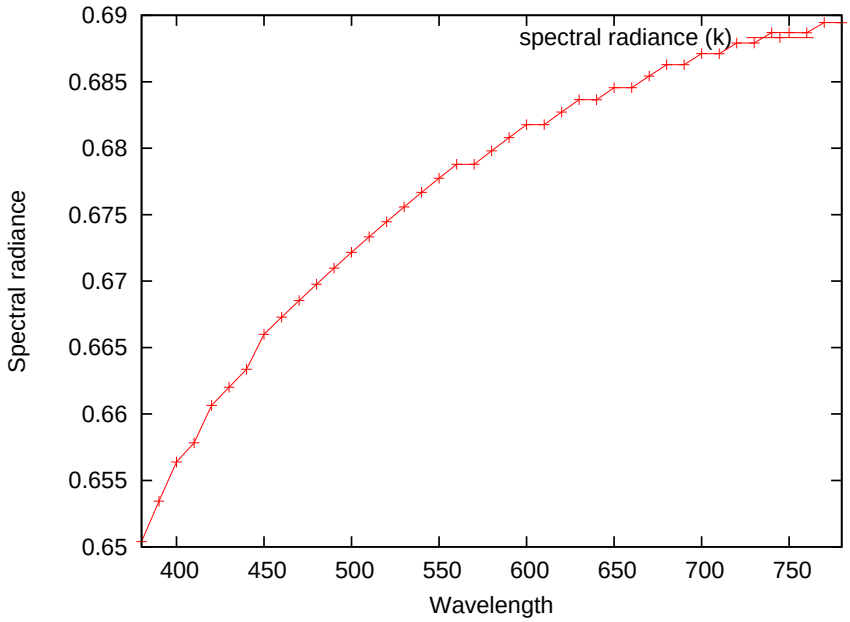

Figure 4.4: Spectral radiance(k) used for calculating the scattering coefficient of haze($\beta_{0,h}$) at the earth's surface.

where c is the concentration factor which is determined by turbidity T as $(0.6544T - 0.6510) * 10^{-16}$ and v is Junge's exponent with a value of 4 for the sky model, the data of spectra k is plotted in Fig. 4.4, n is the refractive index of air with the value of 1.0003 for the visible spectra, N is the number of molecules per unit volume with the value of $2.545 * 10^{25}$, p_n is the depolarization factor with the standard value of 0.035 for air. The value of exponential decay constants for haze (α_h) and molecules (α_m) are 0.8333 and 0.1136, respectively.

4.2.2 In-scattering Coefficient

The sun and sky light scatter into every point along the view direction. Let us denote the spectral radiance of the sun and sky in the direction ω as $L(\omega)$ and the light scattered into the viewing direction (θ, ϕ) at point x as $E(\theta, \phi, x)$. The in-scatter light at point x is

Table 4.1: The Mie scattering term $\eta(\theta)$ used for calculating the angular scattering coefficient of haze.

$\theta \setminus \lambda$	400	450	550	650	850
1	4.192	4.193	4.177	4.147	4.072
4	3.311	3.319	3.329	3.335	3.339
7	2.860	2.868	2.878	2.883	2.888
10	2.518	2.527	2.536	2.542	2.547
30	1.122	1.129	1.138	1.142	1.147
60	3.324	3.373	0.3433	0.3467	0.3502
80	0.1644	0.1682	0.173	0.1757	0.1785
90	0.1239	0.1275	0.1320	0.1346	0.1373
110	0.08734	0.09111	0.09591	0.09871	0.10167
120	0.08242	0.08652	0.09179	0.09488	0.09816
130	0.08313	0.08767	0.09352	0.09697	0.10065
150	0.09701	0.1024	0.1095	0.1137	0.1182
180	0.1307	0.1368	0.1447	0.1495	0.1566

described as the multiplication of $L(\omega)$ and angular scattering coefficient(Eq. 4.3):

$$\begin{aligned} E(\theta,\phi,x) &= \int L(\omega)\beta(\omega,\theta,\phi,h)d\omega \\ &= \int L(\omega)\beta_0(\omega,\theta,\phi)u(x)d\omega \\ &= E^0(\theta,\phi)u(x), \end{aligned} \tag{4.9}$$

where $E^0(\theta,\phi)$ is the light scattered into the viewing direction (θ,ϕ) at earth's ground and is expressed as:

$$E^0(\theta,\phi) = \int L(\omega)\beta_0(\omega,\theta,\phi)d\omega, \tag{4.10}$$

$\beta_0(\omega,\theta,\phi)$ is the angular scattering coefficients for haze and molecules at the earth's surface and is calculated as:

$$\beta_h(\theta) = 0.434\mathbf{c}(\mathbf{T})(\frac{2\pi}{\lambda})^{v-2}\frac{1}{2}\eta(\theta), \tag{4.11}$$

$$\beta_m(\theta) = \frac{\pi^2(n^2-1)^2}{2N\lambda^4}(\frac{6+3p_n}{6-7p_n})(1+cos^2\theta), \tag{4.12}$$

where the parameters n, N, p_n, c and v have the same meaning as used in Eq.(4.8), the values of the scattering term $\eta(\theta)$ for Mie scattering is shown in Table. 4.1.

Let us define the extinction factor τ (Eq. 4.6) from the object surface to the point x along the viewing direction as $\tau(0 \dots x)$, the total light scattering into the view direction for one particle is described as:

$$\begin{aligned} L_{in} &= \int_0^s E(\theta, \phi, x)\tau(0 \dots x)dx \\ &= \int_0^s E^0(\theta, \phi)u(x)\tau(0 \dots x)dx. \end{aligned} \tag{4.13}$$

The atmosphere contains two kinds of particles: the haze and the molecules. Therefore, the total light scattering into the view direction is calculated as the summation of the in-scattering of the two particles:

$$\begin{aligned} L_{in} &= \int_0^s E_h^0(\theta, \phi)u_h(x)\tau(0 \dots x)dx + \int_0^s E_m^0(\theta, \phi)u_m(x)\tau(0 \dots x)dx \\ &= E_h^0(\theta, \phi)H_h + E_m^0(\theta, \phi)H_m, \end{aligned} \tag{4.14}$$

where H for two different particles is calculated as:

$$H_h = \int_0^s u_h(x)\tau(0 \dots x)dx, \tag{4.15}$$

$$H_m = \int_0^s u_m(x)\tau(0 \dots x)dx. \tag{4.16}$$

Eq. (4.14) describes how to estimate the in-scattering light with a distance s along the viewing direction. E_h^0 and E_m^0 are calculated from the Eq. (4.10), H_h and H_m are calculated analogously. The equations for computing H_h is shown as follows. The K and M are defined as:

$$K = -\frac{\beta_0}{\alpha cos\theta}, \tag{4.17}$$

$$M = e^{-\alpha h_0}. \tag{4.18}$$

By substituting K and M in Eq. (4.6), we get:

$$\tau = e^{-K_h(M_h - u_h(s))}e^{-K_m(M_m - u_m(s))}. \tag{4.19}$$

Then Eq. (4.15) is rewritten as:

$$H_h = \int_0^s u_h(x)e^{-K_h(M_h - u_h(x))}e^{-K_m(M_m - u_m(x))}dx. \tag{4.20}$$

When the distance s is considered small or the viewing direction is close to the horizon, then $|scos\theta \ll 1|$. The extinction coefficient is calculated as:

$$\begin{aligned} e^{-K(M-u(x))} &= e^{-\beta M \frac{1-e^{-\alpha x cos\theta}}{\alpha cos\theta}} \\ &\approx e^{-\beta M x}. \end{aligned} \tag{4.21}$$

Thus

$$\begin{aligned} H_h &= \int_0^s u_h(x) e^{-K_h(M_h-u_h(x))} e^{-K_m(M_m-u_m(x))} dx \\ &= \int_0^s e^{-M_h} e^{-\alpha_h x cos\theta} e^{-\beta_h M_h x} e^{-\beta_m M_m x} dx \\ &= e^{-M_h} \frac{1-e^{-(\alpha_h cos\theta+\beta_h M_h+\beta_m M_m)s}}{\alpha_h cos\theta+\beta_h M_h+\beta_m M_m}. \end{aligned} \tag{4.22}$$

However, when the conditional term $|scos\theta \ll 1|$ is not satisfied, H_h can not be calculated by using the Eq. (4.22). Under this situation, H_h could be only calculated from the integrals. This is too impractical to be used for efficiently rendering the object appearance. In order to solve this problem, the approximations for the Eq. (4.20) are introduced. The function v is defined as:

$$v = u_h(x) = e^{-\alpha_h(h_0+xcos\theta)}. \tag{4.23}$$

Therefore, we get

$$dv = -\alpha_h cos\theta u_h(x) dx. \tag{4.24}$$

Then the Eq. (4.20) is written as:

$$H_h = -\frac{1}{\alpha_h cos\theta} \int_{u_h(0)}^{u_h(s)} e^{-K_h(M_h-v)} e^{-K_m(M_m-u_m(x))} dv. \tag{4.25}$$

The second term of the integral $f(x) = e^{-K_m(M_m-u_m(x))}$ in Eq. (4.25) is substituted by a Hermite cubic polynomial $g(v) = Av^3 + Bv^2 + Cv + D$. The coefficients A, B, C and D for the cubic equivalent are determined such that $g(v)$ interpolates the position and slope of the endpoints of $f(x)$. By using the approximations, the integral is described as:

$$\begin{aligned} H_h &= -\frac{1}{\alpha_h cos\theta} \int_{u_h(0)}^{u_h(s)} e^{-K_h(M_h-v)} g(v) dv \\ &= -\frac{1}{\alpha_h cos\theta} [e^{-K_h(M_h-v)} (\frac{g(v)}{K_h} - \frac{g'(v)}{K_h^2} + \frac{g''(v)}{K_h^3} - \frac{g'''(v)}{K_h^4})]_{M_h}^{u_h(s)} \\ &= -\frac{1}{\alpha_h cos\theta} ((e^{-K_h(M_h-u_h(s))})(\frac{g(u_h(s))}{K_h} - \frac{g'(u_h(s))}{K_h^2} + \frac{g''(u_h(s))}{K_h^3} - \frac{g'''(u_h(s))}{K_h^4}) - \\ &\quad (\frac{g(M_h)}{K_h} - \frac{g'(M_h)}{K_h^2} + \frac{g''(M_h)}{K_h^3} - \frac{g'''(M_h)}{K_h^4})). \end{aligned} \tag{4.26}$$

The parameters A, B, C and D in the function $g(v) = Av^3 + Bv^2 + Cv + D$ to approximate $f(x) = e^{-K_m(M_m - u_m(x))}$ are determined by the solution of the following linear equations:

$$\begin{bmatrix} M_h^3 & M_h^2 & M_h & 1 \\ u_h(s)^3 & u_h(s)^2 & u_h(s) & 1 \\ 3M_h^2 & 2M_h & 1 & 0 \\ 3u_h(s)^2 & 2u_h(s) & 1 & 0 \end{bmatrix} \begin{bmatrix} A \\ B \\ C \\ D \end{bmatrix} = \begin{bmatrix} 1 \\ f(s) \\ f'(0) \\ f'(s) \end{bmatrix}. \tag{4.27}$$

4.3 Virtual Object Rendering

The rendering process requires the following inputs for realistic object appearance: (1) the object shape, (2) the object surface reflectance, (3) the illumination and (4) the aerial perspective calculation.

The shape information is obtained from the computer graphics models, because the capital does not exist now. Fig. 4.5 shows the view of the whole capital. In the created models, this ancient capital consists of five different parts: the Ishigami, the Asukadera, the Asukaike, the Kiyomiharanomiya and the Ebinoko. Fig. 4.6 and 4.7 shows the parts of the Kiyomiharanomiya and the Ebinoko, respectively. One palace of the Kiyomiharanomiya is shown in Fig. 4.8. The reflectance of the created models are manually set.

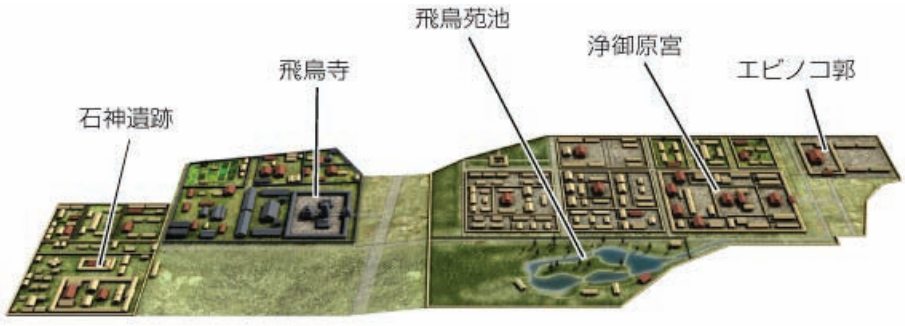

Figure 4.5: The ancient capital of Asukakyo created by computer graphics models. The whole capital consists of five different parts: the Ishigami, the Asukadera, the Asukaike, the Kiyomiharanomiya and the Ebinoko.

The illumination environment (the spectral radiance of the sun and the sky) is estimated from the atmospheric turbidity. Specifically, we first capture the omni-directional image with the spherical camera Ladybug2, the turbidity is estimated by

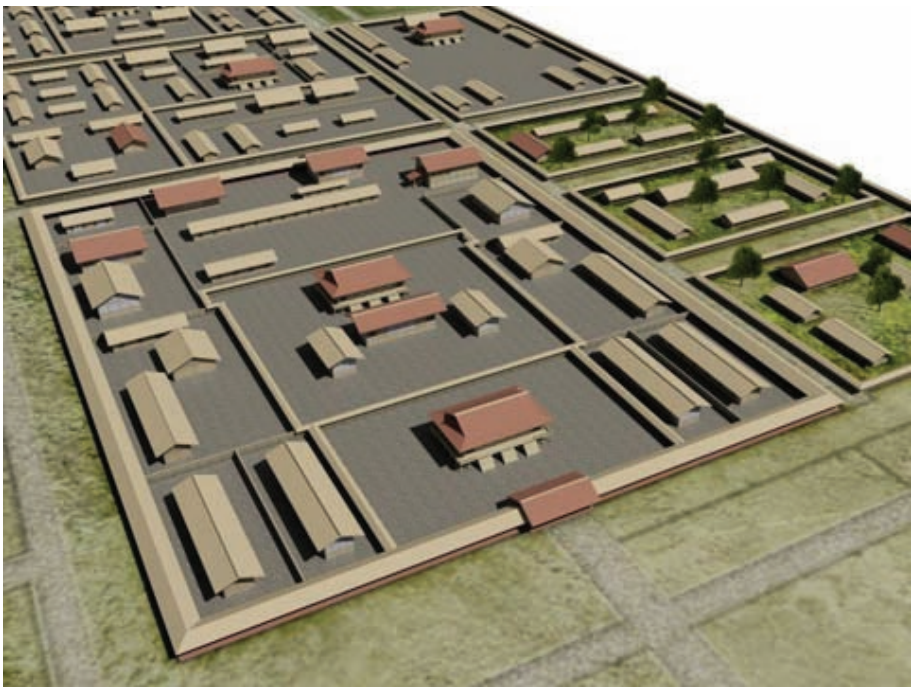

Figure 4.6: One part of the ancient capital: the Kiyomiharanomiya.

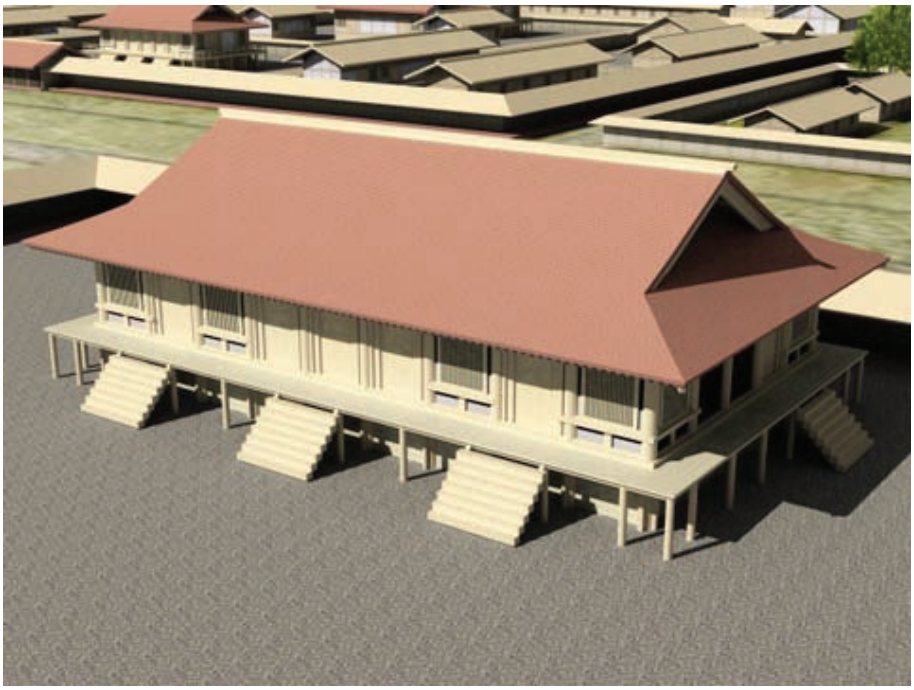

Figure 4.7: One part of the ancient capital: the Ebinoko.

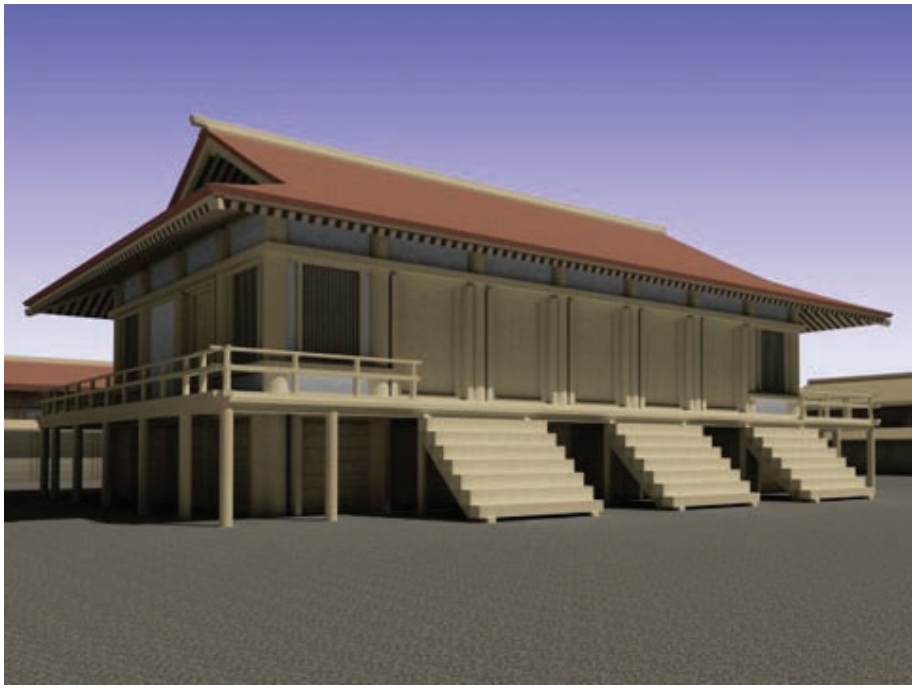

Figure 4.8: One palace of the Kiyomiharanomiya.

matching the brightness distribution of the captured image and the sky model, then the estimated turbidity is used for calculating the spectral radiance of the sun and the chromaticity values xy of the sky pixels, the spectral radiance of the sky light is calculated from the xy values by using three basis functions for outdoor illumination.

After acquiring the shape information and illumination condition, the object appearance is rendered. When the object is illuminated by a light source, the reflected light will go through the camera lens and recorded by the charged couple device (CCD). Then the recored value by the camera is described as:

$$I_c = \int_{\Omega} L(\lambda) q_c(\lambda) d\lambda, \tag{4.28}$$

where I_c is the recorded RGB values, c stands for R, G and B color channels, Ω is the visible wavelength with the value from 380nm to 780nm, $L(\lambda)$ is the reflected spectral radiance at the object surface, $q_c(\lambda)$ is the spectral sensitivity. The aerial perspective effect of distant object is described as:

$$L_s = L_0 \tau + L_{in}. \tag{4.29}$$

By substituting Eq. (4.29) into Eq. (4.28), we get:

$$\begin{aligned} I_c &= \int_\Omega (L_0\tau + L_{in}) q_c(\lambda) d\lambda \\ &= \int_\Omega L_0 \tau q_c(\lambda) d\lambda + \int_\Omega L_{in} q_c(\lambda) d\lambda. \end{aligned} \tag{4.30}$$

In Eq. (4.30), the first term describes the out-scattering effect and the second term describes the in-scattering effect. Note that L_0 is the reflected spectral radiance at the object's surface and is calculated as:

$$L_0 = L_{light} \cdot R, \tag{4.31}$$

where L_{light} is the spectral radiance of illumination and R is the spectral reflectance of object. The models are created by computer graphics, hence, we do not have the spectral reflectance. This makes the problem intractable. However, if assuming that the camera spectral sensitivity can be approximated by a Dirac's delta function (narrow-band assumption), the wavelength λ can be considered as a constant. The first term becomes:

$$\begin{aligned} \int_\Omega L_0 \tau q_c(\lambda) d\lambda &\simeq \int_\Omega L_0 q_c(\lambda) d\lambda \cdot \int_\Omega \tau q_c(\lambda) d\lambda \\ &\simeq I' \cdot \Gamma, \end{aligned} \tag{4.32}$$

where I' is the object appearance when the camera is close (without taking the aerial perspective into account) and calculated as $\int_\Omega L_0 q_c(\lambda) d\lambda$, Γ is calculated as $\int_\Omega \tau q_c(\lambda) d\lambda$. Thus, Eq. (4.30) is rewritten as:

$$I_c = I' \cdot \Gamma + \int_\Omega L_{in} q_c(\lambda) d\lambda, \tag{4.33}$$

where I' can be calculated from the shape information and reflectance with known illumination, the equations for calculating τ and L_{in} are introduced in the previous section.

4.4 Experiment

The ancient capital Asukakyo lies in the Nara prefecture, there is a small hill called as the Amakashioka near the ruin of Asukakyo. The image is taken on the top of this hill. Fig. 4.9 shows the location of the ancient capital and the Amakashioka hill. The

Figure 4.9: The location of the ancient capital Asukakyo and the Amakashioka where we take the image.

Figure 4.10: Captured omni-directional image on the top of Amakashioka.

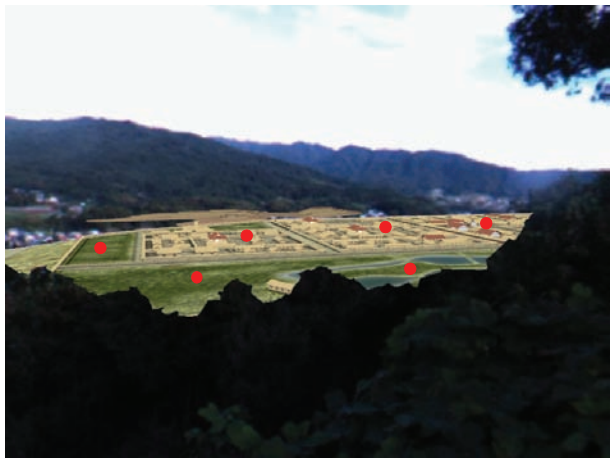

(a) Without aerial perspective.

(b) Wavelength based aerial perspective.

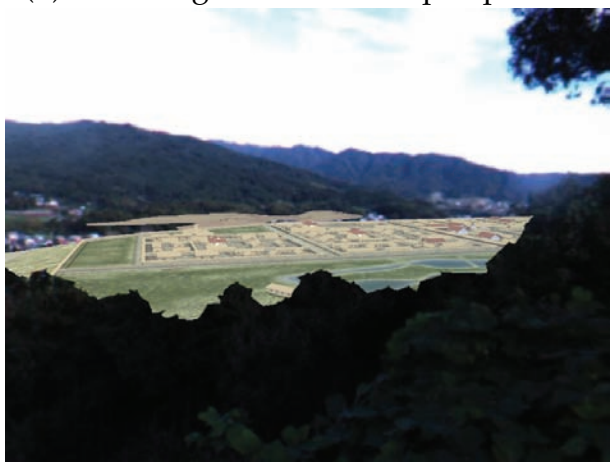

(c) *RGB* based aerial perspective.

Figure 4.11: Rendered images with and without aerial perspective, red points in (a) show the sample points for the evaluation.

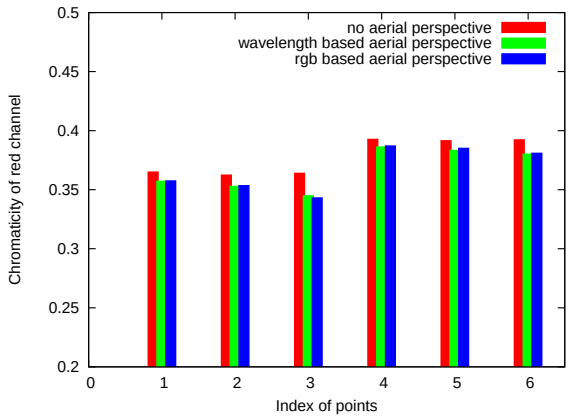

(a) Red channel.

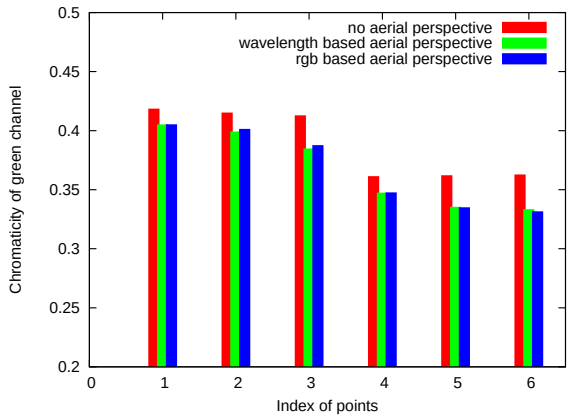

(b) Green channel.

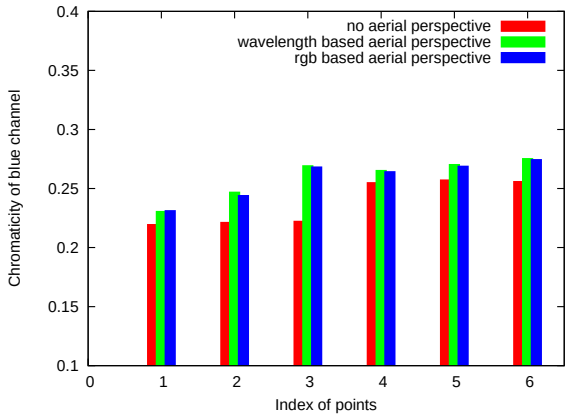

(c) Blue channel.

Figure 4.12: Numerical evaluation of chromaticity values of rendered images with and without aerial perspective.

red line in Fig. 4.9 shows the camera view direction. The straight line distance from the Amakashioka hill to the Asukakyo is about 900 meters according to the Google map.

The captured omni-directional image is shown in Fig. 4.10, the red rectangle shows the area where the Asukakyo lies. The sun direction is extracted from the longitude, the latitude and the time when the image is captured.

The experiment results are shown in Fig. 4.11. Fig. 4.11 (a) shows the rendered image without taking the aerial perspective into account, (b) shows the rendered image with wavelength based aerial perspective calculation and (c) shows the rendered image with *RGB* color channel based aerial perspective calculation. Compared to the wavelength based aerial perspective, the *RGB* color channel based aerial perspective calculates the in-scattering and out-scattering effect by taking integral over the *RGB* channels instead

of the wavelengths. We implemented the *RGB* color channel based aerial perspective for efficiency. Note those two hills behind the Asukakyo, they appear hazy due to the aerial perspective. The aerial perspective effect is calculated in (b) and (c), therefore they also appear hazy. It becomes obvious when comparing to the rendered image without aerial perspective.

The numerical evaluation is shown in Fig. 4.12. We took six sample points as shown in Fig. 4.11 (a). The chromaticity values of these six sample points from rendered images with and without aerial perspective are compared. The chromaticity values for *RGB* color channels are calculated as $I_c/(I_r + I_g + I_b)$. In Fig. 4.12, the red column represents the chromaticity from rendered image without aerial perspective, the green column represents the chromaticity from rendered image with wavelength-based aerial perspective and the blue column represents the chromaticity from rendered image with *RGB*-based aerial perspective. The chromaticity values from rendered images with aerial perspective are different from that of rendered image without aerial perspective. The chromaticity values from rendered image with *RGB*-based aerial perspective are close to that from rendered image with wavelength-based aerial perspective.

4.5 Summary

This chapter introduces the virtual object rendering with aerial perspective effect. The aerial perspective models the slight color change of object when it is distant from the camera, and make the rendered image appear realistic. We first estimate the turbidity from input image and calculate the xy chromaticity values of the sky, the spectral radiance of the sun is calculated from the turbidity and the spectral radiance of the sky is calculated from the xy chromaticity values by using the basis functions of outdoor illumination, the aerial perspective effect is calculated from the in-scattered and out-scattered spectral radiance of sun and sky along the camera viewing direction. Experiment results show the accuracy achieved by the turbidity-based aerial perspective calculation.

Chapter 5

Reflectance Estimation from a Single Perspective Image

The surface reflectance is calculated from the illumination, which is recovered from the estimated turbidity value. Computer vision and graphics techniques need the accurate reflectance properties to create a realistic three-dimensional model of a real world object. This chapter proposes a practical method to estimate the surface reflectance parameters of outdoor diffuse object from a single perspective image. The basic idea is to recover the whole illumination condition from the sky portion captured in the perspective image. The atmospheric turbidity is estimated from the sky portion, the spectral radiance of the sun and sky light is calculated from the estimated turbidity. The inter-reflection exists for concave objects. The inter-reflection problem is solved by assuming the object surface consists of hundreds of small facets. The inter-reflection effect on one facet is calculated as the sum of incoming light energy from all the other facets. Experimental results show the accuracy achieved by the proposed method.

5.1 Introduction

To create a realistic model of a real world object by computer vision and graphics techniques has attracted interest from a wide range of research fields and industries in recent years. Shape and reflectance properties of the object are necessary to simulate the accurate appearance of an object. As a result of significant advancement of range sensors and data processing algorithms, shape of an object becomes acquirable without

much difficulties (Ikeuchi and Miyazaki, 2008; Ikeuchi et al, 2007). However, obtaining the reflectance properties of the object remains a challenge, especially for outdoor objects, because it is hard to precisely model the outdoor illumination.

Much effort has been made for acquiring the outdoor illumination condition (Debevec et al, 2004; Okura et al, 2008). These methods need expensive equipments or massive calibrations. They are not applicable when only a single perspective image is available. Lalonde et al (2009) propose to estimate the outdoor illumination from single perspective image. They use multiple cues from the input image: the sky pixels, the shading information and the casted shadows. They also report that no single cue could provide robust estimation while the combination of all three cues make the estimation reliable. However, not all those three cues are always available in the input image.

Unlike the existing methods, the proposed method need a single perspective image and a sky portion captured for the reflectance estimation. The basic idea is to recover the whole illumination from the sky portion captured in the perspective image. Specifically, we first estimate the atmospheric turbidity from input image, then calculate the spectral radiance of the sun and the skylight from estimated turbidity.

This chapter proposes a practical method to estimate the reflectance parameters of an outdoor diffuse object from a single perspective image. Assuming the partial sky is captured in the input image, we first estimate the turbidity, then the spectral radiance of the sun and sky light is calculated based on the sky model (Preetham et al, 1999). The inter-reflection exists for concave objects. By dividing the object surface into hundreds of small facets, the inter-reflection effect on one facet is calculated as the sum of incoming light energy from all the other facets. Experimental results show the accuracy of the proposed method.

5.1.1 Related Work

In the late 1990s, several modeling methods with range sensors were proposed (Pulli et al, 1997; Neugebauer and Klein, 1999; Lensch et al, 2000; Wang et al, 2001; Bernardini et al, 2001). However, those methods created surface textures by simply blending images taken from multiple views. Meanwhile, physics-based reflectance estimation methods (Dana et al, 1999; Sato et al, 1997; Lin and Lee, 1999; Machida et al, 2003), image-based rendering techniques (Sato et al, 2003a; Winnemoller et al, 2005), and techniques to measure the BRDF (Bidirectional Reflectance Distribution Function) (Ward, 1992; Dana, 2001) have been studied to create a more physically correct object appearance

compared with those created in the early 1990s. Those methods have achieved highly accurate re-renderings, yet they were designed for an indoor environment where one can easily control lighting conditions.

Demands for extracting surface properties under outdoor circumstances are increasing (Ikeuchi et al, 2007), and several methods that can handle outdoor images have been proposed. A few use images of monitoring cameras placed outdoors. Weiss (2001) derived intrinsic images, which are images representing surface albedo, by assuming that the sudden change caused by reflectance remains constant in the image sequence, while that caused by illumination varies depending on the time. Therefore, by taking the median of derivative filter outputs of input images, the reflectance image can be estimated. Matsushita et al. extended the idea so that it can handle non-Lambertian surfaces, and proposed an illumination normalization scheme utilizing the illumination eigen space and a shadow interpolation method based on shadow hulls (Matsushita et al, 2004).

For directly calculating surface reflectance properties, one would need (1) the shape of a target object, (2) the actual appearance of the object, and (3) illumination environment. Shape information and actual appearance can be obtained by range and image sensors, respectively.

The illumination environment can be acquired in several ways. Yu et al. took photographs of the sun and sky to measure their radiance distribution (Yu and Malik, 1998). As they used a normal camera, they included landmarks in each photograph so that they could use them to recover the camera pose later. The position of the sun was calculated by the time and date, and the sky radiance was fitted to the CIE (International Commission on Illumination) standard model to extrapolate the missing portion of the sky. They first recovered diffuse reflectance from measured sky irradiance and from appearance, and then they acquired specular properties by fitting multiple photographs to the Lafortune model. Debevec et al. used a specific apparatus to measure the outside illumination (Debevec et al, 2004). They used a mirrored sphere to image the sky and clouds, a shiny black sphere to indicate the position of the sun, and a diffuse gray sphere to indirectly measure the intensity of the sun. They decided the reflectance parameters of the previously obtained BRDF (Bidirectional Reflectance Distribution Function) by an iterative calculation using the object's photographs from multiple views. Both of these two methods recovered the reflectance parameters of outdoor objects, however, they required multiple measurements and optical calibration.

Methods to acquire a near light source environment have also been proposed.

Sato et al (1999a) used omni-directional stereo to recover illumination with geometric information. Takai et al (2004) took an image of a pair of diffuse spheres, and used the difference between them to first estimate point light sources and then the remaining lighting environment. The two methods successfully superimposed virtual objects into room scenes as well as exterior scenes by recovering illumination of the scenes.

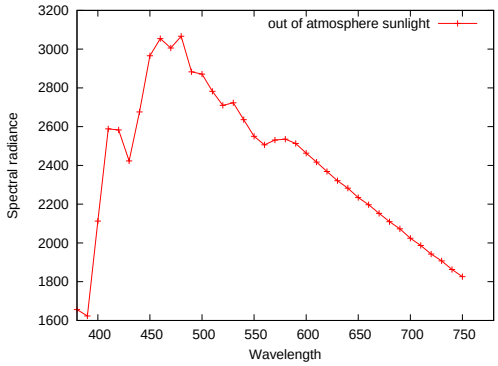

(a) Out of atmosphere sunlight.

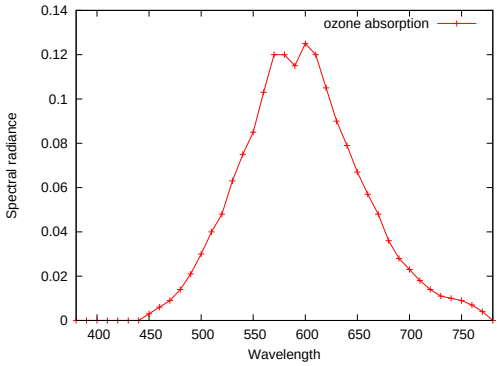

(b) Ozone absorption.

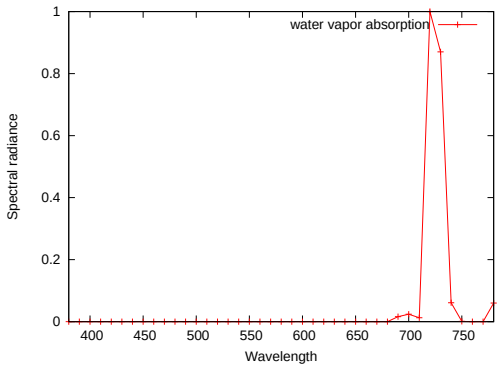

(c) Water vapor absorption.

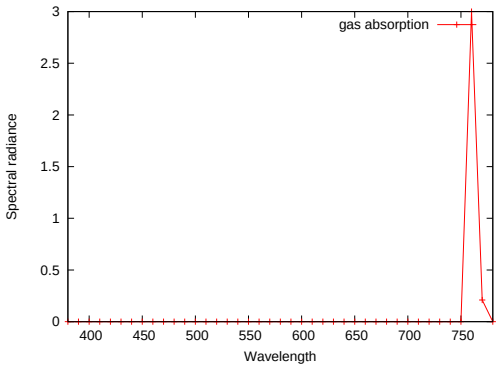

(d) Gas absorption.

Figure 5.1: Spectral radiance of the out of atmosphere sunlight and attenuation functions for ozone, water vapor and gas absorption.

5.2 Outdoor Illumination Estimation

The illumination condition is necessary to estimate the surface reflectance of outdoor object. One possible way of acquiring the outdoor illumination is to directly measure it. However, the measurement needs expensive equipments or complicated

calibrations. This makes the direct measurement of outdoor illumination inapplicable for our case, because we only have single perspective image as the input.

To solve this problem, we propose to estimate the outdoor illumination from the atmospheric turbidity. Specifically, supposing a portion of the sky is captured in the image, we first estimate the turbidity by matching the brightness distribution, then the spectral radiance of the sun and the sky is recovered by using the sky model (Preetham et al, 1999).

The outdoor illumination contains two parts: the sun and the sky. The spectral radiance of the sunlight and the sky is calculated from the turbidity and extracted sun direction. The atmospheric turbidity is estimated by matching the brightness distribution of input image to a sky model. The sun direction is calculated from the site geo-location(longitude and latitude) and the time stamp, see more details in Appendix A.

The sunlight attenuates before reaching the horizon according to various atmospheric constituents: Rayleigh scattering, aerosol, ozone absorption, gas absorption and water vapor absorption. With known spectral radiance of the out of atmosphere sunlight, the spectral radiance of the sunlight at horizon is calculated as the multiplication of the out of atmosphere radiance and the attenuations (Iqbal, 1983):

$$L(\lambda, \theta_s, \phi_s) = L_{out-of-atmosphere} \cdot A_{r,\lambda}(\theta_s) \cdot A_{a,\lambda}(T, \theta_s) \cdot A_{o,\lambda}(\theta_s, k_o) \cdot A_{g,\lambda}(\theta_s, k_g) \cdot A_{wa,\lambda}(\theta_s, k_{wa}), \tag{5.1}$$

where the coefficient A is the attenuation of different constituents, θ_s is the elevation angle of the sun, T is the turbidity value, k_o, k_g and k_{wa} are the absorption coefficients for the ozone, gas and water vapor, respectively. The attenuation coefficients are given by:

$$\begin{aligned} A_{r,\lambda} &= e^{-0.008735\lambda^{-4.08m}}, \\ A_{a,\lambda} &= e^{-\beta\lambda^{-\alpha m}}, \\ A_{o,\lambda} &= e^{-k_{o,\lambda} lm}, \\ A_{g,\lambda} &= e^{-1.41 k_{g,\lambda} m/(1+118.93 k_{g,\lambda} m)^{0.45}}, \\ A_{wa,\lambda} &= e^{-0.2385 k_{wa,\lambda} \omega m/(1+20.07 k_{wa,\lambda} \omega m)^{0.45}}, \end{aligned} \tag{5.2}$$

and the relative optical mass m is given by the following approximation:

$$m = \frac{1}{cos\theta_s + 0.15 \cdot (93.885 - \theta_s)^{-1.253}}, \tag{5.3}$$

where β is the turbidity coefficient, α is the wavelength exponent, $k_{o,\lambda}$, $K_{g,\lambda}$ and $k_{wa,\lambda}$ stand for the attenuation coefficients of the ozone absorption, the mixed gas absorption

and the water vapor absorption, l is the amount of ozone in cm at NTP, ω is the precipitable water vapor in cm and λ is the wavelength in μm. The coefficient β varies with the turbidity value T and is approximately given by $0.04608T - 0.04586$. The value of 1.3 for α, 0.35 for l and 2 for ω is used in the paper.

We have plotted the spectral radiance of out of atmosphere sunlight and the attenuation coefficients $k_{o,\lambda}$, $K_{g,\lambda}$ and $k_{wa,\lambda}$, the results are shown in Fig. 5.1.

The spectral radiance is also calculated from the atmospheric turbidity. Specifically, we first calculate the xy chromaticity from the estimated turbidity, then calculate the spectral radiance using known basis functions of daylights. See more details for calculating the spectral radiance of sky in Section 3.2.

5.3 Radiance and Irradiance Value of Object Surface

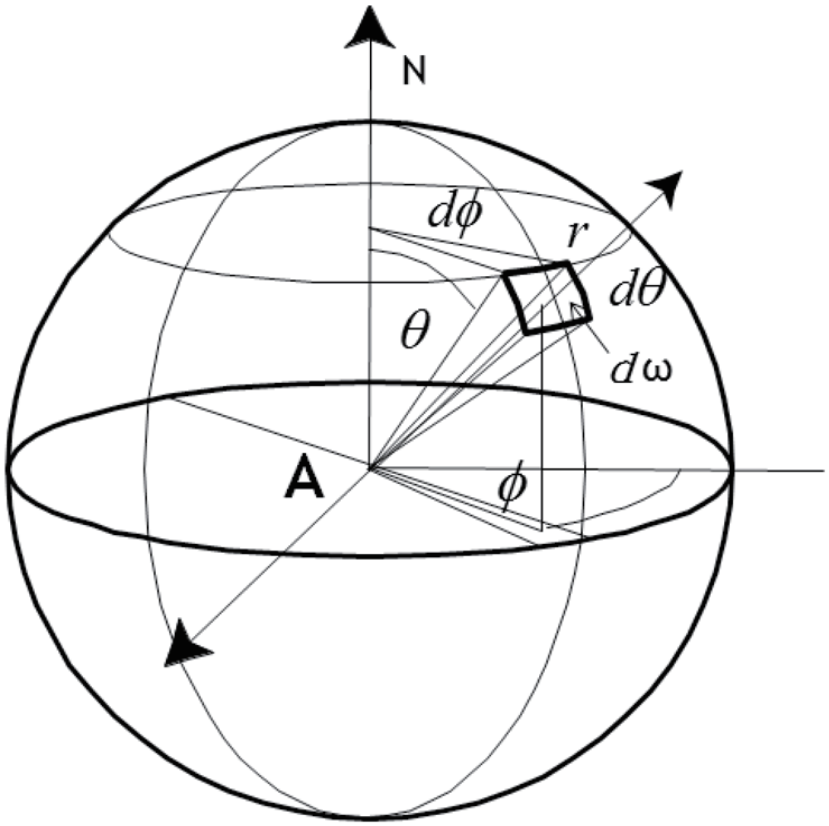

Figure 5.2: Calculation of radiance and irradiance value

In general, when assuming the object surface is Lambertian and there is no interreflection, the reflectance of an object can be derived from the bidirectional reflectance

distribution function $f = \frac{L}{E}$, where L and E are the radiance and irradiance values of object surface, respectively.

Consider a facet located at the center of the sphere (as shown in Fig. 5.2), then the solid angle $d\omega$ can be derived from the elevation θ and azimuth ϕ:

$$d\omega = \sin\theta d\theta d\phi \tag{5.4}$$

The energy received by the facet A from a particular direction, surrounded by an infinitesimal solid angle $d\omega$, is described as:

$$L(\lambda, \theta, \phi)\cos\theta \sin\theta d\theta d\phi \tag{5.5}$$

where $L(\lambda, \theta, \phi)$ is the incident radiance distribution of illumination.

The irradiance value of the facet A can be expressed as the integral of incident energy over the hemisphere whose north pole is at the surface normal direction:

$$E^A = \int_{-\pi}^{\pi}\int_{0}^{\frac{\pi}{2}} L(\lambda, \theta, \phi)\cos\theta \sin\theta d\theta d\phi \tag{5.6}$$

In this chapter, we assume that the object surface is Lambertian surface, and therefore the reflected light is isotropic. Then, the radiance value of the facet A is expressed as the multiplication of irradiance value E and reflectance S^A:

$$I^A = \int_{-\pi}^{\pi}\int_{0}^{\frac{\pi}{2}} S^A L(\lambda, \theta, \phi)\cos\theta \sin\theta d\theta d\phi \tag{5.7}$$

5.4 Reflectance Estimation with the Presence of Inter-reflection

The inter-reflection effect especially for the concave object is not negligible. In order to acquire the accurate reflectance properties for 3D object, we addressed an inter-reflection model to calculate the inter-reflection effect. An assumption is made that the object surface consists of hundreds of small facets as shown in Fig. 5.3. The inter-reflection effect on each facet is calculated as the sum of incoming light energy from all the other facets.

When the surface of a concave object is illuminated, its facets receive light from both light source and other facets, as shown in Fig. 5.4. In Fig. 5.4, the small facet x receives light from both light source and another facet $x\prime$ on the surface. Therefore, the radiance value at each surface facet has two components, one directly resulting from the light source and the second due to illumination by other facets. The latter component is also called as inter-reflection effect.

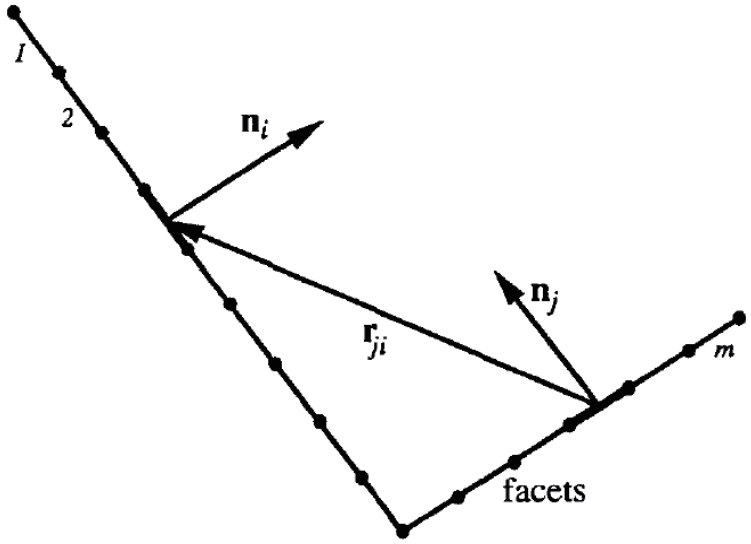

Figure 5.3: Modeling the surface as a collection of facets, each with its own radiance and reflectance values (Nayar et al, 1991).

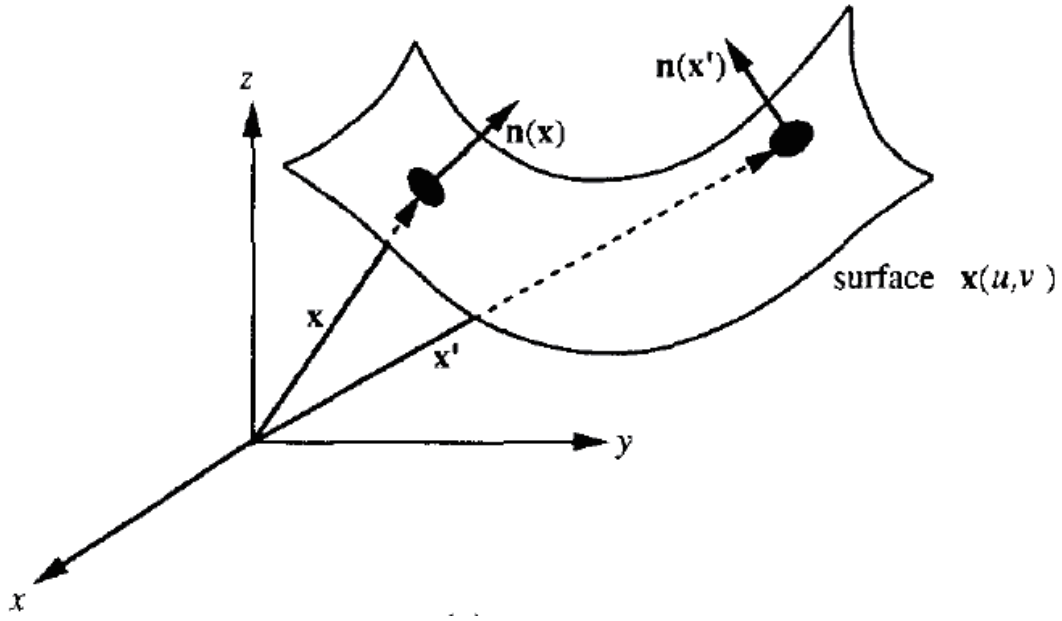

Figure 5.4: A concave surface in three-dimensional space (Nayar et al, 1991).

Radiance due to other facets The inter-reflection effect between two facets i and j is strongly affected by whether these two facets can see each other or not. Two facets i and j which are visible to each other is shown in Fig. 5.5. The visibility V between two facets i and j is determined by the following function:

$$V_{ij} = \frac{n \cdot (-r) + |n \cdot (-r)|}{2|n \cdot (-r)|} \cdot \frac{n\prime \cdot r + |n\prime \cdot r|}{2|n\prime \cdot r|} \cdot Occ \tag{5.8}$$

where n and $n\prime$ are unit surface normals of the ith and jth facets, r is the vector from jth to ith facet, and Occ is the coefficient for occlusion between these two facets. If the ith and jth facets are occluded by another facet, these two facets can not see each other.

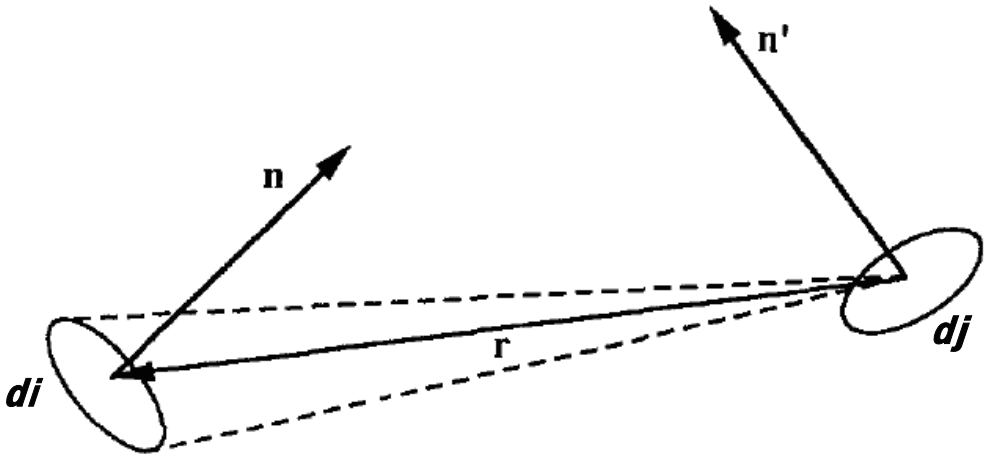

Figure 5.5: Two surface elements that are visible to one another.

The occlusion coefficient is important to calculate the visibility function. A typical situation when occlusion happens is shown in Fig. 5.6. In Fig. 5.6, the ith facet lies on the horizontal top plane, while the jth facet lies on the vertical plane. Since there is another horizontal plane between them, they cannot see each other and there is no inter-reflection effect between ith and jth facets. The occlusion coefficient is calculated as follows: for the vector between the ith and jth facets, we detect whether this vector intersects with another facet or not. If the vector intersects with at least one of the other facets, the occlusion coefficient is equal to zero. If not, there is no occlusion between the ith and jth facets and the occlusion coefficient is set to one.

The visibility function V_{ij} in Eq. (5.8) can only have two values, 1 or 0. If it is equal to 1, the ith and jth facets see each other and the inter-reflection between these two facets will be calculated. If not, no inter-reflection exists between the facets.

Let E_{ij} be the irradiance value of ith facet due to the radiance value of the jth facet L_j. E_{ij} can be derived from the definitions of radiance and irradiance and geometry shown in Fig. 5.5:

$$E_{ij} = [\frac{[n \cdot (-r)][n\prime \cdot r]V_{ij}}{[r \cdot r]^2}]L_j S_i \tag{5.9}$$

where S_i is the area of the ith facet, V_{ij} is the visibility function between the ith and jth facets, and L_j is the radiance value of the jth facet.

The radiance value L_{ij} of the ith facet can be determined from its irradiance value E_{ij} as:

$$L_{ij} = \frac{\rho_i}{\pi} E_{ij} \tag{5.10}$$

where ρ_i is the reflectance of the ith facet. The reflectance is assumed to be invariable among a facet, since a facet size is sufficiently small. The factor $\frac{\rho_i}{\pi}$ is the bi-directional reflectance distribution function for a Lambertian surface. From Eq. (5.9) and (5.10), we obtain

$$L_{ij} = \frac{\rho_i}{\pi} K_{ij} L_j \tag{5.11}$$

where

$$K_{ij} = [\frac{[n \cdot (-r)][n\prime \cdot r]V_{i_j}}{[r \cdot r]^2}]S_i \tag{5.12}$$

K_{ij} is a coefficient determined by the positions and orientations of the ith and jth facet.

From Eq. (5.11), we obtain the radiance value L_{ij} of ith facet due to the radiance value of jth facet, and as described before, this radiance value is the second component of the total radiance value for a small facet lies on the surface of a concave object.

Radiance due to a light source The radiance value of the ith facet directly due to a single point light source (excluding inter-reflection effect) can be expressed by using the irradiance value:

$$L_{si} = \frac{\rho_i}{\pi} E_{si} \tag{5.13}$$

where E_{si} is the irradiance value of the ith facet directly due to a light source. The irradiance value can be calculated from Eq. (5.6).

Total radiance The total radiance value of the ith facet L_i can be expressed as a sum of the radiance due to a light source L_{si} and all the other facets on the surface:

$$L_i = L_{si} + \frac{\rho_i}{\pi} \sum_{j=1}^{m} L_j K_{ij} \tag{5.14}$$

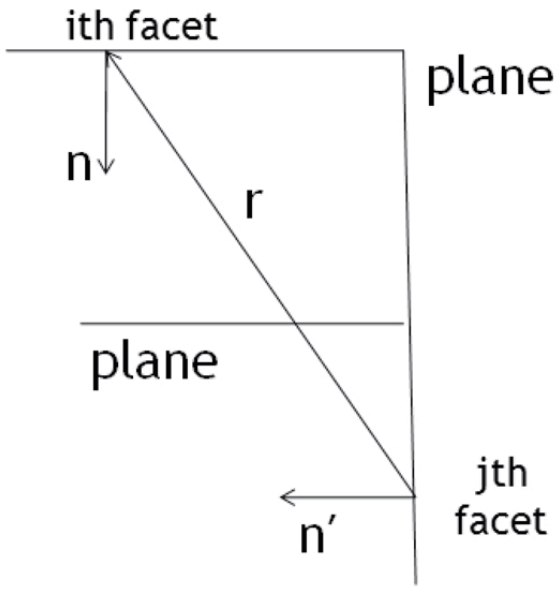

Figure 5.6: Occlusion between two facets: the ith and jth facets are occluded by the middle horizontal plane

where m is the number of facets on the object surface. When j equals to i, the K_{ij} coefficient between the ith and jth facets becomes zero, according to Eq. (5.12).

The inter-reflection equation for a concave surface can be written as follows using a vector notation. Let us define the facet radiance vector as $L = [L_1, L_2, ..., L_m]^T$, the source contribution vector as $L_s = [L_{s1}, L_{s2}, ..., L_{sm}]^T$, and the reflectance matrix P and the K_{ij} coefficient matrix K as:

$$P = \frac{1}{\pi} \begin{bmatrix} \rho_1 & 0 & \cdots & 0 \\ 0 & \rho_2 & \cdots & 0 \\ \cdots & \cdots & \cdots & \cdots \\ \cdots & \cdots & \cdots & \cdots \\ 0 & 0 & \cdots & \rho_m \end{bmatrix} \tag{5.15}$$

$$K = \begin{bmatrix} 0 & k_{12} & \cdots & \cdots & \cdots \\ k_{21} & 0 & \cdots & \cdots & \cdots \\ \cdots & \cdots & 0 & \cdots & \cdots \\ \cdots & \cdots & \cdots & 0 & \cdots \\ \cdots & \cdots & \cdots & \cdots & 0 \end{bmatrix} \tag{5.16}$$

Now, the Eq. (5.14) can be written as:

$$L = L_s + PKL \tag{5.17}$$

The reflectance matrix P can be derived from Eq. (5.17) as:

$$P = (L - L_s)L^{-1}K^{-1} \tag{5.18}$$

The parameters of matrix P are the reflectance of each facet, and can be obtained as:

$$\rho_i = \pi L_i(E_{si} + L_1K_{i1} + L_2K_{i2} + ... + L_mK_{im})^{-1} \tag{5.19}$$

where ρ_i is the reflectance of the ith facet, L_i is the radiance value of the ith facet, E_{si} is the irradiance value due to the light source, and K_{ij} is a coefficient between the ith and jth facets.

The irradiance value is calculated from Eq. (5.6) with known spectral radiance of the sun and sky. The radiance value is obtained from the input image. The K coefficient is determined only by the geometry of two facets on the object surface, and can be derived from the object shape. From Eq. (5.19), we acquire the reflectance of each facet on the object surface with the presence of inter-reflection.

5.5 Experiment

In this section, we first evaluate the outdoor illumination estimated from single perspective image. The simulated sky appearance is compared with the captured image for the accuracy verification. Then we show the estimated surface reflectance with the presence of inter-reflection based on the recovered illumination from estimated turbidity value. The experimental results show the accuracy achieved by the proposed method.

5.5.1 Evaluation of Outdoor Illumination Estimation

Since we use single perspective image for reflectance estimation,only partial sky is available, we first evaluated whether the partial sky could provide enough information for the outdoor illumination estimation. Specifically, we first estimate the turbidity from part of the input image and extract the sun direction, then the spectral radiance of the sun and the sky is calculated, after acquiring the spectral radiance we simulate the sky appearance by using the following equation:

$$I_c = \int_\Omega L(\lambda) Q_c(\lambda) d\lambda, \tag{5.20}$$

where I_c is the image intensity for *RGB* color channels, L is the spectral radiance and Q_c is the spectral sensitivity.

The result is shown in Fig. 5.7. Fig. 5.7 (a) is the captured image by Ladybug2, the red rectangle of (b) shows the partial sky used for turbidity estimation, (c) is the simulated sky appearance. The simulated result is very similar to the input image. The circumsolar region in Fig. 5.7 is saturated and useless. However, the sunlight plays an important role for estimating the surface reflectance. In order to solve this problem, we use the high dynamic range(HDR) image.

The captured and simulated HDR images are shown in Fig. 5.8. In order to make comparison, we captured the HDR image by using Ladybug2 camera. Multiple omni-directional images are captured with different exposures to make the HDR image. The simulated HDR image is also acquired by using Eq. (5.20). We evaluated the accuracy of estimated outdoor illumination: the intensity distribution of circumsolar region, the intensity and chromaticity distribution of sky portion. The sample points for the intensity evaluation of circumsolar region lie in the red line which goes through the sun position, as shown in Fig. 5.9. There are about 500 sample points. The numerical evaluation is shown in Fig. 5.11, only the intensity distribution of red channel is shown here. The intensity distributions of green and blue channels are the same, because the circumsolar region is white and the white color has same *RGB* values. For the intensity and chromaticity evaluations of sky portion, we sample 19 points which uniformly distributed on the sky, as shown in Fig. 5.10. The result is shown in Fig. 5.12. The evaluation results prove that the proposed method achieve high accuracy.

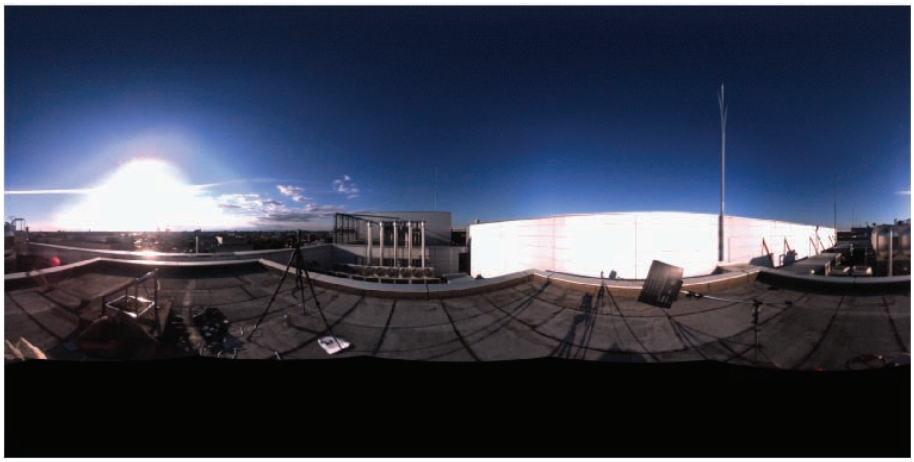

(a) Input image.

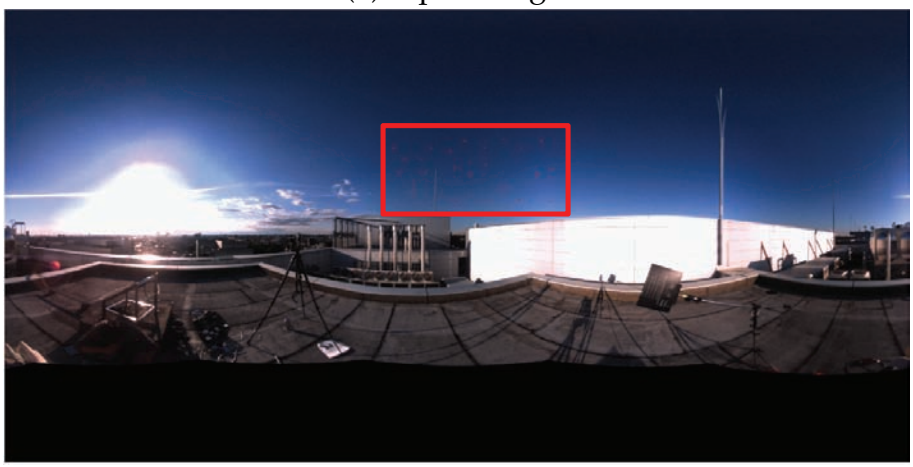

(b) The partial sky used for outdoor illumination estimation.

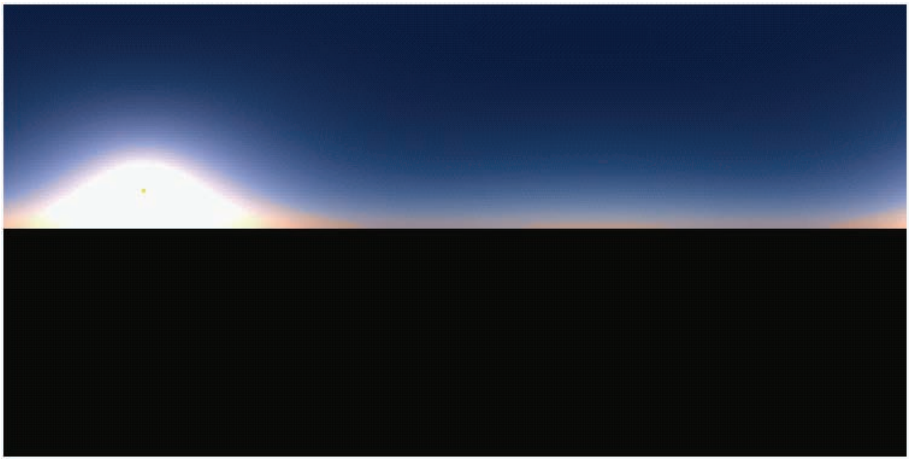

(c) Simulated sky appearance.

Figure 5.7: Input image and simulated sky appearance.

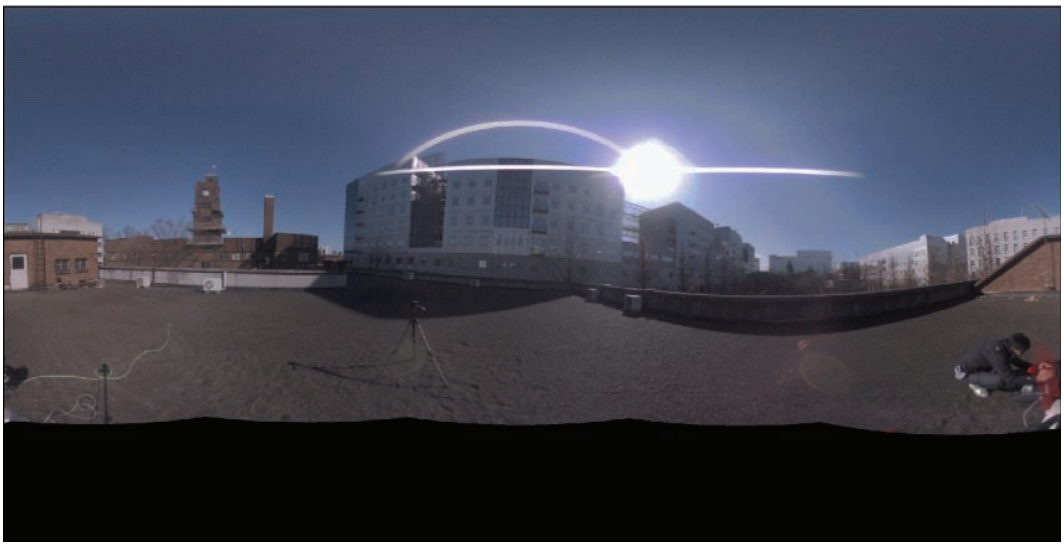

(a) Captured HDR image by Ladybug2.

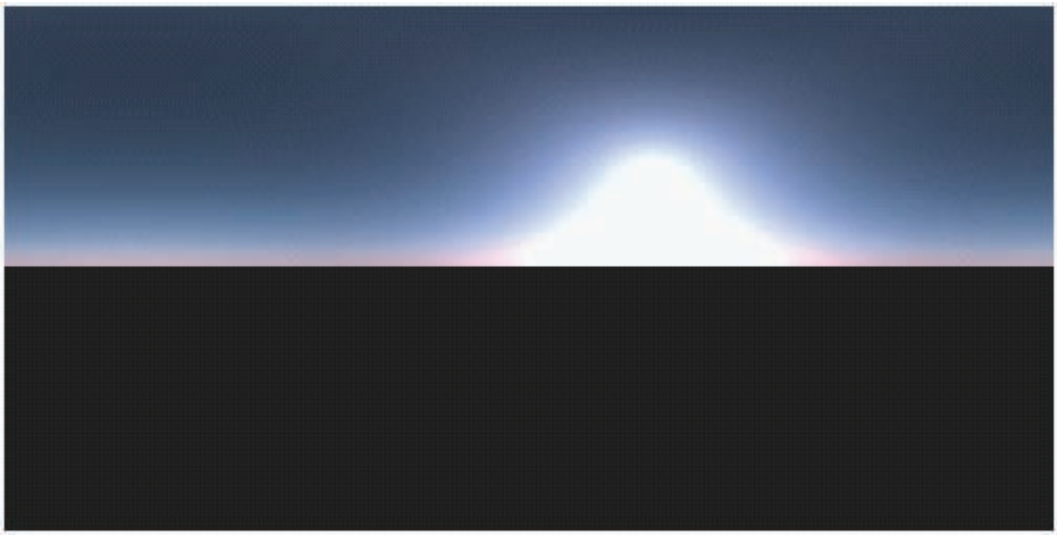

(b) Simulate HDR image of Ladybug2.

Figure 5.8: Captured and simulated HDR image of Ladybug2 camera. The simulated image is calculated from the turbidity. Specifically, we first estimate the turbidity from captured image then calculate the spectral radiance of the sun and sky from estimated turbidity value. The image *RGB* values are calculated from Eq. (5.20).

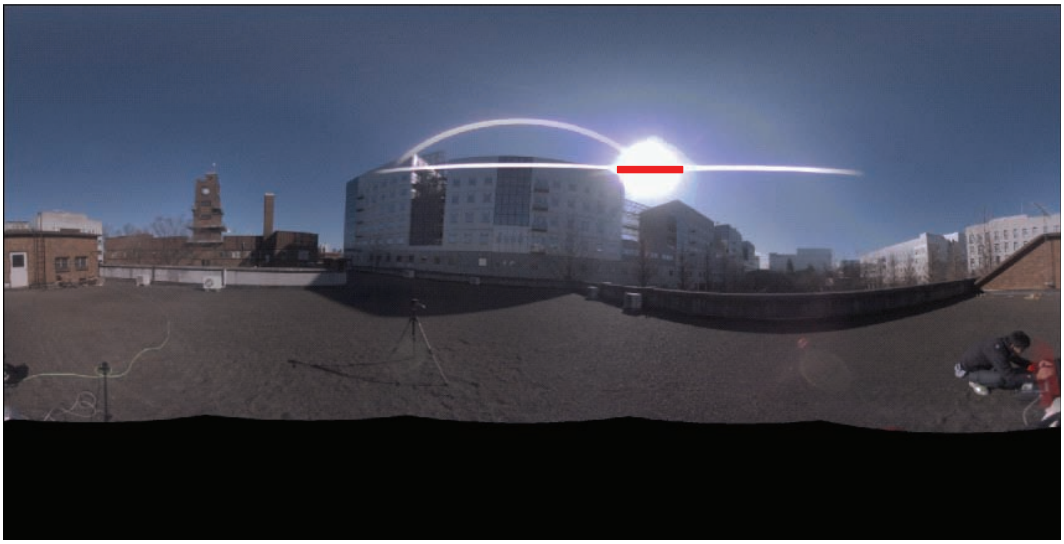

(a) Sample points around the sun area of captured image.

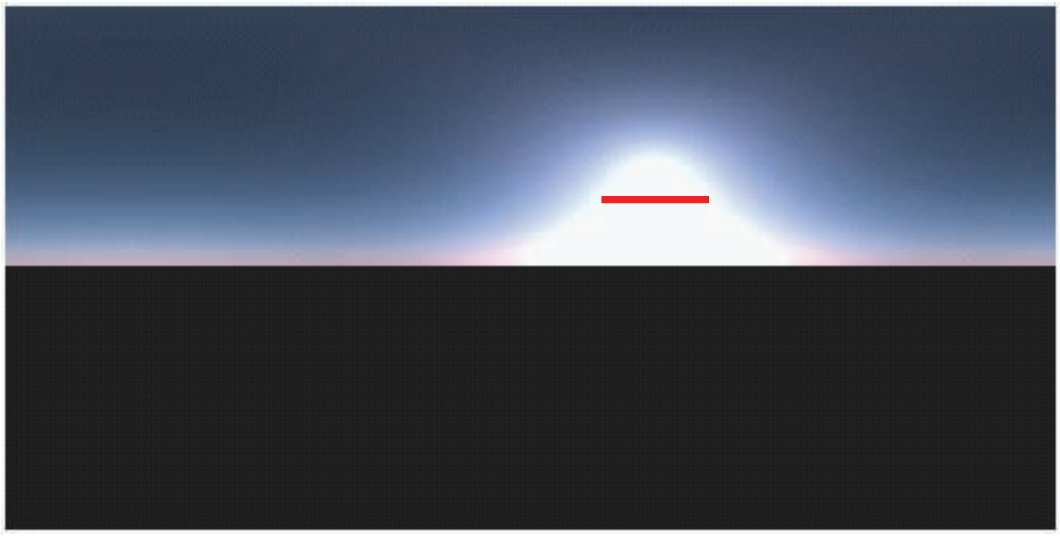

(b) Sample points around the sun area of simulated image.

Figure 5.9: Sample points around the sun area of captured and simulated HDR image. We sampled about 500 points and they lie in the red line. The red line goes through the extracted sun position.The sample points are used for the intensity distribution evaluation of circumsolar region.

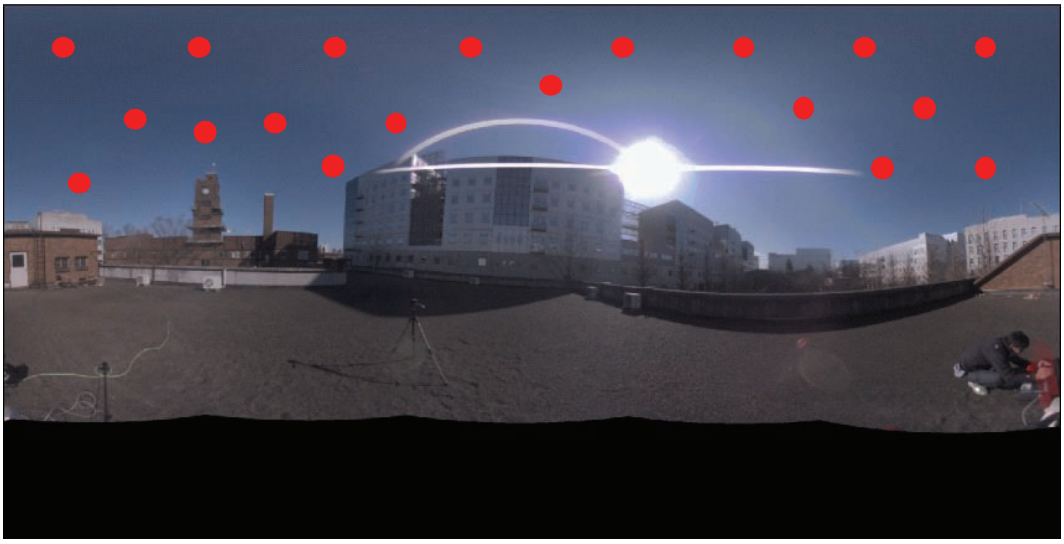

(a) Sample points in the sky area of captured image.

(b) Sample points in the sky area of simulated image.

Figure 5.10: Sample points in the sky area of captured and simulated HDR image. We sample 19 points, the sampled points are uniformly distribution on the upper hemisphere. These sample points are used for the intensity and chromaticity distribution evaluation of the sky portion.

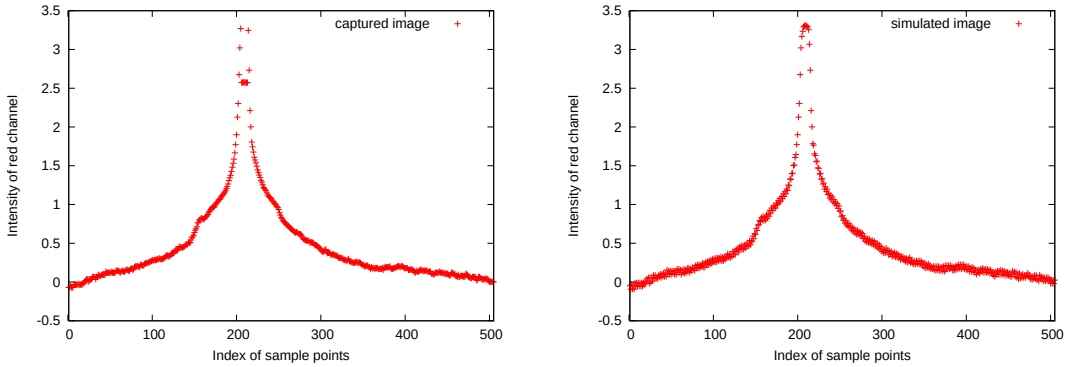

(a) Captured image. (b) Simulated image.

Figure 5.11: Intensity of circumsolar region of captured and simulated HDR image(red channel).

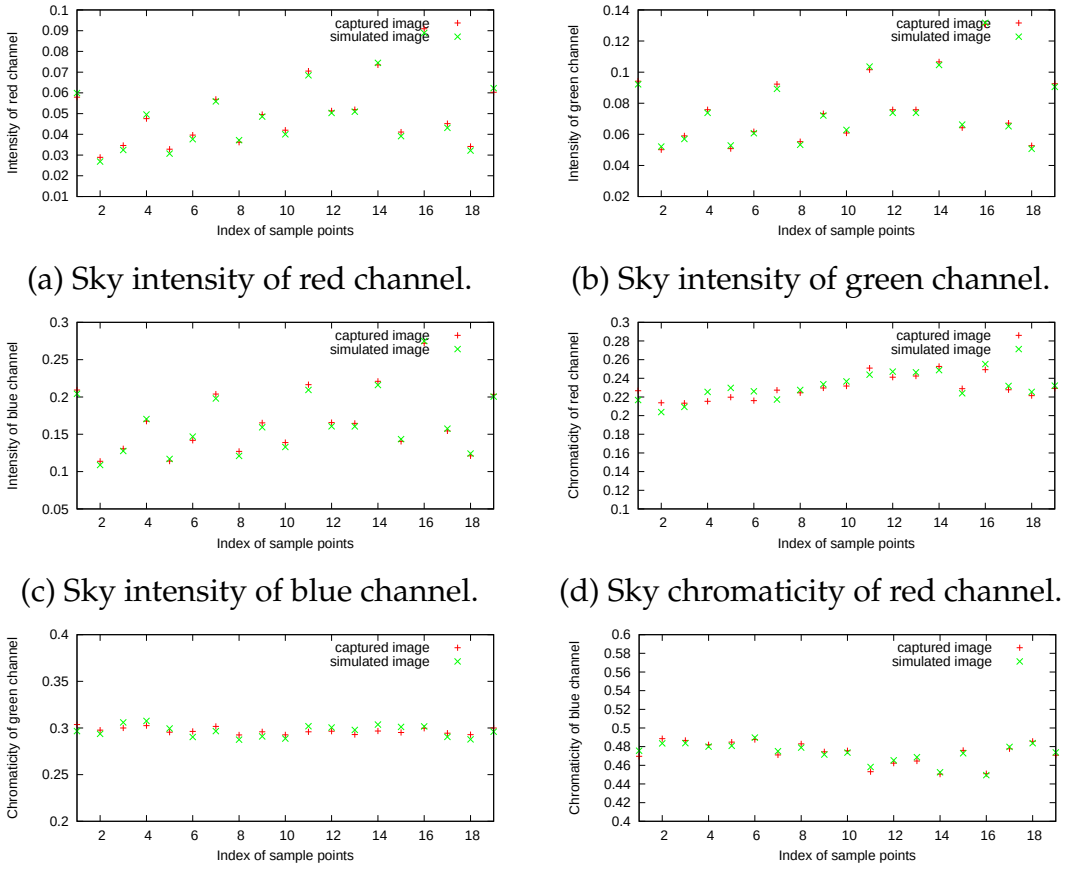

(a) Sky intensity of red channel. (b) Sky intensity of green channel.

(c) Sky intensity of blue channel. (d) Sky chromaticity of red channel.

(e) Sky chromaticity of green channel. (f) Sky chromaticity of blue channel.

Figure 5.12: Sky intensity and chromaticity of *RGB* color channels from captured and simulated HDR image.

(a) Captured image 1.

(b) Captured image 2.

(c) Captured image 3.

(d) Captured image 4.

(e) Captured image 5.

(f) Captured image 6.

Figure 5.13: Captured perspective images from different view directions by Canon 5D Mark II: (a), (b), (c), (d) and (e) are captured with clear skies, (f) is captured with cloudy sky. These captured images are used for recovering the camera parameters, we only need single one of these images to estimate the surface reflectance. In order to make the limitation of the proposed method clear, we also captured images with cloudy skies.

Figure 5.14: The range sensor Cyrax 2500 used to acquire the shape information.

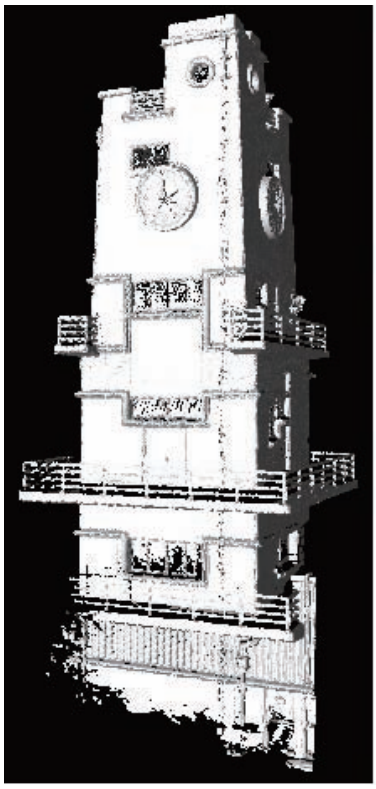

Figure 5.15: Acquired shape information of clock tower by Cyrax 2500.

5.5.2 Measurement of the Scene Radiance

We used the Canon 5D Mark II camera to capture the scene radiance. Multiple images are captured as shown in Fig. 5.13, although we only need one single image to estimate the surface reflectance. This is because we need to estimate the camera parameters, and the camera parameters are recovered from these images by using structure from motion(SfM). We captured about 80 images in total, Fig. 5.13 shows partial of the captured images. The images with clear skies and cloudy skies are captured. We use the cloudy sky image to show the limitation of the proposed method.

5.5.3 Measurement of the Object's Shape

The object shape information is acquired by the range sensor Cyrax 2500. This range sensor has a maximum $40^\circ \times 40^\circ$ field-of-view. With a single-point range accuracy of +/- 4mm, angular accuracies of +/- 60 micro-raians, and a beam spot size of only 6mm from 0-50m range, the Cyrax sensor delivers survey-grade accuracy while providing a versatile platform for data capture. Fig. 5.14 shows the range sensor Cyrax 2500. The acquired shape of clock tower is shown in Fig. 5.15. From the shape, we can get the surface normal and 3D coordinates of each facet on the object surface to calculate the inter-reflection effect.

5.5.4 Surface Reflectance Estimation

The surface radiance value, the surface irradiance value and object shape are required to estimate the surface reflectance. The surface radiance is acquired from the input perspective image. The surface irradiance value directly due to the light source can be calculated from Eq. (5.6). In this experiment, we used Radiance software to do the irradiance calculation. Specifically, first we set the reflectance of each facet to be 1.0 for all the *RGB* channels, then render the object by image based lighting method. The object shape is measured by the range sensor Cyrax 2500. After acquiring these three parameters, the surface reflectance is calculated from Eq. (5.19).

In the experiment, we first show how well the occlusion problem is solved and then estimate the surface reflectance from input perspective images. We also show the limitation of the proposed method by using the image with cloudy sky.

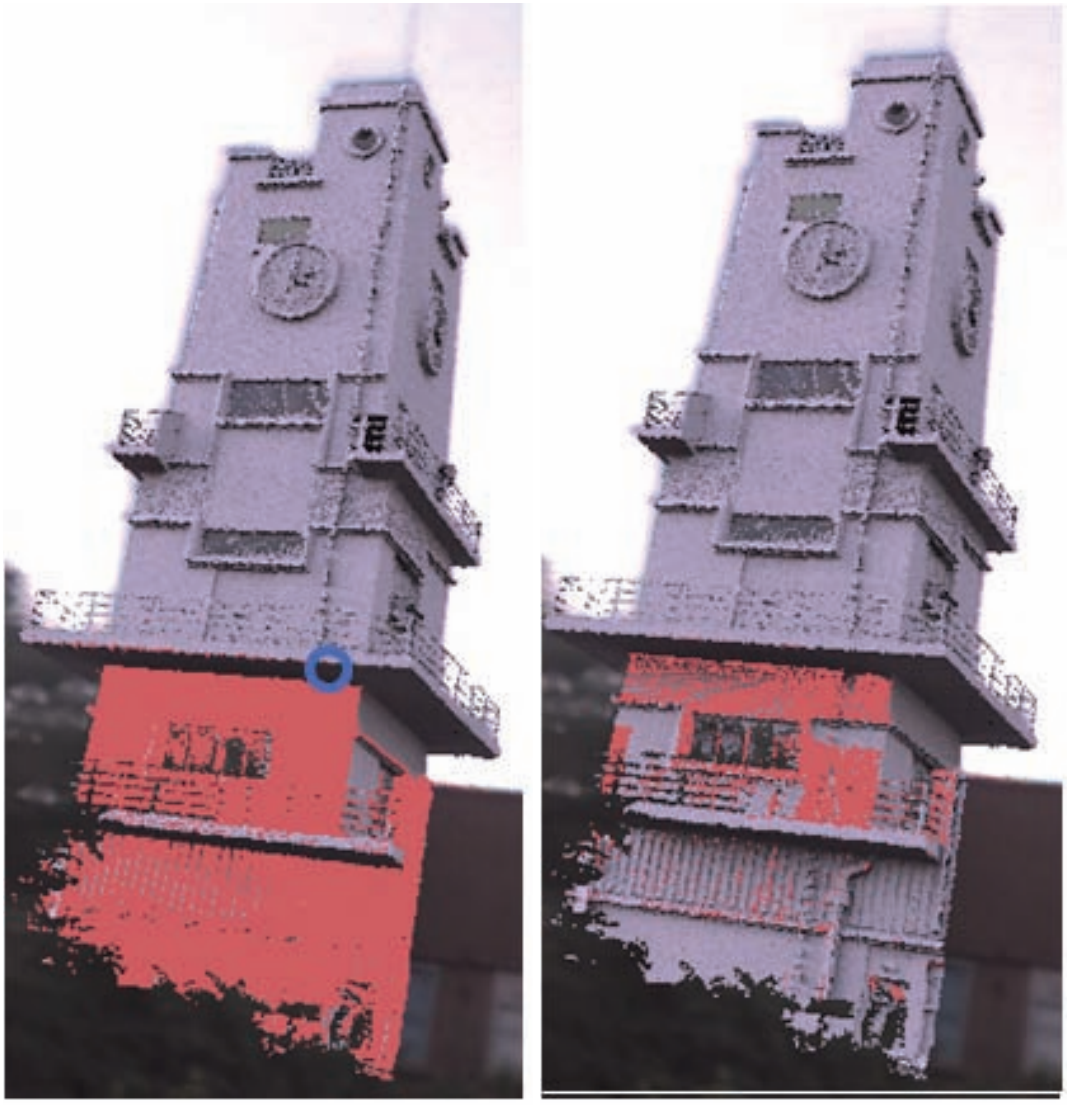

(a) K coefficient. (b) K coefficient.

Figure 5.16: (a) shows the K coefficient calculation with occlusion and (b) shows the K coefficient calculation without occlusion. For a point lies in the blue circle, the inter-reflection effect is calculated from all the red points. In Fig (a), some occluded points are included in the calculation because of the wrong K coefficient. Fig(b) proves we solve this problem.

As shown in Fig. 5.6, even though the visibility function without occlusion coefficient between these two facets is equal to 1, these two facets actually can not see each other because of the occlusion. Fig. 5.16 shows this kind of situation.

(a) From Ladybug2 camera. (b) From Canon 5D Mark II camera.

Figure 5.17: Estimated surface reflectance from the input perspective image and captured Ladybug2 image. The clock tower in these two images are different because of different camera view directions.

When estimating the reflectance of the small facet lies in the blue circle, the K_{ij} coefficient is calculated between this facet and all the other red facets shown in Fig.5.16 (a). Apparently, there are too many red facets that this facet actually can not see. But the K_{ij} coefficient was included in the sum as inter-reflection effect because of the occlusion between them. Without occlusion coefficient, the calculated inter-reflection effect would be too large, the estimated reflectance would be too small. We solve this occlusion problem by applying the occlusion coefficient to visibility function calculation. Specifically, we detect whether the vector between the ith and jth facets intersects with all the other facets or not. If the vector intersects with at least one of the other facets, then the occlusion coefficient is equal to 0, so is the K_{ij} coefficient. If not, the visibility function is equal to 1, and the K_{ij} coefficient can be calculated from Eq. (5.12).

Fig.5.16 (b) shows the situation when dealing with the occlusion problem by the method described before. The red facets have the same meaning as Fig.5.16 (a). For the

same facet, the number of red facets in Fig.5.16 (b) is only around one third of Fig.5.16 (a). Two thirds of red facets in Fig.5.16 (a) are occluded, and should not be seen by the facet lies in the blue circle. With the occlusion coefficient, the estimated reflectance becomes much more accurate.

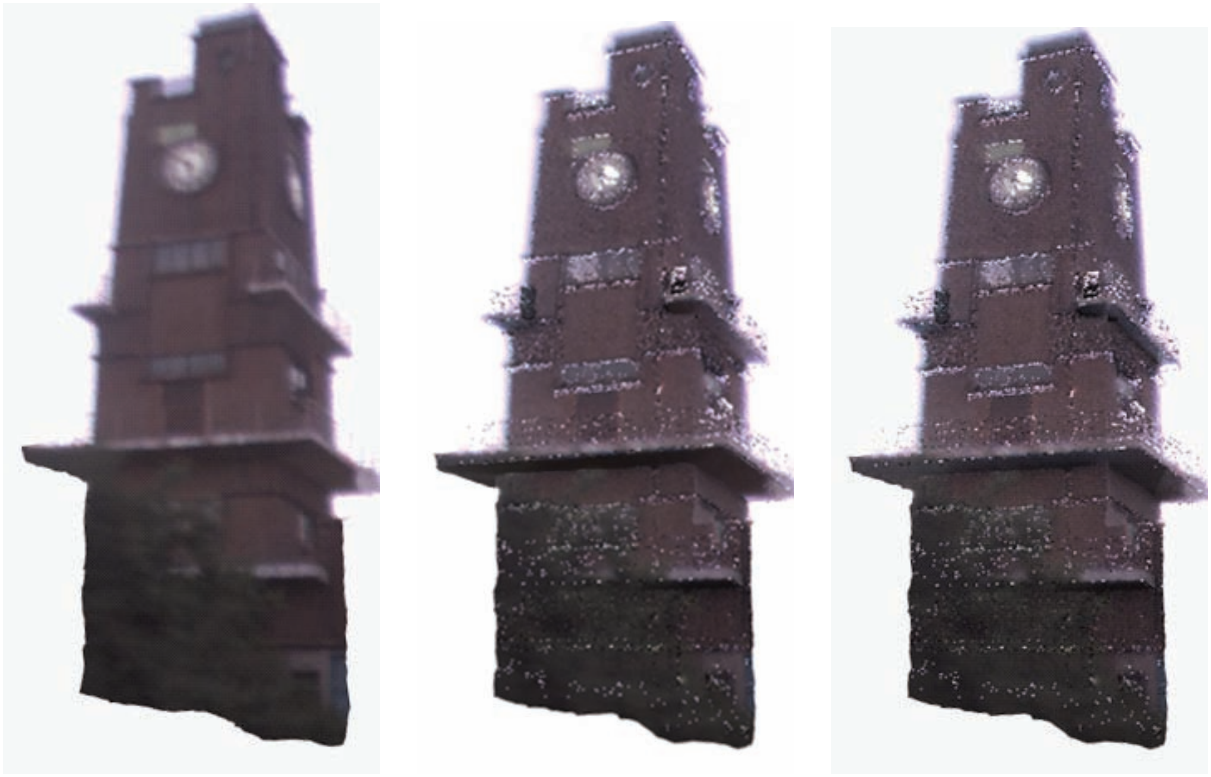

(a) Captured image. (b) Without inter-reflection. (c) With inter-reflection.

Figure 5.18: Simulated object appearance by estimated surface reflectance: (a) is the captured image, (b) shows the result without inter-reflection and (c) shows the result with inter-reflection.

We then evaluated the proposed method with perspective images with clear skies. The input image is shown in Fig. 5.13 (a). In order to verify the accuracy, we also captured the whole illumination condition by Ladybug2 camera. The captured image is shown in Fig. 5.8 (a). The result is shown in Fig. 5.17. The clock tower captured in Fig. 5.17 (a) and (b) are different, because the camera view directions are different. However, the estimated reflectance is similar to each other.

Another experiment result is shown in Fig. 5.18. Fig. 5.18 (a) is the captured image of clock tower, (b) is the result simulated by the previous method which does not take the inter-reflection effect into account, (c) is the result simulated by our proposed method.

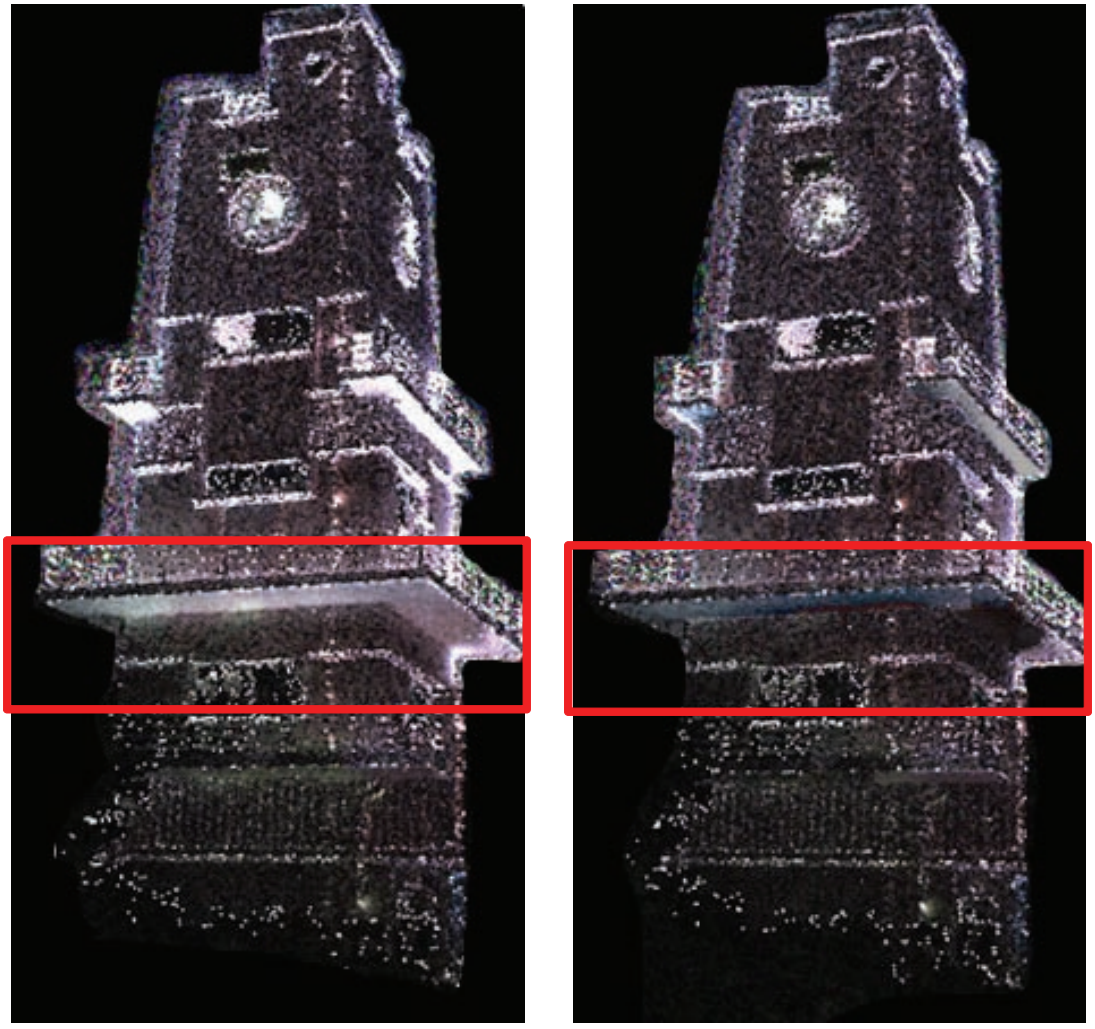

(a) Without inter-reflection. (b) With inter-reflection.

Figure 5.19: The difference between the captured image and simulated result. (a) shows the difference between the captured image and simulated appearance without inter-reflection while (b) shows the difference between the captured image and simulated appearance with inter-reflection. We use a red rectangle to highlight the part with strong inter-reflection.

From Eq. (5.6) and (5.7), if we divide the radiance value by the irradiance value of each facet, we can estimate the reflectance, however this does not handle the inter-reflection effect. Okura et al (2008) used this method to estimate the reflectance of an outdoor diffuse object. Fig. 5.18 (b) was rendered by this way, there is no inter-reflection effect calculated for each facet on the object surface. Fig. 5.18 (c) shows the synthesized image simulated with estimated reflectance, which are obtained by the proposed method.

Fig. 5.19 (a) and (b) show the difference between the captured image of clock tower (Fig. 5.18 (a)) and simulated result without inter-reflection effect (Fig. 5.18 (b)) and with inter-reflection effect (Fig. 5.18 (c)), respectively. From the comparison between Fig. 5.19 (a) and (b), for most concave parts of clock tower, if handling the inter-reflection effect, the re-rendered image looks much more realistic. The difference between the simulated result with inter-reflection effect and captured image of clock tower, especially for the concave parts, is less than three percent. But for simulated result without inter-reflection effect, the difference is bigger than sixty percent.

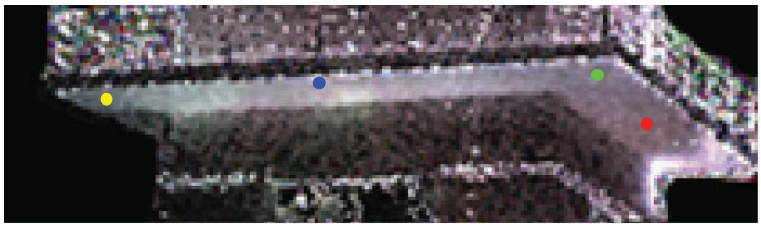

(a) Zoom in of the result without inter-reflection.

(b) Zoom in of the result with inter-reflection.

Figure 5.20: (a) shows the difference of zoomed in part between the captured image and simulated appearance without inter-reflection, (b) shows the difference of zoomed in part between the captured image and simulated appearance with inter-reflection.

In order to make it clear, we zoom in the red rectangle part in Fig. 5.19 (a) and (b). The amplified result is shown in Fig. 5.20 (a) and (b). In these Figures, the *RGB* values of the pixel (brightness) represents the error. If the error is larger, the pixel will be brighter. Obviously, the result estimated by the proposed method (as shown

(a) Cloudy image. (b) Simulated image.

Figure 5.21: Simulated object appearance from image with cloudy sky.

in Fig. 5.20 (b)) has much smaller errors. We took four pixels (the red, green, blue and yellow pixel as shown in Fig. 5.20 (a) and (b)) as examples, the difference for these four pixels between the captured image and simulated result without inter-reflection effect and with inter-reflection effect are shown in Table 5.1. Except the yellow pixel, the other three pixels of our proposed method have much smaller errors. The error for yellow pixel is larger compared to error of other pixels, because actually it is occluded by the tree which lies in front of the clock tower. The geometrical and optical information of this yellow pixel does not match. For the blue pixel which has strong inter-reflection effect, the error of Okura et al.'s method which does not take the inter-reflection into account is almost 10 times bigger than the error of the proposed method. This proves the efficiency of proposed method.

We applied the proposed method to captured image with cloudy sky to show the limitation. The result is shown in Fig. 5.21. Fig. 5.21 (a) shows the captured image and (b) shows the simulated object appearance. As shown in Fig. 5.13 (f), the input image is captured under cloudy sky. The color of simulated appearance from estimated surface reflectance is different from the input image. When the sky is covered by thick cloud, the estimated turbidity is deviated from the ground truth, because we use the

sky model for turbidity estimation and the sky model can not handle the cloud. The estimated outdoor illumination from turbidity is also deviated. The proposed method fails when the sky is covered by cloud.

Table 5.1: Difference of zoomed-in part of the method of Okura et al (2008) which dose not take the inter-reflection effect into account and the proposed method which takes the inter-reflection effect into account.

Pixels	Okura et al.'s method	The proposed method
Red pixel	0.041	0.011
Green pixel	0.067	0.009
Blue pixel	0.105	0.010
Yellow pixel	0.048	0.021

5.6 Summary

This chapter explains the proposed method to estimate the surface reflectance properties of outdoor diffuse object from single perspective image. The perspective image can not provide enough information, because only partial illumination environment is captured. In order to solve this problem, we use the atmospheric turbidity. Specifically, we first estimate the turbidity from the input perspective image, then recover the whole outdoor illumination from the estimated turbidity value. After acquiring the illumination, the surface reflectance is calculated. In the experiment, we first evaluate the accuracy of recovered outdoor illumination. The intensity distributions of circumsolar region and the intensity and chromaticity distributions of sky region from the captured and simulated HDR images are compared. The shape information is acquired by using the range sensor Cyrax 2500, the surface radiance is obtained from the input image and the surface irradiance values is calculated from the recovered illumination. The experiment results show the accuracy of the proposed method.

Chapter 6

Conclusions

6.1 Summary

This dissertation proposes a novel method for estimating the atmospheric turbidity and provides three applications of the estimated turbidity. The atmospheric turbidity is estimated by matching the brightness distribution of captured image to a sky model. After acquiring the turbidity, we can estimate the spectral sensitivity and white-balance parameters of digital cameras, we can calculate the aerial perspective effect for realistically rendering the virtual object and we can estimate the surface reflectance of outdoor diffuse object from a single perspective image.

6.1.1 Atmospheric Turbidity Estimation

The atmospheric turbidity describes the optical thickness of the haze atmosphere as opposed to the atmosphere of molecules alone. It is widely used in computer graphics and vision community. A novel method for estimating the turbidity is proposed and various evaluations on the turbidity are performed. The atmospheric turbidity is estimated by matching the brightness distributions between the captured image and a sky model. The proposed method for estimating the turbidity handles the situation of the same scene captured by different cameras or with different white-balance settings. The assumption (image intensity is proportional to the sky luminance) used for turbidity estimation and the robustness to noises are evaluated. The evaluations of whether the

captured images of the same scene by different cameras or with different white-balance settings and the accuracy of the sky model are also provided.

6.1.2 Spectral Sensitivity and White Balance Estimation from Sky Images

Spectral sensitivity is often required in physics-based computer vision. However, less attention has been paid for estimating the spectral sensitivity. Motivated by this lack of attention, we introduce a method for estimating the spectral sensitivity and white-balance parameters jointly from images. The basic idea is to use the sky images which infer the cues for sky spectral radiance. The sky chromaticity values are calculated from the estimated turbidity, then the spectral radiance of the sky is calculated from the chromaticity values by using the basis functions of the outdoor illumination. After acquiring the pairs of image *RGB* values and corresponding spectral radiance, the spectral sensitivity is calculated by using basis functions. The basis functions are extracted from the database which consists of collected spectral sensitivities, it makes the estimation accurate and robust.

6.1.3 Virtual Object Rendering With Aerial Perspective Effect

Virtual object rendering is widely used in many fields, such as the architecture, the academy, the medical industry, the entertainment and the heritage preservation. The aerial perspective plays an import role for making the rendered object appear realistic, especially when the object is distant from the camera. The aerial perspective effect is caused by the scattering of the particles suspended in the atmosphere. The spectral radiance of the sun and the sky is calculated from the estimated turbidity, and the aerial perspective is calculated as the summation of in-scattered and out-scattered spectral radiance of the sun and the sky light along the view direction. Experiment results show the accuracy achieved by the turbidity-based aerial perspective calculation.

6.1.4 Reflectance Estimation from a Single Perspective Image

The surface reflectance property is an essential factor for creating the realistic three-dimensional models. A novel method for estimating the surface reflectance of outdoor diffuse object from a single perspective image is proposed. The perspective image does

not provide enough information of illumination because only partial sky is captured. In order to solve this problem, we propose to recover the whole illumination condition from the atmospheric turbidity. After acquiring the turbidity, the spectral radiance of the sun and the sky is calculated. The inter-reflection and occlusion problems are also solved. In the experiment, we evaluate the recovered illumination environment and provide the estimated reflectance under various conditions.

6.2 Contribution

In this dissertation, we propose a novel method for estimating the atmospheric turbidity by matching the brightness distribution between the captured image and a sky model. We also provide three applications of estimated turbidity, the estimation of spectral sensitivity and white-balance settings, the virtual object rendering technique which takes the aerial perspective into account and the reflectance estimation of outdoor diffuse object from a single perspective image. The main contributions are summarized as follows:

Atmospheric turbidity estimation The main contribution of the turbidity estimation is the proposed method estimates the correct turbidity value from captured images of the same scene by different cameras or with different white-balance parameters. The *RGB* values of captured images by different cameras or with different white-balance settings are different according to different characteristics of spectral sensitivities, but the intensity (summation of *R*, *G* and *B* color channels) remains the same. Assuming the image intensity is proportional to the sky luminance, we acquire the correct value for the turbidity under the above situations.

Spectral sensitivity estimation The main contribution of the spectral sensitivity estimation is the utilization of sky images. By using sky images, we do not need the expensive equipment which measures the spectral radiance as the previous methods do (Hubel et al, 1994; Sharma and Trussell, 1993; Finlayson et al, 1998; Barnard and Funt, 2002; Ebner, 2007; Thomson and Westland, 2001), because the spectral radiance is calculated from the atmospheric turbidity. Other contributions are: (1) the basis functions which extracted from spectral sensitivity database, (2) a publicly available spectral sensitivity database and (3) spectral sensitivity-based color correction between different cameras.

Virtual object rendering The main contribution of the virtual object rendering is the turbidity-based aerial perspective calculation. The previous methods do not take the atmospheric turbidity into account (Klassen, 1987; Kaneda et al, 1991; Ward, 1994; Ebert et al, 1998). The aerial perspective is caused by the scattering of particles suspended in the atmosphere. The scattering coefficients of particles are determined by the turbidity. The atmospheric turbidity greatly improves the accuracy of calculated aerial perspective effect.

Reflectance estimation The main contribution of the reflectance estimation of outdoor diffuse object is we only need a single perspective image as input. The perspective image does not provide enough information for reflectance estimation, because only partial sky is captured. We propose to recover the whole illumination environment from the estimated turbidity. The proposed method works well as long as partial clear sky is captured. Compared to those methods which need expensive equipment or massive calibrations, the proposed method is much more convenient.

6.3 Future Work

The proposed method for estimating the atmospheric turbidity and the three applications: the spectral sensitivity estimation, the virtual object rendering and the reflectance estimation made significant progress. However, there are still some issues remained.

Cloudy sky model The atmospheric turbidity is estimated by matching the brightness distribution of captured sky image to a sky model (Preetham et al, 1999). Currently, the sky model can not handle the clouds. This does not affect the turbidity estimation, because we have proved only partial clear sky provide enough information. However, this do affect the reflectance estimation, because the recovered illumination environment is inaccurate when clouds present in the sky. Therefore, the future work is to introduce a sky model which can handle the clouds.

Efficient virtual object rendering The virtual object rendering technique which takes the aerial perspective effect into account has achieved high accuracy. However, the virtual object rendering is compute-intensive task and can not be applied for videos, because for each pixel of the rendered image, the aerial perspective effect based on the

light scattering (complicated integrals) is calculated. Therefore, the future work is to make the virtual object rendering be applied at real-time.

Appendix A

Sun Position from Perspective Image

For completeness, we include all the formulas derived in (Preetham et al, 1999). The sun direction denoted by the zenith (θ_s) and azimuth angle (ϕ_s) can be computed from the following equations:

$$\theta_s = \frac{\pi}{2} - \arcsin(\sin l \sin\delta - \cos l \cos\delta \cos\frac{\pi t}{12}), \tag{A.1}$$

$$\phi_s = \arctan(\frac{-\cos\delta \sin\frac{\pi t}{12}}{\cos l \sin\delta - \sin l \cos\delta \cos\frac{\pi t}{12}}), \tag{A.2}$$

where l is the site latitude in radians, δ is the solar declination in radians, and t is the solar time in decimal hours. δ and t are calculated as follows:

$$\delta = 0.4093 \sin(\frac{2\pi(J-81)}{368}), \tag{A.3}$$

$$t = t_s + 0.170 \sin(\frac{4\pi(J-80)}{373}) - 0.129 \sin(\frac{2\pi(J-8)}{355}) + \frac{12(SM-L)}{\pi}, \tag{A.4}$$

where J is Julian date, the day of the year as an integer in the range from 1 to 365. t_s is the standard time in decimal hours. J and t_s are derived from the time stamp in the image. SM is the standard meridian for the time zone in radians, and L is the site longitude in radians. The longitude l, latitude L and the standard meridian SM can be either given from the reference object's location, or from the GPS information in the image.

Appendix B

Calculating the Sky Luminance from Turbidity (Preetham et al, 1999)

The sky luminance is calculated by using Eq. (2.1), $\mathcal{F}(\theta, \gamma)$ is Perez *et al.*'s sky radiance distribution function (Perez et al, 1993), and it is described as:

$$\mathcal{F}(\theta, \gamma) = (1 + Ae^{B/\cos\theta})(1 + Ce^{D\gamma} + E\cos^2\gamma), \tag{B.1}$$

where A, B, C, D, and E are the five distribution coefficients, and θ and γ are shown in Fig. 2.2. The coefficients are linearly related to turbidity T according to Preetham et al (1999):

$$\begin{bmatrix} A_Y \\ B_Y \\ C_Y \\ D_Y \\ E_Y \end{bmatrix} = \begin{bmatrix} 0.1787 & -1.4630 \\ -0.3554 & 0.4275 \\ -0.0227 & 5.3251 \\ 0.1206 & -2.5771 \\ -0.0670 & 0.3703 \end{bmatrix} \begin{bmatrix} T \\ 1 \end{bmatrix}.$$

The ratio of sky luminance between one view direction and the reference direction in Eq. 2.2 is calculated as:

$$\begin{aligned} \frac{Y(T)}{Y_{ref}(T)} &= \frac{\mathcal{F}(\theta, \gamma)}{\mathcal{F}(\theta_{ref}, \gamma_{ref})} \\ &= \frac{(1 + Ae^{B/\cos\theta})(1 + Ce^{D\gamma} + E\cos^2\gamma)}{(1 + Ae^{B/\cos\theta_{ref}})(1 + Ce^{D\gamma_{ref}} + E\cos^2\gamma_{ref})}. \end{aligned} \tag{B.2}$$

Appendix C

Calculating the Sky Chromaticity from Turbidity (Preetham et al, 1999)

The correlation between the five distribution coefficients for the sky chromaticity values (x and y) and the turbidity T are as follows:

$$\begin{bmatrix} A_x \\ B_x \\ C_x \\ D_x \\ E_x \end{bmatrix} = \begin{bmatrix} -0.0193 & -0.2592 \\ -0.0665 & 0.0008 \\ -0.0004 & 0.2125 \\ -0.0641 & -0.8989 \\ -0.0033 & 0.0452 \end{bmatrix} \begin{bmatrix} T \\ 1 \end{bmatrix},$$

$$\begin{bmatrix} A_y \\ B_y \\ C_y \\ D_y \\ E_y \end{bmatrix} = \begin{bmatrix} -0.0167 & -0.2608 \\ -0.095 & 0.0092 \\ -0.0079 & 0.2102 \\ -0.0441 & -1.6537 \\ -0.0109 & 0.0529 \end{bmatrix} \begin{bmatrix} T \\ 1 \end{bmatrix}.$$

The zenith chromaticity x_z and y_z can also be determined by turbidity T as:

$$x_z = \begin{bmatrix} T^2 & T & 1 \end{bmatrix} \begin{bmatrix} 0.0017 & -0.0037 & 0.0021 & 0.000 \\ -0.0290 & 0.0638 & -0.0320 & 0.0039 \\ 0.1169 & -0.2120 & 0.0605 & 0.2589 \end{bmatrix} \begin{bmatrix} \theta_s^3 \\ \theta_s^2 \\ \theta_s \\ 1 \end{bmatrix}$$

$$y_z = \begin{bmatrix} T^2 & T & 1 \end{bmatrix} \begin{bmatrix} 0.0028 & -0.0061 & 0.0032 & 0.000 \\ -0.0421 & 0.0897 & -0.0415 & 0.0052 \\ 0.1535 & -0.2676 & 0.0667 & 0.2669 \end{bmatrix} \begin{bmatrix} \theta_s^3 \\ \theta_s^2 \\ \theta_s \\ 1 \end{bmatrix},$$

where θ_s is the sun direction. Thus, sky chromaticity x and y can be calculated only from the turbidity and the sun direction using Eq. (3.3). T usually ranges from 2.0 to 30.0.

The parameters M_1 and M_2 to determine spectra from the CIE chromaticity x and y can be calculated as follows:

$$M_1 = \frac{-1.3515 - 1.7703x + 5.9114y}{0.0241 + 0.2562x - 0.7341y}, \tag{C.1}$$

$$M_2 = \frac{0.0300 - 31.4424x + 30.0717y}{0.0241 + 0.2562x - 0.7341y}. \tag{C.2}$$

References

Azuma R (1997) A survey of augmented reality. Presence: Teleoperators and Virtual Environments 6(4):355–385

Azuma R, Baillot Y, Behringer R, Feiner S, Julier S, MacIntyre B (2001) Recent advances in augmented reality. IEEE Computer Graphics and Applications 21(6):34–47

Barnard K, Funt B (2002) Camera characterization for color research. Color Research and Application 27(3):153–164

Basri R, Jacobs D (2001) Photometric stereo with general unknown lighting. In: Proceedings of IEEE Computer Society Conference on Computer Vision and Pattern Recognition (CVPR), vol 2, pp 374–381

Bernardini F, Martin IM, Rushmeier H (2001) High-quality texture reconstruction from multiple scans. IEEE Transaction on Visualization and Computer Graphics 6:318–332

Brainard DH (1994) Bayesian method for reconstruction color images from trichromatic samples. In: IS & T, 47th Annual Conference, pp 375–380

Buil C (2005) Comparative test between canon 10d and nikon d70. http://astrosurf.com/buil/d70v10d/eval.htm

Chaiwiwatworakul P, Chirarattananon S (2004) An investigation of atmospheric turbidity of thai sky. Energy and Buildings 36:650–659

Chakrabarti A, Scharstein D, Zickler T (2009) An empircal camera model for internet color vision. In: Proceedings of British Machine Vision Conference

Chen T, Goesele M, Seidel HP (2006) Mesostructure from specularity. In: Proceedings of IEEE Computer Society Conference on Computer Vision and Pattern Recognition (CVPR), vol 2, pp 1825–1832

Cook R, Torrance K (1981) A reflectance model for computer graphics. In: ACM Transactions on Graphics (SIGGRAPH), pp 506–512

Dana KJ (2001) Brdf/btf measurement device. In: Proceedings of European Conference on Computer Vision (ICCV), p 460

Dana KJ, van Ginekken B, Nayar SK, Koenderink JJ (1999) Reflectance and texture of real-world surfaces. In: Proceedings of IEEE Computer Society Conference on Computer Vision and Pattern Recognition (CVPR), pp 151–157

Debevec P (1998) Rendering synthetic objects into real scenes: bridging traditional and image-based graphics with global illumination and high dynamic range photography. In: ACM Transactions on Graphics (SIGGRAPH), pp 189–198

Debevec P, Tchou C, Gardner A, Hawkins T, Poullis C, Stumpfel J, Jones A, Yun N, Einarsson P, Lundgren T, Fajardo M, Martinez P (2004) Estimating surface reflectance properties of a complex scene under captured natural illumination. USC ICT-TR-06

Debevec PE, Malik J (1997) Recovering high dynamic range radiance maps from photographs. In: ACM Transactions on Graphics (SIGGRAPH), pp 369–378

Debvec P, Hawkins T, Tchou C, Duiker HP, Sarokin W, Sagar M (2000) Acquiring the reflectance field of a human face. In: Proceedings of the 27th annual conference on computer graphics and interactive techniques, pp 145–156

D'Zmura M, Lennie P (1986) Mechanisms of color constancy. Journal of the Optical Society of America 3(10):1662–1672

Ebert D, Musgrave K, Peachey D, Perlin K, Worley (1998) Texturing and Modeling: A procedural approach. Academic Press

Ebner M (2007) Estimating the spectral sensitivity of a digital sensor using calibration targets. In: Proceedings of Conference on Genetic and Evolutionary Computation, pp 642–649

Finlayson G, Hordley S, Hubel P (1998) Recovering device sensitivities with quadratic programming. In: Proceedings of Color Science, System, and Application, pp 90–95

Finlayson GD, Drew MS, Funt BV (1994) Color constancy: generalized diagonal transforms suffice. Journal of the Optical Society of America 11(11):3011–3019

Forsyth DA (1990) A novel algorithm for color constancy. International Journal of Computer Vision 5(1):5–36

Freeman WT, Brainard DH (1995) Bayesian decision theory, the maximum local mass estimate, and color constancy. In: International Conference on Computer Vision, pp 210–217

Frieden BR (1983) Probability, statistical optics and data testing. Measurement Science and Technology

Goldstein EB (1980) Sensation and perception. Wadsworth

Haber T, Fuchs C, Bekaert P, Seidel HP, Geoesele M, Lensch HPA (2009) Relighting objects from image collections. In: Proceedings of Computer Vision and Pattern Recognition, pp 627–634

Hara K, Nishino K, Ikeuchi K (2005) Light source position and reflectance estimation from a single view without the distant illumination assumption. IEEE transactions on Pattern Analysis and Machine Intelligence 27(4):493–505

Hardeberg JY, Brettel H, Schmitt F (1998) Spectral characterization of electronic cameras. In: Electronic Imaging, pp 100–109

Hertzmann A, Seitz SM (2005) Example-based photometric stereo: Shape reconstruction with general, varying brdfs. IEEE Transactions on Pattern Analysis and Machine Intelligence 27:1254–1264

Higo T, Matsushita Y, Joshi N, Ikeuchi K (2009) A hand-held photometric stereo camera for 3-d modeling. In: Proceedings of International Conference on Computer Vision, pp 1234–1241

Hordley SD (2006) Scene illuminant estimation: Past, present, and future. Color Research and Application 31(4):303–314

Horn BKP (1989) Shape from shading. MIT Press Cambridge, MA, USA

Hubel PM, Sherman D, Farrell JE (1994) A comparison of method of sensor spectral sensitivity estimation. In: Proceedings of Color Science, System, and Application, pp 45–48

Ikeuchi K (1981) Determining surface orientations of specular surfaces by using the photometric stereo method. IEEE transactions on Pattern Analysis and Machine Intelligence 3(6):661–669

Ikeuchi K (2007) The virtual asukakyo project. http://www.cvl.iis.u-tokyo.ac.jp/research/virtual-asukakyo/

Ikeuchi K, Horn BKP (1981) Numerical shape from shading and occluding boundaries. Artificial Intelligence 17(1-3):141–184

Ikeuchi K, Miyazaki D (2008) Digitally archiving cultural objects. In: Springer science business media

Ikeuchi K, Oishi T, Takamatsu J, Sagawa R, Nakazawa A, Kurazume R, Nishino K, Kamakura M, Okamoto Y (2007) The great buddha project: Digitally archiving, restoring, and analyzing cultural heritage objects. International Journal of Computer Vision 75(1):189–208

Iqbal M (1983) An introduction to solar radiation. In: Academic Press

Judd DB, Macadam DL, Wyszecki G, Budde HW, Condit HR, Henderson ST, Simonds JL (1964) Spectral distribution of typical daylight as a function of correlated color temperature. Journal of the Optical Society of America 54(8):1031–1036

Kakuta T, Oishi T, Ikeuchi K (2004) Virtual kawaradera: Fast shadow texture for augmented reality. In: Proceedings of International Conference on Virtual Systems and Multimedia (VSMM), pp 141–150

Kaneda K, Okamoto T, Nakame E, Nishita T (1991) Photorealistic image synthesis for outdoor scenery under various atmosphere conditions. The Visual Computer 7(5 & 6):247–258

Kawakami R, Ikeuchi K (2009) Color estimation from a single surface color. In: Proceedings of Computer Vision and Pattern Recognition, pp 635–642

Kennedy J, Eberhart R (1995) Particle swarm optimization. In: Proceedings of IEEE International Conference on Neural Networks, pp 1942–1948

Klassen RV (1987) Modeling the effect of the atmosphere on light. In: ACM Transactions on Graphics (SIGGRAPH), pp 215–237

Kuthirummal S, Agarwala A, Goldman DB, Nayar SK (2008) Priors for large photo collections and what they reveal about cameras. In: Proceedings of European Conference on Computer Vision, pp 74–87

Lalonde JF, Efros AA, Narasimhan SG (2009) Estimating natural illumination from a single outdoor image. In: Proceedings of International Conference on Computer Vision, pp 183–190

Lalonde JF, Narasimhan SG, Efros AA (2010) What do the sun and the sky tell us about the camera? International Journal of Computer Vision 88(1):24–51

Lensch HP, Heidrich W, Seidel HP (2000) Automated texture registration and stitching for real world models. In: Pacific Graphics, pp 317–326

Li Y, Lin S, Lu H, Shum HY (2003) Multiple-cue illumination estimation in textured scenes. In: Proceedings of International Conference on Computer Vision, pp 1366–1373

Lin S, Lee SW (1999) Estimation of diffuse and specular appearance. In: Proceedings of International Conference on Computer Vision (ICCV), pp 855–860

Lin S, Gu JW, Yamazaki S, Shum HY (2004) Radiometric calibration using a single image. In: Proceedings of Computer Vision and Pattern Recognition, pp 938–945

Machida T, Yokoya N, Takemura H (2003) Surface reflectance modeling of real objects with interreflections. In: Proceedings of International Conference on Computer Vision, pp 170–177

Maloney LT, Wandell BA (1986) Color constancy: a method for recovering surface spectral reflectance. Journal of the Optical Society of America 3(1):29–33

Maloney LT, Wandell BA (1996) Color constancy: a method for recovering surface spectral reflectances. Journal of the Optical Society of American-A 3:29–33

Mann S, Picard R (1995) Being 'undigital' with digital cameras: Extending dynamic range by combining differently exposed pictures. In: Proceedings of IS & T Annual conference, pp 422–428

Matsushita Y, Nishino K, Ikeuchi K, Sakauchi M (2004) Illumination normalization with time-dependent intrinsic images for video surveillance. IEEE transactions on Pattern Analysis and Machine Intelligence 26(10):1336–1347

Nayar SK, Ikeuchi K, Kanade T (1991) Surface reflection: physical and geometrical perspectives. IEEE transactions on Pattern Analysis and Machine Intelligence 13(7):611–634

Neugebauer PJ, Klein K (1999) Texturing 3d models of real objects from multiple unregistrated photographic views. In: Computer Graphics Forum, pp 245–256

Nishino K, Zhang Z, Ikeuchi K (2001) Determining reflectance parameters and illumination distribution from a sparse set of images for view-dependent image synthesis. In: Proceedings of International Conference on Computer Vision, pp 599–606

Okura S, Kawakami R, Ikeuchi K (2008) Efficient estimation of diffuse surface reflectance in an outdoor scene using spherical images. In: Proceedings of Meeting on Image Recognition and Understanding (MIRU)

Parkkinen JPS, Hallikainen J, Jaaskelainen T (1989) Characteristic spectra of munsell colors. Journal of the Optical Society of America 6(2):318–322

Perez R, Seals R, Michalsky J (1993) An all weather model for sky luminance distribution. Solar Energy

Pratt WK, Mancill CE (1976) Spectral estimation techniques for the spectral calibration of a color image scanner. Applied Optics 15(1):73–75

Preetham AJ, Shirley P, Smits B (1999) A practical analytic model for daylight. In: ACM Transactions on Graphics (SIGGRAPH)

Pulli K, Cohen M, Duchamp T, Hopper H, Shapiro L, Stuetzle W (1997) View-based rendering visualizing real objects from scanned range and color data. In: Proceedings of Euro Graphics Workshop, pp 23–34

Ramamoorthi R, Hanrahan P (2001) A signal-processing framework for inverse rendering. In: ACM Transactions on Graphics (SIGGRAPH)

Ramanath R, Snyder W, Yoo Y, Drew M (2005) Color image processing pipeline. IEEE Signal Processing Magazine 22(1):34–43

Reinhard E, Adhikhmin M, Gooch B, Shirley P (2001) Color transfer between images. Computer Graphics and Application 21(5):34–41

Sato I, Sato Y, Ikeuchi K (1999a) Acquiring a radiance distribution to superimpose virtual objects onto a real scene. In: Proceedings of IAPR Workshop on Machine Vision Applications, pp 19–22

Sato I, Sato Y, Ikeuchi K (1999b) Illumination distribution from brightness in shadows: adaptive estimation of illumination distribution with unknown reflectance properties in shadow regions. In: Proceedings of International Conference on Computer Vision (ICCV), pp 875–882

Sato I, Okabe T, Sato Y, Ikeuchi K (2003a) Appearance sampling for obtaining a set of basis images for variable illumination. In: Proceedings of International Conference on Computer Vision (ICCV), pp 800–807

Sato I, Sato Y, Ikeuchi K (2003b) Illumination from shadows. IEEE transactions on Pattern Analysis and Machine Intelligence 25(3):290–300

Sato Y, Wheeler MD, Ikeuchi K (1997) Object shape and reflectance modeling from observation. In: ACM Transactions on Graphics (SIGGRAPH)

Shafer SA (1985) Using color to separate reflection components. Color Research and Application 10(4):210–218

Sharma G, Trussell HJ (1993) Characterization of scanner sensitivity. In: Proceedings of Transforms & Transportability of Color, pp 103–107

Slater D, Healey G (1998) What is the spectral dimensionality of the illumination functions in outdoor scenes? In: Proceedings of Computer Vision and Pattern Recognition, pp 105–110

Takai T, Niimura K, Maki A, Matsuyama T (2004) Difference sphere: An approach to near light source estimation. In: Proceedings of IEEE Computer Society Conference on Computer Vision and Pattern Recognition (CVPR), pp 98–105

Takamatsu J, Matsushita Y, Ikeuchi K (2008) Estimating camera response functions using probabilistic intensity similarity. In: Proceedings of Computer Vision and Pattern Recognition

Tan RT, Nishino K, Ikeuchi K (2004) Color constancy through inverse intensity-chromaticity space. Journal of the Optical Society of America 21(3):321–334

Thomson M, Westland S (2001) Colour-imager characterization by parametric fitting of sensor response. Color Research and Application 26(6):442–449

Tominaga S (1996) Surface reflectance estimation by the dichromatic model. Color Research and Application 21(2):104–114

Vora PL, Farrell JE, Tietz JD, Brainard DH (1997) Digital color cameras - 2 - spectral response. Tech. Rep. HPL-97-54, HP corporation

Vrhel MJ, Trussell HJ (1994) Filter considerations in color correction. IEEE Transactions on Image Processing 3(2):147–161

Wang L, Kang SB, Szeliski R, Shum HY (2001) Optimal texture map reconstruction from multiple views. In: Proceedings of IEEE Computer Society Conference on Computer Vision and Pattern Recognition (CVPR), pp 347–354

Ward GJ (1992) Measuring and modeling anisotropic reflection. In: ACM Transactions on Graphics (SIGGRAPH), pp 265–272

Ward GJ (1994) The radiance lighting simulation and rendering system. In: ACM Transactions on Graphics (SIGGRAPH), pp 459–472

van de Weijer J, Gevers T, Gijsenij A (2007) Edge-based color constancy. IEEE Transactions on Image Processing 16(9):2207–2214

Weiss Y (2001) Deriving intrinsic images from image sequences. In: Proceedings of International Conference on Computer Vision (ICCV), pp 68–75

Winnemoller H, Mohan A, Tumblin J, Gooch B (2005) Light waving: Estimating light position from photographs alone. In: Computer Graphics Forum 24-3, pp 433–438

Woodham RJ (1980) Photometric method for determining surface orientation from multiple images. Optical Engineering 19(1):139–144

Wyszecki G, Stiles WS (1982) Color Science. Wiley Interscience publication

Yu Y, Malik J (1998) Recovering photometric properties of architectural scenes from photographs. In: ACM Transactions on Graphics (SIGGRAPH)

Zhang R, Tsai P, Cryer JE, Shah M (1999) Numerical shape from shading and occluding boundaries. IEEE transactions on Pattern Analysis and Machine Intelligence 21(8):690–706

Zhao H (2011) Spectral sensitivity database. http://www.cvl.iis.u-tokyo.ac.jp/~zhao/database.html

List of Publications

Journal Papers

1. Hongxun Zhao, Rei Kawakami, Robby T. Tan, Katsushi Ikeuchi, "Spectral Sensitivity and White Balance Estimation from Sky Images," *International Journal of Computer Vision,* (IJCV), under review

2. Hongxun Zhao, Rei Kawakami, Katsushi Ikeuchi, "Surface Reflectance Estimation of Outdoor Diffuse Object from a Single Perspective Image," *Journal of Optics Society of America,* be submitted soon

International Conference

1. Hongxun Zhao, Rei Kawakami, Robby T. Tan, Katsushi Ikeuchi, "Virtual Object Rendering with Turbidity-based Aerial Perspective Calculation," *IEEE International Symposium on Mixed and Augmented Reality,* be submitted soon

Domestic Conferences

1. Hongxun Zhao, Sonoko Okura, Rei Kawakami, Katsushi Ikeuchi, "Reflectance Estimation of Outdoor Diffuse Object with the Presence of Inter-reflection," *Computer Vision and Image Media,* (CVIM), 2008

2. Hongxun Zhao, Rei Kawakami, Robby T. Tan, Katsushi Ikeuchi, "Estimating Basis Functions for Spectral Sensitivity of Digital Cameras," *Meeting on Image Recognition and Understanding,* (MIRU), 2009

International Workshops

1. Hongxun Zhao, Rei Kawakami, Katsushi Ikeuchi, "Reflectance Estimation with the Presence of Inter-reflection and Camera Sensitivity Recovery," *KAIST-UT Workshop,* 2009